NONADIABATIC QUANTUM WAVE PACKET DYNAMICS OF REACTIVE CHEMICAL SYSTEMS

A Thesis Submitted for the Degree of

DOCTOR OF PHILOSOPHY

B. JAYACHANDER RAO

SCHOOL OF CHEMISTRY
UNIVERSITY OF HYDERABAD
• HYDERABAD 500046
INDIA

September 2008

Dedicated

To

My Family

STATEMENT

I hereby declare that the matter embodied in this thesis is the result of investigations carried out by me in the School of Chemistry, University of Hyderabad, Hyderabad, under the supervision of **Prof. Susanta Mahapatra**.

In keeping with the general practice of reporting scientific observations, due acknowledgement has been made whenever the work described is based on the findings of other investigations.

(**B. Jayachander Rao**)

School of Chemistry
University of Hyderabad
Central University P. O.
Hyderabad 500046
India

CERTIFICATE

Certified that the work embodied in this thesis entitled "**NONADIABATIC QUANTUM WAVE PACKET DYNAMICS OF REACTIVE CHEMICAL SYSTEMS**" has been carried out by Mr. **B. Jayachander Rao** under my supervision and the same has not been submitted elsewhere for a Degree.

(**Prof. Susanta Mahapatra**)
Thesis Supervisor

Dean
School of Chemistry

List of Abbreviations

BO	-	Born-Oppenheimer
PES	-	Potential energy surface
CI	-	Conical intersections
JT	-	Jahn-Teller
PJT	-	Pseudo Jahn-Teller
RT	-	Renner-Teller
TISE	-	Time-independent Schrödinger equation
WP	-	Wave packet
FC	-	Franck-Condon
TDSE	-	Time-dependent Schrödinger equation
QM	-	Quantum mechanical
GP	-	Geometric phase
DR	-	Dissociative recombination
LSTH	-	Lie-Siegbahn-Truhlar-Horowitz
DMBE	-	Double many-body expansion
BKMP	-	Boothroyd-Keogh-Martin-Peterson
CASSCF	-	Complete active space self consistent field
MRCI	-	Multireference configuration interaction
QCT	-	Quasiclassical trajectory
RKHS	-	Reproducing kernel Hilbert space
CS	-	Coupled states or centrifugal sudden
CC	-	Coriolis coupling
BF	-	Body-fixed
GWP	-	Gaussian wave packet
SOD	-	Second order differencing
SO	-	Split-Operator

CP	-	Chebyshev polynomial
SIL	-	Short iterative Lanczos
FFT	-	Fast Fourier transform
DVR	-	Discrete variable representation
FBR	-	Finite basis representation
GLQ	-	Gauss Legendre quadrature
NNSD	-	Nearest neighbor space distribution
CSF	-	Configuration state function

Acknowledgements

I wish to express my deep sense of gratitude and indebtedness with profound respect to my supervisor **Prof. Susanta Mahapatra** for his constant encouragement throughout my research work. I have learnt a lot from his meticulous planning and implementation, dedication and hard work. I have benefited immensely, both academically and personally through my association with him.

I extend my sincere thanks to the former and present Deans, School of Chemistry, for providing all the facilities to carry out my research work. I also thank all the faculty members and the non-teaching staff of the school for their cooperation and assistance on various occasions. I express my gratitude to Prof. K. D. Sen for his encouragement and guidance on various occasions. Special thanks to Prof. E. D. Jemmis for taking initiative to provide a high-class computational facility in this campus under the University for Potential Excellence (UPE) and High Performance Computational Facility (HPCF) programs. Special thanks to Prof. Durga Prasad for interest in this work and valuable suggestions.

Financial assistance from the Council of Scientific and Industrial Research (CSIR) is acknowledged.

I thank my senior colleagues Dr. Padmanaban, Dr. Subhas and Dr. Venkatesh for many stimulating discussions and help on various occasions. I especially thank Dr. Padmanaban and Dr. Subhas for their help during the initial days of my Ph.D. research work. I also thank my juniors Siva, Tanmoy, Susanta, Rajagopal Rao, Susruta, Rajagopal Reddy and Tanmoy Roy for maintaining a cheerful atmosphere in lab.

I would like to thank Mrs. Gitashri Mahapatra, Anusha Mahapatra and Anish Mahapatra for providing a homely atmosphere and for their delightful company on various occasions.

Last, but not the least, I take immense pleasure in thanking my parents for their constant encouragement and support throughout my life. I would like to thank my wife for her constant support and encouragement. I also thank all my family members.

Contents

1 Introduction **1**

1.1 Hydrogen exchange reaction and its isotopic variants 3

1.1.1 Potential energy surface of H + H_2 reaction 4

1.1.2 Nonadiabatic effects in H + H_2 reaction 7

1.2 Bimolecular atom-diatom insertion reactions 10

1.2.1 The N (^2D) + H_2 insertion reaction 11

1.2.2 Potential energy surface for the N (^2D) + H_2 reaction . . . 13

1.2.3 Nonadiabatic effects in N (^2D) + H_2 reaction 14

1.3 Current state of research and the aim of the present work 15

1.4 Overview of the Thesis 17

2 Quantum dynamics on coupled electronic states **20**

2.1 Introduction 20

2.2 Hamiltonian 21

2.3 Preparation of the initial WP 24

2.4 Time evolution of the initial WP 26

2.5 Final analysis (Quantum flux operator approach) 30

2.5.1 Calculation of reaction probability 31

2.5.2 Calculation of reaction cross sections and thermal rate constants . . . 33

3 Nonadiabatic quantum wave packet dynamics of hydrogen exchange reaction and its isotopic variants 35

3.1 Introduction . . . 35

3.2 Results and Discussion . . . 38

3.2.1 Computational details . . . 38

3.2.2 Reaction Probability and Time Dependence of Electronic Population . . . 39

3.2.3 Initial State-Selected Integral Reaction Cross Sections . . . 50

3.2.4 Thermal Rate Constants . . . 58

3.3 Effect of reagent rotation and vibration on the H + H_2 reaction . . . 63

3.3.1 Reaction probability . . . 63

3.3.2 Initial state-selected integral reaction cross sections . . . 67

3.4 Coriolis coupling effects . . . 71

3.4.1 Computational Details . . . 73

3.4.2 Reaction Probabilities . . . 74

3.5 Summary . . . 78

4 Quantum wave packet dynamics of N(^2D) + H_2 reaction 81

4.1 Introduction . . . 81

4.2 Theoretical and computational details . . . 82

4.2.1 Integral reaction cross sections and thermal rate constants 82

4.2.2 Vibrational energy level spectrum of the NH_2 radical . . . 82

4.3 Results and Discussion . . . 85

4.3.1 Reaction Probability, Integral Reaction Cross Section and Thermal Rate Constant 85
4.3.2 On the insertion type of mechanism of the N + H_2 reaction 91
4.3.3 Vibrational energy level spectrum of the $1^2A''$ electronic state of NH_2 95
4.4 Summary 103

5 On the ($E\otimes e$)-Jahn-Teller CIs in the 3p (E') and 3d (E'') Rydberg electronic states of triatomic hydrogen 105

5.1 Introduction 105
5.2 Diabatic electronic states and conical intersections 107
5.3 Theoretical framework to treat the nuclear dynamics 117
5.4 Results and discussion 118
5.4.1 Vibronic energy levels of the 3p (E') Rydberg electronic manifold 119
5.4.2 Vibronic energy levels of the 3d (E'') Rydberg electronic manifold 126
5.4.3 Time-dependent wave packet dynamics 130
5.5 Summary 136

6 Future Directions 140

Chapter 1

Introduction

The celebrated Born-Oppenheimer (BO) [1, 2] adiabatic approximation has been the cornerstone in the development of quantum mechanical treatment of chemical reaction dynamics. The large mass of the nucleus as compared to that of an electron permits an approximate separation of the motion of these two microscopic particles. The concept of adiabatic potential energy surfaces (PESs), defined by the BO approximation is fundamental to the understanding of chemical reaction dynamics and molecular spectroscopy. Many chemical reactions can be rationalized in terms of the motion of atomic nuclei on a single BO PES. This well known approximation breaks down when two or more electronic PESs become degenerate at some (finite or infinite) number of molecular configurations. For such an intersection to appear, these molecules should necessarily contain at least two nuclear coordinates [3]. In a simple two-electronic picture, only two independent relations between three electronic Hamiltonian matrix elements are sufficient for the existence of doubly degenerate electronic energy eigenvalues [4]. As a result, these relations can easily be satisfied explaining thereby the frequent occurrence of conical intersections (CIs) of PESs [4–6]. For polyatomic molecules with their dense electronic states and many nuclear degrees of freedom, CIs of BO PESs have become a generic feature [6,7]. CIs occurring due to the symmetry enforced instabilities in Jahn-Teller (JT) active molecules in their nonlinear configurations are well known in the literature [8–11] and are known as JT CIs. Another subclass which deals with the interaction between the degenerate and nondegenerate states and are referred to as pseudo - JT (PJT) systems in the literature [12–15]. Linear molecules are exceptions of the JT and PJT interactions but instabilities (for linear geometries) in their degenerate electronic states leads to Renner-Teller (RT) or glancing type of interactions [16,17].

CIs of PES are ubiquitous in polyatomic molecules, and their existence leads to a complete breakdown of BO adiabatic approximation and therefore, nonadiabatic electronic transitions take place during the nuclear motion. As a result, it is necessary to monitor the nuclear motions simultaneously on more than one electronic PES in a nuclear dynamical study [12,18]. Apart from this, a second complexity arises from the diverging nature of the (derivative) non-adiabatic coupling elements in the adiabatic electronic basis making it unsuitable for dynamical studies. In order to deal with this situation one resorts to a diabatic electronic representation [19–21], where the diverging kinetic coupling elements are transformed into the smooth potential coupling elements and thereby the discontinuity of the adiabatic representation is avoided. Various approximate schemes have been proposed for this adiabatic-to-diabatic transformation [22–24] through a suitable unitary transformation of the adiabatic electronic states defined in terms of the adiabatic-to-diabatic mixing angle [25].

One generally follows either a time-independent or a time-dependent quantum mechanical approach for the simulation of the nuclear dynamics. In a time-independent method, the time-independent Schrödinger equation (TISE) is solved by representing the nuclear Hamiltonian in a suitable basis. In time-dependent approach, an initial wave packet (WP) corresponding to the ground vibrational level is prepared which is subjected to a Franck-Condon (FC) transition to the final electronic state(s), where it is propagated with aid of time-dependent Schrödinger equation (TDSE) in a spectroscopic study. In a reactive scattering study, the initial WP is located in the reagent asymptote of the PES and propagated thereafter by solving the TDSE. The dynamical observables are finally calculated from the time evolved WP.

1.1 Hydrogen exchange reaction and its isotopic variants

The hydrogen exchange reaction, $H + H_2 \rightarrow H_2 + H$ is the simplest chemical reaction consisting of three nuclei and three electrons and has been a prototype model in the development of chemical reaction dynamics [26, 27]. Dynamical studies on this reaction started in the late 1920 [28]. Accurate quantum mechanical (QM) calculations appeared about a half a century later, in 1970s [29]. Full and converged QM calculations were performed in 1980s [30]. With advances in theoretical and experimental methods, good agreement between the theory and experiment has been achieved for integral and differential reaction cross sections and thermal rate constants in recent times [31–42,44,45]. The increase in the precision of the experimental data [46, 47] drove the theoretical research to consider the complex electronic nonadiabatic interactions in the nuclear dynamics of this fundamental reaction, since it occurs on an orbitally degenerate electronic state. Attempts were made to include such nonadiabatic quantum mechanical effects either in terms of geometric phase (GP) change of adiabatic electronic wavefunction or by considering the nonadiabatic coupling explicitly in the formalism [25, 48].

The triatomic hydrogen H_3 has been a benchmark candidate to understand the most fundamental chemical processes occurring on Earth as well as in the interstellar media [49]. In spite of its structural simplicity, the fragmentation dynamics of Rydberg excited H_3 appears to follow an outstandingly complex mechanism [50–54]. The process of dissociative recombination (DR) of triatomic hydrogen ion H_3^+ has attracted extensive attention from both experiment and theory in recent times [53, 55]. The H_3^+ ion acts as proton donor in chemical reactions that occur in interstellar clouds [56]. It is also the simplest triatomic ion, and serves as a benchmark system to understand the polyatomic DR processes. Various nonadiabatic transitions are expected to contribute to the observed dissociative recombination when a H_3^+ ion captures an electron and the resulting Rydberg H_3 subsequently dissociates, via,

$$\mathrm{H}_3^+ + e^- \rightarrow \mathrm{H}_3^* \rightarrow \mathrm{H}_2 + \mathrm{H} \ \mathit{or} \ \mathrm{H} + \mathrm{H} + \mathrm{H} \tag{1.1}$$

This dissociative recombination is an important process in the chemistry of diffuse interstellar cold plasma clouds. The JT and PJT - type of interactions among various Rydberg electronic manifolds of H_3 have been predicted to play a crucial a role in it [52–54]. In this context, investigations of the structure and dynamics of the 3p (E') and 3d (E'') Rydberg electronic states of H_3 radical was felt to be important to understand the DR process and pursued here.

1.1.1 Potential energy surface of H + H_2 reaction

There are several global *ab initio* electronic PESs available in the literature for this system. They are well-known by the abbreviations viz., LSTH [57, 58], DMBE [59], BKMP [60] and BKMP2 PESs [61]. Varandas *et al.* [59] have reported an analytical representation of the two lowest electronic PESs of H + H_2 based on the DMBE (double many body expansion) method. These authors have used 267 *ab initio* points of Liu and Siegbahn [62,63], 31 points from Blomberg and Liu [64] and 18 new *ab initio* points. Their *ab initio* calculations employed a primitive $(9s3p1d)$ basis set contracted to $[4s3p1d]$. They first performed a complete-active-space-self-consistent-field (CASSCF) calculation [65] with the three active orbitals to obtain eight configurations and followed by a multireference configuration interaction calculation with all single and double excitations (MR-CISD). The fundamental form used for the DMBE fit reveals correct analytical properties [66–69] for the PES exhibiting a D_{3h} CI and is analytically continued to the first-excited electronic PES $(2^2A')$. A schematic diagram of the conically intersecting PESs of the ground electronic state of H_3 is shown in Fig. 1. The two JT split PESs are shown by red colored (V_-) and blue colored (V_+) lines, respectively for the D_{3h} geometry.

Although the DMBE PES is derived from a relatively small number of *ab initio* points, it is accurate enough as revealed by further *ab initio* calculations [25] and justifiably used in the literature to simulate the nuclear motion of H_3 [26]. Till date, the DMBE PES is the only one available which globally represents both the lower and upper adiabatic sheets of the ground electronic manifold of H_3. Wu *et al.* reported a new surface based on spline fits of the exact quantum Monte Carlo calculations [70]. All the surfaces mentioned above are constructed based on the same initial *ab initio* data points with different sets of additional data points for each surface. Recently, Mielke *et al.* [71] reported a set of three PESs for the hydrogen exchange reaction using a hierarchical set of electronic basis. These were subsequently used to estimate the complete basis set limit of

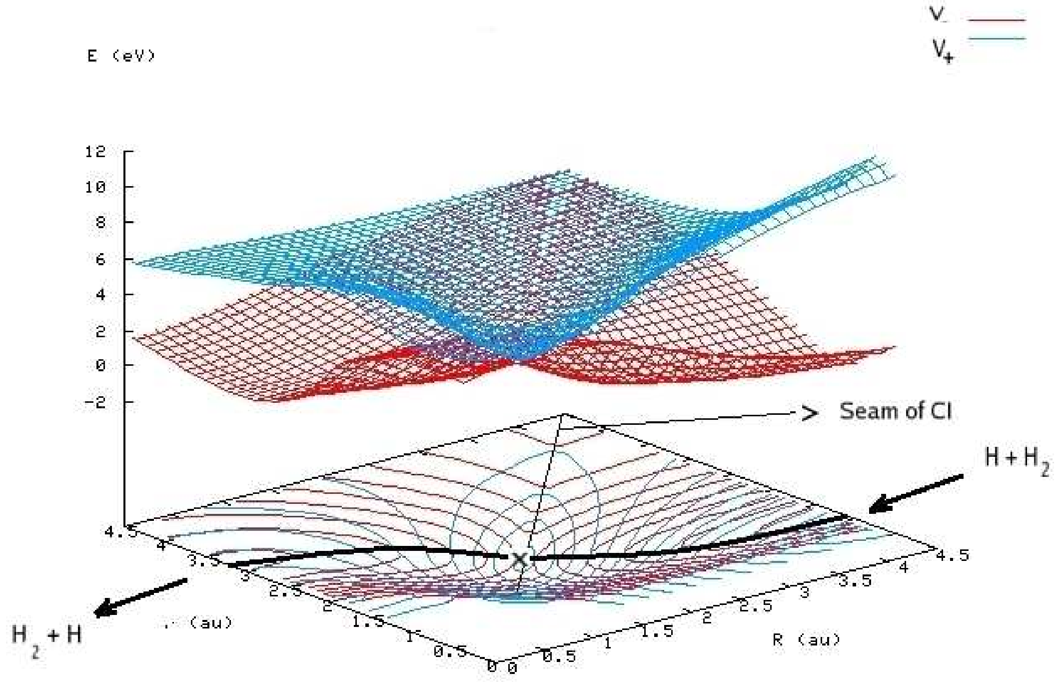

Figure 1.1: Adiabatic PESs of ground (shown by red colored contours) and first excited electronic states (shown by blue colored contours) of H_3 for D_{3h} geometry. The point of CI is shown by X in the figure.

the calculations, generating a fourth surface, named CCI surface [71].

1.1.2 Nonadiabatic effects in $H + H_2$ reaction

As discussed above that the hydrogen exchange reaction takes place on the JT split PES, and hence a study of the electronic nonadiabatic effects on the nuclear dynamics of this fundamental reaction has become an important topic of research in recent times [25, 72–78]. The orbital degeneracy of the electronic ground state of H_3 is split when it is distorted from its equilibrium D_{3h} configuration along its degenerate asymmetric stretching and bending vibrational modes. The resulting two JT split PESs form CIs at the D_{3h} equilibrium configuration of H_3 [4]. The possible effects of CIs on the nuclear dynamics of this system had initiated considerable debates in the literature [25,72,75–83], which could be resolved partially only in the recent years [25, 72, 73].

The effects of CIs on the molecular spectroscopy and later on reaction dynamics are well studied in literature in terms of GP change of adiabatic electronic wavefunction when encircling the CI in a closed path. The GP effect was first identified in a molecular system by Herzberg and Longuet-Higgins [4]. To make the total wavefunction single valued, one must either impose multivalued boundary conditions on the nuclear wavefunction, or one must make the electronic wavefunction complex and single valued by introducing a vector potential into the Hamiltonian [84]. The effect of GP on the bound vibrational energy level spectrum and more recently on the $H + H_2$ reaction dynamics have been studied at length [79, 85]. Early work on the GP effects in $H + H_2$ reaction was done by Mead [86]. He showed that the GP changes the relative phases of the inelastic and reactive contributions to fully symmetrized cross sections. Kupperman and coworkers have carried out extensive quantum reactive scattering calculations of the H + H_2 reaction and its isotopic variants [79–83] for collision energies less than the energetic minimum of the CIs of ~ 2.74 eV. The GP effects was found to change markedly the state-to-state rovibrational product distributions [79–83]. These results were found to be in better agreement with the earlier experimental measurements of these quantities [87]. Subsequent calculations that omit the GP change revealed an excellent agreement with the results of molecular beam experiments, based on the Rydberg atom time of flight technique at energies slightly above the minimum of CIs [88] establishing no noticeable GP effects on the hydrogen exchange reaction.

The absence of detectable GP effects in all the high resolution experiments stimulated further theoretical calculations. Recently, Kendrick [89–93] has carried out extensive theoretical investigations on the role of GP effects on the reactivity of the H + H_2 reaction and its isotopic variants. The important outcome of these theoretical studies [89–93] is that the GP effects cancel out in all of the state resolved integral and differential cross sections, when the contributions of odd and even values of the total angular momentum are added together. These studies were done using the LSTH and BKMP2 PESs and cancellation was found in both the cases [89–93]. This cancellation seems to be due to a symmetry property, independent of the PES and holds for all values of J. The results of these calculations did not agree with the previous ones [79–83].

The influence of GP on the reactive scattering dynamics of the H + H_2 system has been further considered and analyzed by an entirely different approach by Althorpe and coworkers [75,76]. These authors have carried out WP calculations on the hydrogen exchange reaction over the 0.4 - 2.5 eV total energy range using the BKMP2 PES, both with and without the inclusion of the GP effects [76]. The results obtained by them are in excellent agreement with those of Kendrick

[89–93] showing that the GP effects are observable in the state-to-state reaction probabilities but cancel exactly when the contributions from different partial waves of J are summed to obtain the integral reaction cross sections. Their results are also consistent with those of Kendrick [89–93] in predicting that there are no significant GP effects in the full differential reaction cross sections at energies below 1.8 eV, and in the partial differential cross sections at energies above this. In addition to this, they also observed small GP effects in the full differential cross sections above 1.8 eV [76] (which was not reported by Kendrick) which may be experimentally observable. In subsequent studies [77,78], Althorpe and coworkers have explained this cancellation by showing that the nuclear wavefunction around a CI branches into even and odd components (with a sign change that depends on the GP) and these two components can further interfere and thus contribute to the partial cancellation of the GP effects in the reaction cross sections. In the recent past, Mahapatra *et al.* [25] have studied the role of CIs on the hydrogen exchange reaction by explicitly including the coupling between the two sheets of the JT split ground electronic PES for the first time. In this work, the authors have computed the initial state-selected total reaction probabilities for $J = 0$ by a time-dependent WP method. This work represents the inclusion of the GP change and the nonadiabatic coupling in the reaction dynamics in a consistent fashion. They have calculated the reaction probabilities for energies upto the onset of the three-body dissociation of H_3 and found a very minor impact of nonadiabatic coupling on the reaction dynamics for $J = 0$.

The GP change also shown to have a negligible effect on the transition state resonances in the $H + H_2$ reaction [85]. Due to the fact that the CIs occur at the D_{3h} equilibrium geometry of H_3, understandably the saddle point resonances are not affected by the strong nonadiabatic effects. While the $H + H_2$ reaction dynamics has not yet been proved to be dramatically influenced by the GP effects, the direct evidence of the strong nonadiabatic effects in the H_3 system and its isotopic variants emerged from the neutralized ion-beam experiment of Bruckmeier *et al.* [94, 95]. The latter probed these systems in the close proximity of the seam of CIs. GP change, understandably accounts for a part of the nonadiabatic interactions and a more complete study (including the full nonadiabatic coupling) by Mahapatra *et al.* have unambiguously established the importance of nonadiabatic effects in the Rydberg emission spectra of H_3 and its isotopomers in conjunction with the experimental observations [96].

1.2 Bimolecular atom-diatom insertion reactions

The bimolecular atom-diatom insertion reactions of the type, X + H_2 [X is O(^1D), C(^1D), N(^2D) and S(^1D)] follow an indirect mechanism and are characterized by the presence of deep well on their PES. A common characteristic of these insertion reactions is that the deep potential well between reactants and products is associated with strongly bound species which is formed after the insertion of the incoming atom (X) into the H - H bond, *i.e.,* XH_2 (e.g., H_2O, CH_2, NH_2 and H_2S) molecules are formed. Among these molecules, H_2O and H_2S are formed in their ground electronic state and CH_2 (a^1A') and NH_2 (X^2B_1) are the radicals. Because of the presence of a very deep well, accurate QM scattering calculations are quite cumbersome and approximate methods such as quasiclassical trajectory (QCT) or reduced dimensionality QM calculations have been mostly used together with time-dependent methods to calculate the dynamical quantities of these reactions. As these reactions are believed to proceed statistically because of the stability of the intermediate complex with respect to reactants and products, a number of statistical studies are carried out in the literature [97–99]. Accurate QM calculations have appeared quite recently [100–102]. Each of the reaction has its own peculiarities and among these, the reaction of N(^2D) atom with the H_2 molecule is considered and studied in here.

1.2.1 The N (^2D) + H_2 insertion reaction

The N(^2D) + H_2 ($X^1\Sigma_g^+$) $\rightarrow$ NH ($X^3\Sigma^-$) + H (^2S) reaction represents a prototype for insertion reactions. It has been studied both experimentally and theoretically over the past few decades due to its important role in atmospheric and dark zone chemistry of propellant combustion [103]. In former times, dynamics of this reaction has been studied using a London-Eyring-Polanyi -Sato type of PES by Suzuki *et al.* [104] first, and then employing a more realistic one of Sorbie-Murrell type derived from *ab initio* electronic structure data [105]. Both these studies concluded that the reaction takes place via hydrogen atom abstraction, in agreement with previous experimental results [106]. However, more advanced experimental studies using laser induced fluorescence [107,108] and crossed molecular beam [109] techniques indicate that the reaction proceeds via an insertion type of mechanism. This apparent controversy could be resolved with the availability of more refined global *ab initio* PES for the 1 $^2A''$ electronic ground state of NH_2 reported by Ho *et al.* [110]. The topography of this PES reveals that the reaction proceeds via an approach of the nitrogen atom perpendicular to the H_2 bond [110]. This PES supports two barriers of height $\sim$ 0.21 eV and $\sim$ 0.08 eV, respectively, for the linear and T - shaped approaches and a well of depth $\sim$ 5.5 eV for the latter C_{2v} configuration [110].

QCT calculations based on the above PES show good agreement with the more recent experimental data [107–109]. Lin *et al.* [111] reported quantum dynamical results employing the 1 $^2A''$ PES of Ho *et al.* [110]. Initial state-specific integral reaction cross sections (up to the collision energy of $\sim$ 0.25 eV) and thermal rate constants are reported by these authors. In this study the authors have included partial wave contributions up to $J = 29$ to calculate the integral reaction cross sections. The calculated thermal rate constants turned out to be slightly larger than the experimental results and these results also show that the QCT method underestimates the observed rate coefficients. They also reported state-to-state differential and integral cross sections [112,113] of this reaction using same PES [110]. An *ab initio* PES for the 1 $^2A''$ electronic state based on the DMBE method has also been reported by Poveda *et al.* [114]. These authors also performed quantum dynamical studies using this PES [115] and reported the initial state-selected and energy resolved reaction probabilities, integral reaction cross sections and thermal rate constants. The rate constants obtained by these authors are slightly smaller than the experimental results [115]. Very recently Castillo *et al.* [116] have reported quantum WP and classical trajectory studies of this reaction and its isotopic variants on the 1 $^2A''$ PES of Ho *et al.* [110]. These authors have calculated the initial state-selected reaction probabilities and product rotational distributions for the total angular momentum $J = 0$ by using a real WP propagation method [117] up to a collision energy of $\sim$ 1.0 eV. Integral reaction cross sections (up to collision energy $\sim$ 0.25 eV) and thermal rate constants have been calculated from the $J = 0$ reaction probabilities by using the standard J-shifting [118], uniform J-shifting [119] approximations and also using the coupled states approximations for $J > 0$. The thermal rate constant data obtained by these authors are in good agreement with experimental results [116]. All these theoretical studies revealed oscillatory structures in the initial state-selected reaction probabilities and integral reaction cross sections as a function of collision energies. The oscillatory structures bear the signature of long lived complex (NH_2) formation during the course of the reaction.

1.2.2 Potential energy surface for the N (^2D) + H_2 reaction

There are many PESs available for the N(^2D) + H_2 reaction, but the first PES for the ground state $1\ ^2A''$ of NH_2 which supported the insertion type of mechanism appeared in 1999 [120]. This PES is based on high quality *ab initio* data and within the framework of the reproducing kernel Hilbert space (RKHS) theory [121–123]. This PES has been used in various QM and QCT studies of dynamics of the N(^2D) + H_2(D_2, HD) reactions and its high quality is evident from the good agreement found between the theoretical calculations and the corresponding experimental measurements. But this PES contains spurious small scale structures (of magnitude smaller than 1.0 Kcal/mol) at large separations and fails to give proper values at and near collinear geometries H-N-H. Also this surface does not describe the C_{2v} transition state and the N-H-H linear barrier regions correctly.

Ho *et al.* [110] have reported an improved version of this PES based a large set of data points resulting from the multireference configuration interaction (MRCI) calculations. This new PES is based on a set of 2715 *ab initio* points resulting from the MRCI calculations. This implementation is carried out using the RKHS interpolation method. A fast algorithm, with the help of low-order spline reproducing kernels, is implemented for the computation of the PES, which is essential for the large scale calculations of the dynamics. This PES removes all the shortcomings of the previous surface [120] and correctly describes the C_{2v} transition state [see Fig. 4]. We have utilized it in our dynamical calculations reported

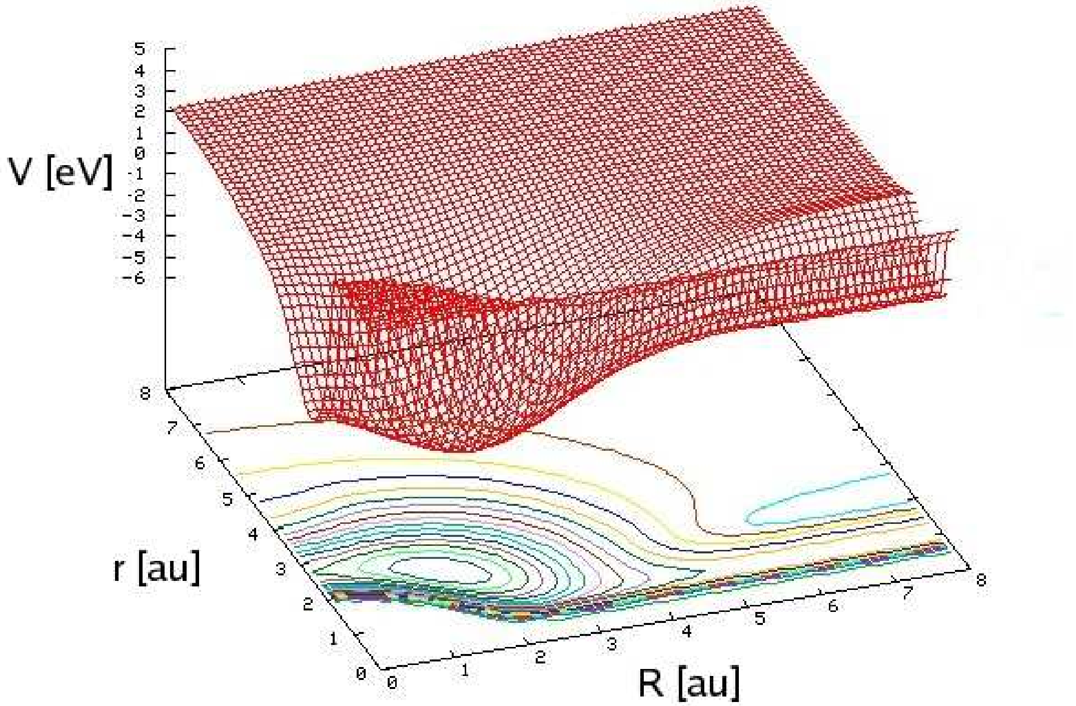

Figure 1.2: Schematic representation of the adiabatic potential energy surface [110] of the electronic ground state ($1^2A''$) of the N (^2D) + H_2 system for the C_{2v} arrangements of the three nuclei.

below. Recently, a new *ab initio* PES of the X^2A'' ground electronic state of NH_2 has been reported by Zhou *et al.* [124]. This is a global PES constructed by a three-dimensional cubic spline interpolation of more than 20000 *ab initio* points, which were calculated at MRCI level with Davidson correction using augmented correlation-consistent polarized valence quadruple-zeta basis set.

1.2.3 Nonadiabatic effects in N (^2D) + H_2 reaction

The ground 1 $^2A''$ and first excited 2 $^2A'$ electronic states of NH_2 transform into a degenerate $^2\Pi$ state for linear configurations and thus interact through RT type of vibronic coupling. NH_2 is the first molecular system where RT effects were observed [125]. Santoro *et al.* [126] have investigated the RT effect in the collision dynamics of NH_2 using a trajectory-surface-hopping approach. Recently, Defazio *et al.* [127] have studied the RT dynamics of the title reaction using a J - shifting approximation on the PES reported by Santoro *et al.* [126]. These authors have reported state resolved reaction probabilities, cross sections and thermal rate constants paying special attention to the RT effects. Very recently, the experimental rate constants for the NH ($a^1\Delta$) + H and ND ($a^1\Delta$) + D reactions have been measured using a quasi-static laser flash photolysis/ laser-induced fluorescence technique [128]. The findings of this experiment are corroborated in a theoretical analysis using a simple surface-hoping approach to reveal the impact of RT coupling on the reaction dynamics on the excited electronic state [128].

1.3 Current state of research and the aim of the present work

Recently, Varandas *et al.* have studied the nonadiabatic effects in the H + D_2 reaction [129]. These authors have reported the state-to-state dynamics of the H + D_2 reaction by the reactant-product decoupling method. These authors have calculated rotational distributions for the reaction H + D_2 $(v = 0, j = 0) \rightarrow$ HD$(v' = 3, j' = 0)$ at eight different collision energies between 1.49 and 1.89 eV. These authors have not found any major nonadiabatic effects in their results. Initial state-selected total reaction probabilities and integral reaction cross sections are also reported for energies ranging from 0.25 upto 2.0 eV and no significant nonadiabatic effects are observed in the dynamical results. Althorpe and coworkers have studies the effect of GP in the state-to-state opacity functions of the hydrogen exchange reaction, which cancel out in the state-to-state integral reaction cross sections [76]. Recently, Althorpe and coworkers have studied the effect of GP on the state-to-state dynamics of H + H_2 reaction upto the total energies of $\sim$ 4.5 eV above the ground state potential minimum [130]. These authors have found that the upper electronic state makes only a very small contribution to the state-to-state dynamics, even at energies much higher than the minimum of CIs. At total energies above 3.5 eV, many of the state-to-state reaction probabilities show strong GP effects. These effects are found to survive the coherent sum over partial waves to produce features in the state-to-state differential cross sections which could be detected in an experiment with an angular resolution of $\sim 20^o$ [130]. The effect of coriolis coupling (CC) in the state-to-state differential and integral reaction cross sections for the H + D_2 reaction on the BKMP2 surface [61] in the total energy range of 0.4 - 1.2 eV with D_2 initially in its ground vibrational-rotational state has been studied by Chu *et al.* [131] using the DIFFREALWAVE code [132]. These authors have compared the results from calculations including the full CC and those using the centrifugal sudden (CS) approximation. They showed that the energy dependence and the angular dependence of the calculated cross sections are sensitive to the coriolis coupling, which emphasizes the importance of the CC in the accurate state-to-state dynamical calculations. Recently, Defazio *et al.* have studied the effect of CC on the initial state-resolved dynamics the N(^2D) + H_2 insertion reaction, with and without including nonadiabatic RT interactions between the NH_2 X $^2B_1$ and A $^2A_1$ electronic states [133]. These authors have found that the CC effects are rather small up to $J = 40$ when the RT interactions are excluded and the CS approximation is found to be sufficient in this case. On the otherhand, RT effects are associated with large CC effects near the linearity of NH_2, and the accuracy of the CS approximation breaks down at high collision energies, when the reaction starts on the excited state.

The aim of the present work is to investigate the effects of the CIs and the associated nonadiabatic effects in the H + H_2 (and its isotopic variants) reaction. An examination of the details of the N(^2D) + H_2 reaction dynamics is also planned. The initial state - selected and energy resolved reaction probabilities, integral reaction cross sections and thermal rate constants have been calculated for both H + H_2 (and its isotopic variants) and N(^2D) + H_2 reactions. The effect of the CC on the coupled state dynamics of the hydrogen exchange reaction is also investigated. The calculated thermal rate constants are compared with the available theoretical and experimental results. The effect of JT CIs in the 3p (E') and 3d (E'') Rydberg electronic states of triatomic hydrogen has been investigated in an attempt to understand the DR processes of H_3.

1.4 Overview of the Thesis

In Chapter 2, we present a detailed description of the theoretical framework to deal with nuclear dynamics in the coupled-state situation by a TDWP approach. The nuclear dynamics is treated with a two-state model Hamiltonian. The flux operator is represented in both adiabatic and diabatic representations to calculate the initial state-selected and energy resolved reaction probabilities. Initial state-selected and energy resolved integral reaction cross sections are calculated by summing up all the necessary partial waves depending on the total angular momentum, J within the coupled state approximations and also including the CC terms in the Hamiltonian. The thermal rate constants are calculated from the integral reaction cross sections.

In Chapter 3, we present and discuss the reaction probabilities, integral reaction cross sections and thermal rate constants obtained for H + H_2 and its isotopic variants using the theoretical formalism described in chapter 2. The reaction probabilities are calculated both in the uncoupled and coupled surface situations, respectively. All partial wave contributions upto the total angular momentum, $J = 50$ (60, in case of H + HD) are calculated. The reaction probabilities depending on the total angular momentum J are summed up using the CS approximation to calculate the integral reaction cross sections. The thermal rate constants are calculated by Boltzman averaging over the reagent rotational angular momentum quantum number, j.

In chapter 3, we also present and discuss the effect of the reagent rotation and vibration on the dynamics of the H + H_2 reaction when the reagent is in its $(v = 0, j = 0 - 10)$ and $(v = 0 - 10, j = 0)$ states. We calculate the reaction probabilities upto the three-body dissociation limit of H_3 both in coupled and uncoupled states situation, respectively. The integral reaction cross sections have been calculated by summing over all partial waves upto $J = 50$, in both coupled and uncoupled surface situations, respectively. The observed nonadiabatic effects on the dynamical attributes are discussed at length.

In chapter 4, we present and discuss the reaction dynamics of the prototypical insertion reaction, N(^2D) + H_2. The initial state-selected total reaction probabilities are calculated for the title reaction up to the collision energy of 1.0 eV. All partial waves up to the total angular momentum, $J = 60$ are included to obtain converged integral reaction cross sections. The thermal rate constants are calculated by Boltzman averaging of the initial state specific rate constants over reagent rotational angular momentum quantum number, j. The large number of vibrational levels supported by the NH_2 PES for the C_{2v} geometry are calculated and analyzed. The eigenfunctions of some of the low lying energy levels are calculated and assigned with the nodal pattern. A statistical analysis of these vibrational levels is also undertaken.

In chapter 5, we study the static and dynamic aspects of the JT conical interactions in the 3p (E') and 3d (E'') Rydberg electronic states of the H_3 theoretically. The static aspects are discussed based on recent *ab initio* quantum chemistry results, and the dynamic aspects are examined in terms of the vibronic spectra and nonradiative decay behavior of these states. The adiabatic PESs are diabatized and the nuclear dynamics is studied on the resulting conically intersecting manifold of electronic states by a time-dependent WP approach. Calculations are performed both in coupled and uncoupled surface situations in order to understand the importance of the nonadiabatic interactions due to JT CIs in these excited Rydberg electronic states.

Finally, the summarizing remarks including the future directions are provided in chapter 6.

Chapter 2

Quantum dynamics on coupled electronic states

2.1 Introduction

This chapter describes the theoretical formalism to study the dynamics of a bimolecular reaction occurring on a coupled manifold of electronic states. The nuclear dynamics is studied with a two-state model by representing the flux operator both in the adiabatic as well as in a diabatic electronic basis. The reaction is initiated in the adiabatic electronic representation and then monitored by numerically solving the TDSE in a diabatic electronic representation to avoid the diverging kinetic coupling terms of the former representation [25]. The observables are finally calculated in either of the two representations. The complexity of defining a suitable adiabatic-to-diabatic transformation angle, increases with an increase in the number of participating electronic state. A numerical diagonalization of the electronic Hamiltonian matrix is often undertaken to approximately describe the adiabatic-to-diabatic transformation matrix. For an explicitly time-independent Hamiltonian, the solution of the TDSE reads

$$|\Psi(t)\rangle = \exp\left[\frac{-i\hat{H}t}{\hbar}\right]|\Psi(t=0)\rangle \tag{2.1}$$

where, $|\psi(t)\rangle$ is the wavefunction at time t, and $\hat{H}$ defines the Hamiltonian operator of the reacting system.

2.2 Hamiltonian

The diabatic Hamiltonian for the ground electronic manifold, for example, of the H + H_2 system can be written as

$$H^d = T_N \begin{pmatrix} 1 & 0 \\ 0 & 1 \end{pmatrix} + \begin{pmatrix} U_{11} & U_{12} \\ U_{21} & U_{22} \end{pmatrix} \tag{2.2}$$

where, T_N represents the nuclear kinetic energy operator, which is diagonal in this basis. In terms of the mass-scaled body-fixed (BF) Jacobi coordinates R (the distance of the hydrogen atom to the center of mass of the diatomic reagent molecule), r (the internuclear distance of the reagent molecule) and γ (the angle between $\vec{R}$ and $\vec{r}$) [see Fig. 3] and for total angular momentum $\mathbf{J} \neq 0$, it is given by

$$T_N = -\frac{\hbar^2}{2\mu}\left[\frac{\partial^2}{\partial R^2} + \frac{\partial^2}{\partial r^2}\right] + \frac{\hat{j}^2}{2\mu r^2} + \frac{\hat{l}^2}{2\mu R^2}. \tag{2.3}$$

In Eq. (2.3), the operator $\hat{j}$ defines the diatomic rotational angular momentum associated with the Jacobi angle γ, and $\hat{l}$ is the orbital angular momentum operator. The quantity, $\mu = \sqrt{(m_H m_H m_H)/(m_H + m_H + m_H)}$, is the three-body

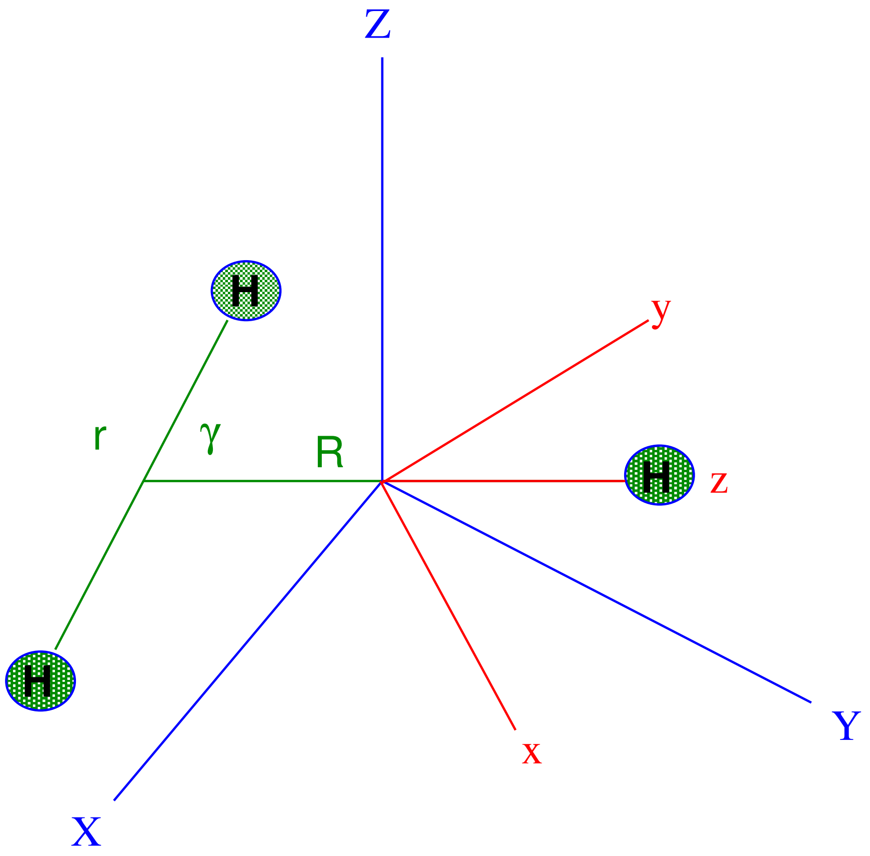

Figure 2.1: The center-of-mass coordinates for the H + H_2 collision used in the space-fixed and body-fixed frame are represented as XYZ (blue) and xyz (red) axes, respectively. The coordinate origin is at the center of mass atom-diatom system.

scaled reduced mass and quantities U_{11} and U_{22} in Eq. (2.2) are the energies of the two diabatic electronic states and, $U_{12} = U_{21}$ represent their coupling potential. The BF z-axis is defined to be parallel to $\hat{R}$ and the diatom lies in the (x, z) plane [see Fig. 2.1].The quantity $\hat{l}^2$ is expressed as

$$\hat{l}^2 \equiv (\hat{J} - \hat{j})^2 = \hat{J}^2 + \hat{j}^2 - 2\hat{J}_z\hat{j}_z - \hat{J}_+\hat{j}_- - \hat{J}_-\hat{j}_+ \tag{2.4}$$

where, $\hat{J}$ is the total angular momentum operator and $\hat{J}_z$ and $\hat{j}_z$ are the respective BF z components of $\hat{J}$ and $\hat{j}$. $\hat{J}_+(\hat{J}_-)$ and $\hat{j}_+(\hat{j}_-)$ are the corresponding raising (lowering) operators. Within the coupled states or centrifugal sudden approximation (CS) [135, 136] the last two terms of Eq. 2.4 are neglected. The elements of the diabatic electronic Hamiltonian matrix of Eq. (2.2) are obtained by diabatizing the adiabatic electronic Hamiltonian matrix through the following similarity transformation:

$$\begin{pmatrix} U_{11} & U_{12} \\ U_{21} & U_{22} \end{pmatrix} = \mathcal{S} \begin{pmatrix} V_- & 0 \\ 0 & V_+ \end{pmatrix} \mathcal{S}^\dagger \tag{2.5}$$

$$= \frac{V_- + V_+}{2}\mathbf{1} + \frac{V_+ - V_-}{2} \begin{pmatrix} -\cos\chi & \sin\chi \\ \sin\chi & \cos\chi \end{pmatrix}, \tag{2.6}$$

with

$$\mathcal{S} = \begin{pmatrix} \cos\phi & \sin\phi \\ -\sin\phi & \cos\phi \end{pmatrix}. \tag{2.7}$$

The quantities V_- and V_+ represent the JT-split lower and upper adiabatic sheets of the DMBE PES [59], and S defines the unitary transformation matrix from the adiabatic-to-diabatic representation; $\Psi^{diab} = \mathcal{S}\ \Psi^{adiab}$; ϕ is the adiabatic-to-diabatic mixing angle. The quantity χ $(= 2\phi)$ above is the pseudorotation angle defined to be the polar angle of the e-type vibration in the two-dimensional vibrational subspace of the system. It has been demonstrated that this scheme of diabatization removes the leading singular derivative coupling of the adiabatic electronic representation and is able to yield quantitative experimental information [23, 24].

In the adiabatic representation the electronic part of the Hamiltonian is diagonal and the nonadiabatic coupling elements appear as off-diagonal elements in the nuclear part of the Hamiltonian. The adiabatic Hamiltonian matrix can be obtained from the diabatic one of Eq. (2.2) using the above $\mathcal{S}$ matrix:

$$\begin{aligned} H^{ad} &= S^{\dagger} H^{d} S \\ &= T_N \mathbf{1} - S^{\dagger}[T_N, S] - \begin{pmatrix} V_- & 0 \\ 0 & V_+ \end{pmatrix}, \end{aligned} \tag{2.8}$$

where T_N represents the nuclear kinetic energy operator given in Eq. 2.3.

2.3 Preparation of the initial WP

In a reactive scattering study the initial wavefunction is prepared in the asymptotic reactant channel where the interaction potential almost vanishes. In such a situation the initial wavefunction pertinent to the reacting system can be written as a product of the translational wavefunction $F(R)$ for the motion along R and the rovibrational wavefunction Φ_{vj} of the reagent molecule. We locate the wavefunction initially on the repulsive lower adiabatic sheet (V_-) of the DMBE

PES [59] of H_3 which assumes the form

$$|\Psi^J_\Omega(R_l, r_m, \gamma_n, t=0)\rangle \;=\; \sqrt{\omega_n} F(R_l)\phi_{vj}(r_m)\tilde{P}^\Omega_j(\cos\gamma_n). \tag{2.9}$$

where R_l, r_m and γ_n are the grid points in the (R, r, γ) space. The quantity Ω is the quantum number for the projection of j (and also J) on the BF z axis. We choose a minimum uncertainty Gaussian wave packet (GWP) for $F(R)$:

$$F(R) = \left(\frac{1}{2\pi\delta^2}\right)^{\frac{1}{4}} \exp\left[-\frac{(R-R_0)^2}{4\delta^2} - ik_0(R-R_0)\right]. \tag{2.10}$$

The quantity δ is the width parameter of the GWP, and R_0 and k_0 correspond to the location of its maximum in the coordinate and momentum space, respectively. The functions ϕ_{vj} represent the rovibrational eigenfunctions corresponding to a given vibrational v and rotational j levels of the reagent molecule. The sine discrete variable (sine-DVR) representation approach of Colbert and Miller [137] is used to solve the rovibrational eigenvalue equation for ϕ_{vj} :

$$\left[-\frac{\hbar^2}{2\mu'}\frac{d^2}{dr'^2} + V(r') + \frac{j(j+1)\hbar^2}{2\mu' r'^2}\right]\phi_{vj}(r') = \epsilon_{vj}\phi_{vj}(r'). \tag{2.11}$$

Here μ' is the reduced mass, ϵ_{vj} is the energy eigenvalue, and $r' = r(\mu/\mu')^{1/2}$, the unscaled internuclear distance of the reagent molecule. $V(r')$ is its potential energy obtained from the DMBE PES [59] by setting $R \to \infty$. The initial wavefunction defined in Eq. (2.9) is transformed to the diabatic electronic representation by using the S matrix (Eq. (2.7)) prior to the propagation. In the diabatic electronic representation the initial wavefunction can be written in the vector notation as

$$\Psi^d(R,r,\gamma,t=0) \;=\; \psi_1^d(R,r,\gamma,t=0)\begin{pmatrix}1\\0\end{pmatrix}+\psi_2^d(R,r,\gamma,t=0)\begin{pmatrix}0\\1\end{pmatrix} \quad (2.12)$$

where $\begin{pmatrix}1\\0\end{pmatrix}$ and $\begin{pmatrix}0\\1\end{pmatrix}$ indicate the first and the second diabatic electronic state with energy U_{11} and U_{22}, respectively.

2.4 Time evolution of the initial WP

The general solution of the TDSE [Eq. (2.1)] is given by

$$\Psi(t) = \hat{P}\exp\left[-i\hbar\int_0^T \hat{H}(t')dt'\right]\Psi(0) \quad (2.13)$$

where, $\Psi(0)$ and $\Psi(t)$ are the wavefunctions at time 0 and t, respectively. $\hat{P}$ is the time ordering operator. For an explicitly time-independent Hamiltonian, the solution reads as in Eq. (2.1). The exponential operator in the R.H.S.of the Eq. (2.1) forms a continuous dynamical group where time t is a parameter, and is known as the time-evolution operator denoted by $\hat{U}(t,t_0)$. For $t_0=0$,

$$\hat{U}(t,t_0) = e^{-i\hat{H}t/\hbar}. \quad (2.14)$$

Time t is divided into smaller steps of length Δt and the evolution for the entire range of time is accomplished through:

$$\hat{U}(t) \;=\; \Pi_{n=0}^{N_{t-1}}\hat{U}((n+1)\Delta t, n\Delta t) \quad (2.15)$$

where, N_t is the total number of time steps and, $\Delta t = t/N_t$ is the step length. $\hat{U}(t, t_0)$ is a linear operator and is unitary:

$$\hat{U}\hat{U}^\dagger = \hat{U}^\dagger\hat{U} = \mathbf{1} \tag{2.16}$$

The exponential operator is approximated in various ways in the literature. For example, the second order differencing (SOD) scheme [138], the split operator (SO) operator [139], the chebyshev polynomial (CP) scheme [140] and the short iterative Lanczos (SIL) scheme [141] represents a few of them. For the present investigations, we have used the chebyshev polynomial scheme for time evolution [140]. Chebyshev polynomials are found to be superior to many other polynomials and are optimal for a scalar function $F(x)$ bounded in the interval [-1,1]. So, a scalar function like e^{ax} can be expressed in terms of these polynomials in the interval -1$\leq x \leq 1$ as

$$e^{ax} = \sum_{n=0}^{\infty}(2 - \delta_{n0})J_n(\alpha)T_n(x), \tag{2.17}$$

where δ_{n0} is the Kroenecker delta and, $\alpha = \Delta E\ \Delta t/2\hbar$. $J_n(\alpha)$ are the modified Bessel functions of order n. $T_n(x)$ are the Chebyshev polynomials of order n, calculated using the recursion relation [142]

$$T_{n+1}(x) = 2xT_n(x) - T_{n-1}(x) \tag{2.18}$$

with $T_0(x) = 1$ and $T_1(x) = x$.

The evolution operator is a function of an operator. It can be shown that a function of an operator can be expressed as a function of a scalar in the complete basis of the operator. So, the function of the operator can be approximated in the

Chebyshev series, provided the domain of the operator is confined to the interval [-1,1] in which the Chebyshev polynomials are optimal. In case of a Hamiltonian which is self-adjoint, the eigenvalues lie on a real axis, and they can be positioned from -1 to 1 by renormalizing the Hamiltonian as follows:

$$\hat{H}_{norm} = 2(\hat{H} - \overline{H})/\Delta E \tag{2.19}$$

where, $\overline{H} = (E_{max} + E_{min})/2$, and, $\Delta E = E_{max} - E_{min}$. In terms of this renormalized Hamiltonian, H_{norm}, the evolution operator can be written as:

$$e^{-i\hat{H}\Delta t/\hbar} = e^{-i\overline{H}\Delta t/\hbar} e^{-i\alpha \hat{H}_{norm}}. \tag{2.20}$$

The first term in the above equation is the phase shift due to the shift of the energy scale. The second term is approximated by the chebyshev series [140, 143, 144] as

$$e^{-i\alpha H_{norm}} = \sum_{n=0}^{\infty} (2 - \delta_{n0}) J_n(\alpha) \Phi_n(-i\hat{H}_{norm}) \tag{2.21}$$

where, $\Phi_n(-i\hat{H}_{norm})$ are the complex Chebyshev polynomials of order n satisfying the recursion relation:

$$\Phi_{n+1} = -2i\hat{H}_{norm}\Phi_n + \Phi_{n-1} \tag{2.22}$$

where, $\Phi_0 = 1$ and $\Phi_1 =$ -$i\hat{H}_{norm}$. Therefore, the evolution of $\Psi(t)$ in this scheme on a discrete grid is given by:

$$\Phi(t + \Delta t) = e^{-i\hat{H}\Delta t}/\hbar \sum_{n=0}^{N} (2 - \delta_{n0}) J_n(\alpha) \Phi_n(-i\hat{H}_{norm}) \Phi(t). \tag{2.23}$$

The number of terms to be used in the above expansion is estimated from the time-energy phase space volume α. In practice the number of terms used is slightly larger than this estimate for a good convergence. Since the evolution operator is expanded in a series of polynomials in the Chebyshev method, by definition the scheme is not unitary. The deviation from the unitarity corresponds to the remainder term in the expansion. This deviation provides as an accuracy check of the scheme. The errors are uniformly distributed in the bounded interval [143, 145]. Since Bessel functions show exponential convergence for $n > \alpha$, the error is usually very small.

The Eq. (2.20) is used in conjunction with the fast Fourier transform method (FFT) [146] to evaluate the action of the radial kinetic energy operator. The action of the rotational kinetic energy operator is carried out by transforming the discrete variable representation (DVR) [147] wavefunction, $|\Psi_{lmn}\rangle$ to the angular momentum space (finite basis representation (FBR)), multiplying it by the diagonal/off-diagonal value of the operator and transforming it back to the DVR representation [147]. Numerically this is accomplished in a single step as follows

$$\begin{aligned}
\hat{T}_{dia}(\gamma)|\Psi^{\Omega}_{lmn'}\rangle &= \sum_n \left\{ \sum_j \boldsymbol{U}^{\Omega}_{n',j}{}^{\dagger} \left\{ \frac{\hbar^2}{2}\left[\frac{j(j+1)}{I} + \frac{J(J+1)-2\Omega^2}{\mu R^2}\right]\right\} \boldsymbol{U}^{\Omega}_{j,n} \right\} |\Psi^{\Omega}_{lmn}\rangle, \\
\hat{T}^{\pm}_{off}(\gamma)|\Psi^{\Omega}_{lmn'}\rangle &= \sum_n \left\{ \sum_j \boldsymbol{U}^{\Omega\pm1\dagger}_{n',j} \left\{ \frac{\hbar^2}{2\mu R^2}\left[C^{\pm}_{J\Omega}C^{\pm}_{j\Omega}\right]\right\} \boldsymbol{U}^{\Omega}_{j,n} \right\} |\Psi^{\Omega\pm1}_{lmn}\rangle \qquad (2.24)
\end{aligned}$$

where, the quantity $\boldsymbol{U}_{j,n}$ represents the DVR-FBR transformation matrix and $\boldsymbol{U}^{\dagger}_{n,j}$ is the Hermitian conjugate to $\boldsymbol{U}_{j,n}$. $C^{\pm}_{J\Omega}$ and $C^{\pm}_{j\Omega}$ are the CC terms defined as

$$C^{\pm}_{J\Omega} = [J(J+1) - \Omega(\Omega \pm 1)]^{1/2}, \qquad (2.25)$$

where, J is the total angular momentum quantum number of the system and Ω

is the projection of J on the body-fixed axis.

As the WP moves forward in time, its fast moving components approach the grid boundaries and are no longer relevant for the rest of the dynamics [148]. Therefore, to avoid unphysical reflections or wrap around of these components from the boundaries of a finite sized grid, the WP at each time step is multiplied by a damping function [149]

$$f(X_i) = \sin\left[\frac{\pi}{2}\frac{(X_{mask} + \Delta X_{mask} - X_i)}{\Delta X_{mask}}\right], \qquad X_i \geq X_{mask} \tag{2.26}$$

which is activated outside the dividing line in the product channel and also in the asymptotic reactant channel. X_{mask} is the point at which the damping function is initiated and $\Delta X_{mask}(= X_{max} - X_{mask})$ is the width of X over which the function decays from 1 to 0, with X_{max} being the maximum value of X in that direction, in a particular channel.

2.5 Final analysis (Quantum flux operator approach)

The flux operator $\hat{F}$ is defined in terms of a dividing surface Θ which is the function of a suitable coordinate that separates the product from the reactants.

$$\hat{F} = \frac{i}{\hbar}\left[\hat{H}, \Theta\right], \tag{2.27}$$

where

$$\Theta = h(r - r_d). \tag{2.28}$$

The quantity h above is a heaviside step function which equals unity for a positive argument and zero otherwise. r_d is chosen far out in the product channel to ensure the asymptotic motion for all $r = r_d$. Since Θ depends only on coordinates the potential operator commutes with it and $\hat{F}$ is given by the commuter of Θ with T_N. The latter is diagonal in a diabatic electronic basis and hence $\hat{F}$. Whereas, in the adiabatic basis T_N is nondiagonal and therefore $\hat{F}$ also contains off-diagonal elements [25]. The reaction probability is the expectation value of the above flux operator in the basis of the energy normalized time-independent reactive scattering wave function evaluated at $r = r_d$. We write this wavefunction in the diabatic electronic basis as

$$|\Phi^d(R, r_d, \gamma, E)\rangle = \begin{pmatrix} |\phi_1^d(R, r_d, \gamma, E)\rangle \\ |\phi_2^d(R, r_d, \gamma, E)\rangle \end{pmatrix} \tag{2.29}$$

where ϕ_1^d and ϕ_2^d corresponds to the wavefunction components on the diabatic state 1 and 2, respectively.

2.5.1 Calculation of reaction probability

For an initial state i (corresponding to a specific vibrational v and rotational j state of the reagent diatom) the energy resolved reaction probability is given by [25]

$$\begin{aligned} P_i^R(E) = \sum_f |S_{fi}^R|^2 &= \langle \Phi^d(R, r_d, \gamma, E)|\hat{F}|\Phi^d(R, r_d, \gamma, E)\rangle \qquad (2.30) \\ &= \frac{\hbar}{\mu} \sum_{k=1}^{2} \mathrm{Im} \left[\langle \phi_k^d(R, r_d, \gamma, E)| \frac{\partial \phi_k^d(R, r_d, \gamma, E)}{\partial r} \rangle \right] |_{r=r_d}. \end{aligned}$$

The quantity in the right-hand side of the above equation is integrated over the entire range of R and γ. The energy normalized time-independent reactive scattering wavefunction is calculated along the dividing surface at, $r = r_d$ by

$$|\phi_k^d(R, r_d, \gamma, E)\rangle \;\; = \;\; |\psi_k^d(R, r_d, \gamma, E)\rangle/\kappa_E \tag{2.31}$$

The function $\psi_k^d(R, r_d, \gamma, E)\rangle$ is obtained by Fourier transforming the time-evolved WP $\psi_k^d(R, r_d, \gamma, t)\rangle$ along the dividing surface

$$|\psi_k^d(R, r_d, \gamma, E)\rangle \;\; = \;\; \frac{1}{\sqrt{2\pi}} \int_{-\infty}^{+\infty} e^{iEt/\hbar} |\psi_k^d(R, r, \gamma, t)\rangle dt|_{r=r_d}. \tag{2.32}$$

The quantity κ_E in Eq. (2.31) is the weight of the translational component $F(R)$ contained in the initial WP for a given total energy E

$$\kappa_E = (\frac{\mu}{2\pi\hbar k})^{1/2} \int_{-\infty}^{+\infty} F(R) e^{ikR} dR, \tag{2.33}$$

where $k = \sqrt{2\mu(E - \epsilon_{vj})}/\hbar$, with ϵ_{vj} being the initial ro-vibrational energy of the reagent molecule. For the present two state problem, the flux operator in the adiabatic electronic basis depends (see ref. [25] for details) only on the reaction coordinate (here r), so only the r-dependent part of the nuclear kinetic energy operator is of relevance in Eq. (2.30). The nuclear kinetic energy operator of the Hamiltonian in this basis is nondiagonal and consequently the flux operator possesses nondiagonal elements. We redefine the energy normalized time-independent reactive scattering wavefunction in the adiabatic electronic basis as

$$|\Phi^{ad}(R, r_d, \gamma, E)\rangle \quad = \quad \begin{pmatrix} |\phi_-^{ad}(R, r_d, \gamma, E)| \\ |\phi_+^{ad}(R, r_d, \gamma, E)\rangle \end{pmatrix} \tag{2.34}$$

where ϕ_-^{ad} and ϕ_+^{ad} represent the two components of this wavefunction on V_- and V_+, respectively. The reaction probability in the adiabatic electronic representation is then given by [25]

$$\begin{aligned} P_i^R(E) \quad = \quad & \frac{\hbar}{\mu}\left[\mathrm{Im} < \phi_-^{ad}(R, r_d, \gamma, E)|\frac{\partial \phi_-^{ad}(R, r_d, \gamma, E)}{\partial r} >\right] + \\ & \frac{\hbar}{\mu}\left[\mathrm{Im} < \phi_+^{ad}(R, r_d, \gamma, E)|\frac{\partial \phi_+^{ad}(R, r_d, \gamma, E)}{\partial r} >\right] + \\ & \frac{\hbar}{\mu}\left[2\mathrm{Im} < \phi_-^{ad}(R, r_d, \gamma, E)|\frac{\partial \phi_+^{ad}(R, r_d, \gamma, E)}{\partial r} >\right]. \end{aligned} \tag{2.35}$$

The probability expression in the adiabatic electronic basis, therefore, contains the off-diagonal electronic contributions in contrast to the same (Eq. (2.30)) in a diabatic electronic basis.

2.5.2 Calculation of reaction cross sections and thermal rate constants

The cumulative reaction probability for a given initial (v, j) state is calculated by summing up the reaction probability results for different partial wave contributions as follows [150]

$$N_{vj}(E) = \sum_{\Omega=0}^{j} \frac{g_\Omega}{(2j+1)} \sum_{J \geq \Omega}^{J_{max}} (2J+1) P_{vj}^{J\Omega}(E). \tag{2.36}$$

the quantity g_Ω is the degeneracy factor; $g_\Omega = 1$ for $\Omega = 0$, and $g_\Omega = 2$ for $\Omega \neq 0$. The total reaction cross section is given by

$$\sigma_{vj}(E) = \frac{\pi}{k^2} N_{vj}(E). \tag{2.37}$$

The initial state-selected thermal rate constant can be obtained from the total reaction cross section [151] as

$$K_{vj}(T) = \sqrt{\frac{8K_BT}{\pi\mu}} \frac{1}{(K_BT)^2} \int_0^\infty E\sigma_{vj}(E) e^{-E/K_BT} dE, \tag{2.38}$$

where K_B is the Boltzmann constant. Finally, the rotationally averaged thermal rate constants can be obtained by averaging over a Boltzmann distribution of such states

$$K_v(T) = \sum_j \frac{K_{vj}(E)}{Q_{rot}} (2j+1) e^{-Bj(j+1)hc/K_BT}, \tag{2.39}$$

where B is the rotational constant of the reagent and Q_{rot} is the rotational partition function given by

$$Q_{rot} = \sum_j (2j+1) e^{-Bj(j+1)hc/K_BT}. \tag{2.40}$$

Chapter 3

Nonadiabatic quantum wave packet dynamics of hydrogen exchange reaction and its isotopic variants

3.1 Introduction

In this chapter, we present and discuss the reaction probability, reaction cross section and thermal rate constant results obtained for the hydrogen exchange reaction and its isotopic variants, employing the theoretical methodology illustrated in chapter No. 2. The reaction probabilities are calculated upto the three-body dissociation limit of ~ 4.74 eV. In the CS [135,136] model inclusion of partial-wave contributions upto $J = 50$, for the H + H_2, H + D_2; D + H_2 reactions and upto $J = 60$, for the H + HD reaction, respectively, are found to be necessary to obtain converged cross section results in this energy range. Calculations are carried

Table 3.1: Numerical grid parameters and properties of the initial wavefunction used in the present study

Parameter	Value	Description
$N_R/N_r/N_\gamma$	128/64/48	Number of grid points
R_{min}/R_{max} (a_0)	0.1/15.34	Extension of the grid along R
r_{min}/r_{max} (a_0)	0.5/8.06	Extension of the grid along r
$\Delta R/\Delta r$ (a_0)	0.12/0.12	Grid spacings along R and r
r_d (a_0)	4.10	Location of the dividing surface in the product channel
R_{mask}/r_{mask} (a_0)	11.74 /4.70	Starting point of the masking function
R_0 (a_0)	10.5	Initial location of the center of the GWP in the coordinate space
E_{trans} (eV)	2.0	Initial translational kinetic energy
δ (a_0)	0.16	Initial width parameter of the GWP
Δt (fs)	0.135	Length of the time step used in the WP propagation
T (fs)	413.76	Total propagation time

out both with and without the coupling of PESs and the results are compared. Channel specific reaction attributes are reported in case of H + HD reaction. The convergence of each calculation is checked with respect to the choice of the numerical grid parameters given in Table 3.1.

The effect of reagent rotations and vibrations on the reactivity is also studied employing the CS [135, 136] approximation in this chapter. Initial state-selected and energy resolved reaction probabilities have been reported for the reagent, H_2 in its ($v = 0, j = 0 - 10$) and ($v = 0 - 10, j = 0$) levels. Integral reaction cross sections have been calculated from the reaction probabilities as discussed in chapter 2. Analysis of the reaction probability and reaction cross section data shows that the nonadiabatic effects are insignificant at small values of j and v, which become more pronounced with an increase of the latter quantities. Electronic nonadiabatic effects appear to be more important in the reaction dynamics of rotationally excited H_2. A more exact treatment of the dynamics including the coriolis coupling terms in the Hamiltonian (c.f., Eq. (2.4)) is also considered and some of the preliminary results are presented and discussed in case of H + H_2 exchange reaction. It is important to note that the uncoupled surface calculations refer to the treatment of the nuclear dynamics on the lower adiabatic sheet of the degenerate ground electronic state of H_3 without inclusion of any nonadiabatic or GP effects. The initial state selected rate constants are calculated from the integral reaction cross sections and Boltzman averaging of these rate constants over the reagent rotational levels, j yields thermal rate constants.

It is found that the reaction cross sections show only minor differences beyond the minimum of CIs occurring at $\sim$ 2.74 eV. These findings are consistent with the single surface calculations reported in the literature including the GP change of the wavefunction [75–78, 89–92]. In case of H + H_2 reaction, the cross section initially increases with increase in total energy and reaches a maximum of $\sim$ 2.5 $\AA^2$ at $\sim$ 2.5 eV and then decreases at higher energies. In case of H + D_2 reaction, the cross section initially increases reaching a maximum of $\sim$ 1.25 $\AA^2$ at $\sim$ 2.5 eV and then decreases at higher energies. In case of D + H_2 reaction, the cross section reaches to a maximum of around 2.5 $\AA^2$ at $\sim$ 2.5 eV and then decreases thereafter. The difference between the cross sections obtained with and without the PES coupling somewhat increases with the rotational excitation of the reagent diatom. The thermal rate constants computed in the coupled and uncoupled state situations differ only slightly. In case of H + HD reaction, the cross section initially increases with the total energy and reaches to a maximum of $\sim$ 1.6 $\AA^2$ at $\sim$ 3.5 eV and then decreases. In this case also the thermal rate constants calculated with and without PES coupling reveal only minor differences.

3.2 Results and Discussion

The results obtained for the H + H_2, H + D_2, D + H_2 and H + HD reactions are presented and discussed below. Within the CS approximation, all the partial wave contributions upto the total angular momentum $J = 50$ (60, in case of H + HD) are included to obtain the converged cross sections upto the three-body dissociation of H_3.

3.2.1 Computational details

The detailed theoretical framework and computational methodology to treat the reaction dynamics by the TDQM approach is outlined in Chapter 2. We describe below few essential points. The TDSE [Eq. (2.1)] is solved numerically on a grid in the (R, r, γ) space using the matrix Hamiltonian of Eq. (2.2). In a reactive scattering study the initial wavefunction is prepared in the asymptotic reactant channel where the interaction potential almost vanishes. In such a situation the initial wavefunction pertinent to the reacting system can be written as a product of the translational wave function for the motion along R, rovibrational wavefunction for the motion along r and the angular basis functions for the motion along γ. This initial wavefunction is located on the repulsive lower adiabatic sheet (V_{-}) of the DMBE PES of H_3 [59].

A coordinate grid consisting of 128 × 64 × 48 points in the R, r and γ space with R ranging between 0.1 a_0 to 15.34 a_0 and r ranging from 0.5 a_0 to 8.06 a_0. The grid along γ is taken as the nodes of a 48-point Gauss Legendre Quadrature (GLQ) [153] for each value of Ω. For the latter purpose, the matrix of the $\cos(\gamma)$ operator in the basis of the associated Legendre polynomials is diagonalized. The resulting diagonal elements define the nodes of a n-point Gauss Legendre quadrature [153] and the DVR to the FBR transformation matrix is given by the eigenvector matrix U. The quadrature weight associated with the grid points are calculated by $w_n^{1/2} = \sqrt{\frac{2^{\Omega+1}\Omega!}{(2\Omega+1)!!}} \sin^{-\Omega}(\gamma_n)U_{1n}$, where U_{1n} refers to the first row of U (the lowest value of j, i.e., $j = \Omega$). The action of the rotational kinetic energy operator is then carried out by transforming the DVR wavefunction to the angular momentum space (FBR), multiplying it by the diagonal value of the angular kinetic energy operator, and transforming it back to the DVR representation.

3.2.2 Reaction Probability and Time Dependence of Electronic Population

The H + H_2 ($v = 0$, $j = 0$) → H_2 ($\sum v', \sum j'$) + H reaction probability values as a function of the total energy E (H, H_2 translational + H_2 rovibrational) are plotted in Fig. 3.1 (a) for a few selected values of the total angular momentum, J = 0, 10, 20, 30, 40 and 50 (indicated in the panel) and for $\Omega = 0$. These represent the initial state selected and energy resolved total (summed over all open v' and j' levels of the product H_2 at a given energy) reaction probabilities. The coupled and uncoupled surface results are shown by the solid and dashed lines, respectively. The reaction probabilities in both cases are calculated for the entire relevant energy range starting from the onset of the reaction to the three body break-up limit of ∼ 4.74 eV. The energy distribution of the translational GWP used in the initial WP is shown in Fig. 3.1 (b). It can be seen from Fig. 3.1 (b) that the translational energy components of the initial GWP cover a broad range of energies which fits well to the energy range considered here. We note here that, this is the first theoretical work of its kind which considers to investigate this exchange reaction over such a wide range of energy. It can be seen from Fig. 3.1 (a) that the reaction onset in both the coupled and uncoupled state situation

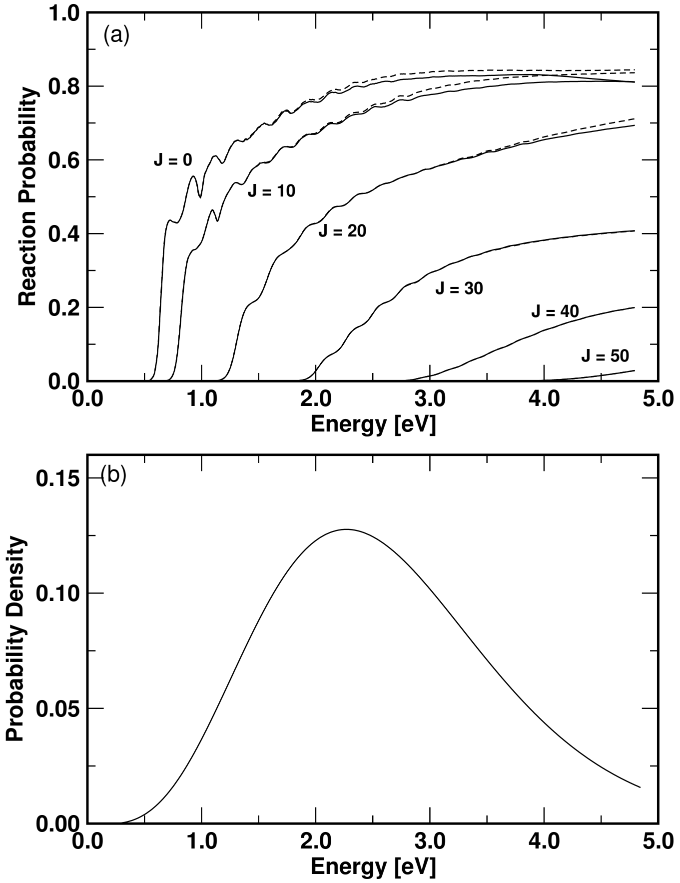

Figure 3.1: (a) Total reaction probabilities as a function of the total energy E (H, H_2 rovibrational) for the H + H_2 ($v = 0$, $j = 0$) $\rightarrow$ H_2 ($\sum v', \sum j'$) + H exchange reaction on the DBME PES for the total angular momentum, $J = 0$, 10, 20, 30, 40 and 50 (indicated in the panel). The coupled and uncoupled surface results are shown by the solid and dashed lines, respectively. The zero of the energy scale corresponds to infinitely separated reagent. (b) The energy distribution of the initial translational (H, H_2) GWP used for calculating the above reaction probabilities.

shifts to higher energies with an increase in the total angular momentum, J. The resonance structures and their energetic locations remain same for a given value of J in the coupled and uncoupled surface situations. The difference between the coupled and uncoupled surface reaction probabilities for a given value of J is nearly zero at low energies. At higher energies near and above the energetic minimum of the seam of CIs (at ~ 2.74 eV) this difference becomes noticeable (cf., Fig. 3.1 (a)). However, as J increases, the coupled and uncoupled surface results merge on each other, particularly for $J \geq 30$. The resonance structures seen in the reaction probability curves for low J values gradually disappear as J increases. Beyond $J = 40$ these resonances are not at all seen in the reaction probability curves.

The effect of rotational and vibrational excitation of the reagent H_2 on the coupled and uncoupled surface reaction probabilities of the H + H_2 reaction is shown in Figs. 3.2 (a - b), respectively. In Fig. 3.2 (a), the reaction probabilities of the reagent H_2 ($v = 0$, $j = 1$ - 3) for $J = 10$ and $\Omega = 0$ are plotted. Again, the coupled and uncoupled surface results are shown by the full and dashed lines, respectively. It can be seen from Fig. 3.2 (a) that the difference between the coupled and uncoupled surface results is small at low energies and this difference increases with increasing energies for a given value of j. In addition, with rotational excitation of reagent H_2, the difference between the coupled and uncoupled surface results increases and for $j = 3$, it becomes quite substantial already at energies much below the minimum of the seam of CIs. As the initial rotation of the reagent H_2 correlates with the internal rotation of the system around the CI, it is possible for the nuclear wavefunction to encircle the CI on the lower adiabatic sheet even if the upper one is not accessible at these energies. Therefore, the nonadiabatic effects seen in the reaction probability curve for $j = 3$ are likely

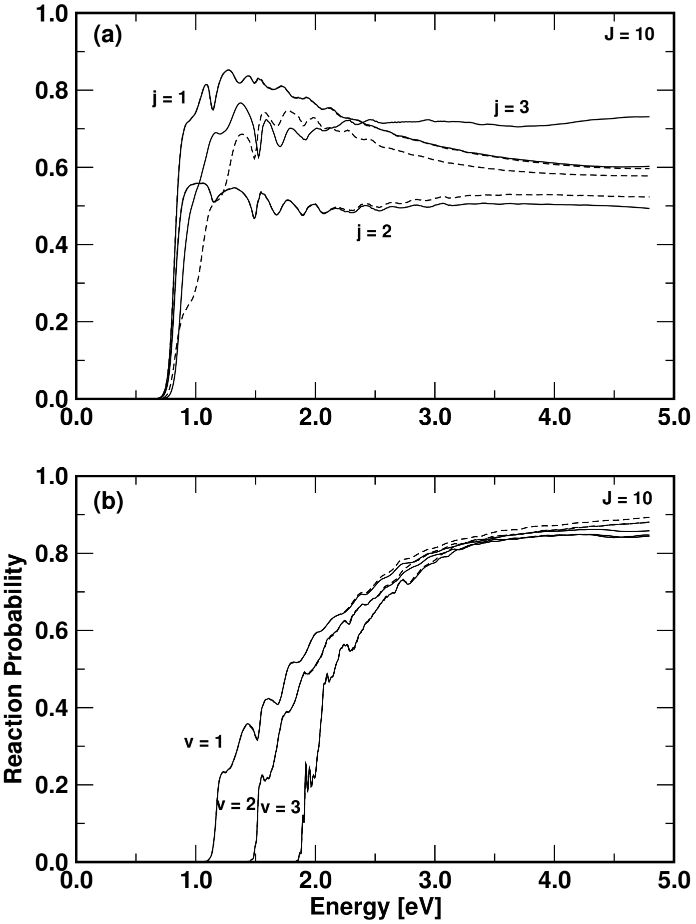

Figure 3.2: Same as in Fig. 3.1 (a) for (a) H + H_2 ($v = 0, j = 1 - 3$) → H_2 ($\sum v', \sum j'$) + H and (b) H + H_2 ($v = 1 - 3, j = 0$) → H_2 ($\sum v', \sum j'$) + H and for $J = 10$, $\Omega = 0$.

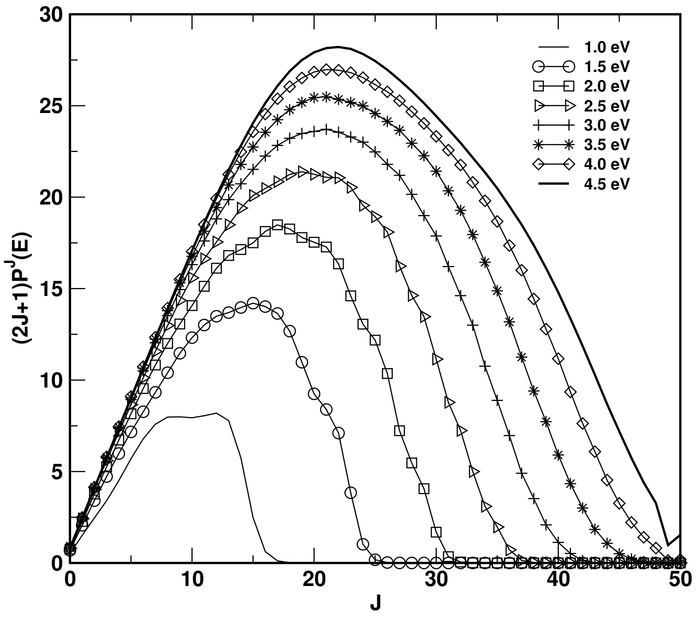

Figure 3.3: Weighted partial wave contribution to the integral reaction cross sections at various values of the total energy (indicated in the panel) for the H + H_2 $(v = 0, j = 0)$ reaction.

to arise from the geometric phase.

In Fig. 3.2 (b) we show the reaction probabilities of the reagent H_2 $(v = 1 - 3, j = 0)$ for $J = 10$ and $\Omega = 0$. The onset of the reaction shifts to higher energies with the vibrational excitation of the reagent H_2. The coupled and uncoupled surface results are shown in the panel by the full and the dashed lines, respectively. For a given value of v, the difference between the coupled and the uncoupled-surface results is small at low energies and it increases slightly with an increase in the energy. This slight difference is more visible beyond the energetic minimum of the seam of CIs. As the vibrational quantum number increases, the difference between the coupled and the uncoupled surface results also increases slightly. However, the effect of the nonadiabatic coupling on the reaction dynamics with reagent vibrational excitation appears not very significant.

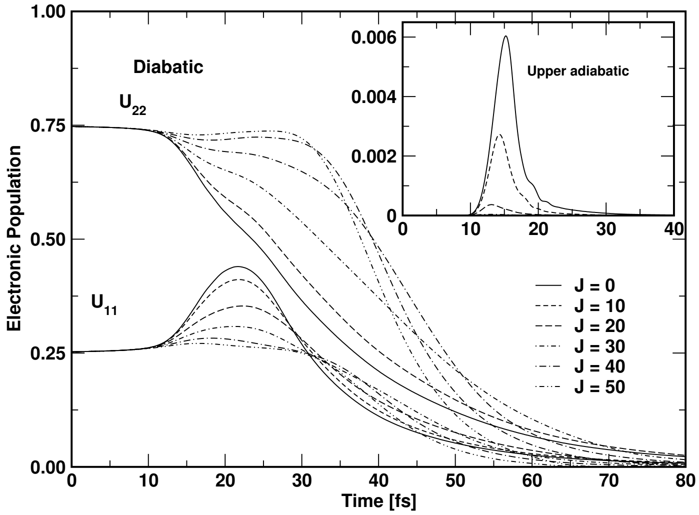

Figure 3.4: Electronic population dynamics for the H + H_2 $(v = 0, j = 0) \rightarrow H_2$ $(\sum v', \sum j')$ + H exchange reaction. The population of two component diabatic electronic states U_{11} and U_{22} for various values of the total angular momentum, J are shown by different line types (indicated in the panel). Because of the damping function activated at the grid edge, the above populations approach to zero at longer times. The maximum of the time-dependent population of the upper adiabatic electronic state (V_+) for different values of J are shown in the inset of the figure.

In Fig. 3.3, the J dependence of the degeneracy, $(2J{+}1)$ weighed reaction probability for the H + H_2 ($v = 0$, $j = 0$) reaction for eight representative values of the total energy (indicated in the panel) calculated from the probability results obtained in the coupled surface situation are shown. This analysis helps to assess the partial wave contributions to the integral reaction cross sections (discussed later in the text) for a given value of the total energy. The weighed probability value for a given energy initially increases with J due to the $(2J{+}1)$ degeneracy factor and then decreases at higher values of J, due to the shift of the reaction threshold caused by the centrifugal barrier. The partial wave contribution increases with increasing total energy, and J values upto 50 are necessary to include to obtain the converged reaction cross sections upto a total energy of $\sim$ 4.5 eV. The mild oscillations (mostly at low energy values) in the probability curves in Fig. 3.3 are associated with the resonances of the H + H_2 system. These oscillations disappear with an increase in the energy. In order to better understand the similarities between the coupled and uncoupled surface results we show in Fig. 3.4 the time evolution of the electronic populations in the coupled surface dynamics of H + H_2 ($v = 0$, $j = 0$) reaction for different values of J and $\Omega = 0$. The initial WP is prepared in the reagent asymptote of the lower adiabatic sheet of the DMBE PES. It is transformed to the diabatic electronic representation using the S matrix (cf., Eq. (2.7)) prior to the propagation. The two component diabatic populations for different values of J are shown by different line types indicated in Fig. 3.4. It can be seen from Fig. 3.4 that the population of the two component diabatic electronic states are $\sim$ 0.75 and $\sim$ 0.25 at t = 0. Therefore, we note that the asymptotic adiabatic potential also represents an admixture of the two diabatic potentials. However, as discussed in our earlier article [25], this does not introduce any numerical artifact in the dynamical attributes. At longer

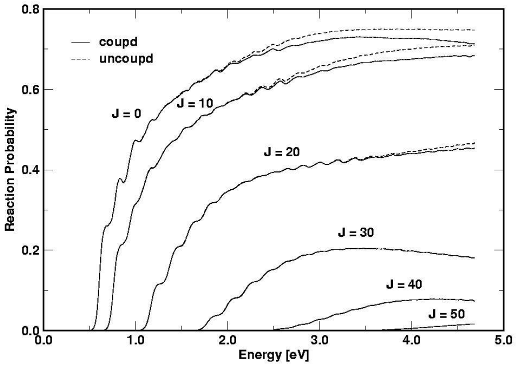

Figure 3.5: Same as in Fig. 3.1 for the H + D$_2$ ($v = 0, j = 0$) $\rightarrow$ HD ($\sum v', \sum j'$) + D exchange reaction on the DBME PES for the total angular momentum, J = 0, 10, 20, 30, 40 and 50 (indicated in the panel). The coupled and uncoupled surface results are shown by the solid and dashed lines, respectively. The zero of the energy scale corresponds to infinitely separated reagent.

times (> 50 fs) the populations of both diabatic sheets approached zero. This is because of the absorption of the wavepacket at grid edges by the damping function. The WP component reaching the upper adiabatic electronic state during the dynamics is shown in the inset of Fig. 3.4 for different values of J indicated in the figure. The population of this state reaches a maximum value of $\sim 6 \times 10^{-3}$ after ~ 15 fs for $J = 0$. But as J increases, the population of this state decreases. These maximum populations are $\sim 2.7 \times 10^{-3}$ and $\sim 3.8 \times 10^{-4}$ for $J = 10$ and 20, respectively. Beyond $J = 20$, the population of this state is found to be almost negligible.

We now discuss the above dynamical quantities calculated for the isotopic H + D$_2$, D + H$_2$ and H + HD reactions. The H + D$_2$ ($v = 0, j = 0$) $\rightarrow$ HD ($\sum v', \sum j'$) + D reaction probability values as a function of the total energy E are plotted in Fig. 3.5 for a few selected values of the total angular momentum, J = 0, 10, 20, 30, 40 and 50 (indicated in the panel) and for $\Omega = 0$. The coupled and uncoupled surface results are shown by the solid and dashed lines, respectively. We can see from Fig. 3.5 that the threshold for the reaction increases with increasing J to higher energy values. The difference between the coupled and uncoupled surface results is not seen below the minimum ($\sim$ 2.74 eV) of CIs. But above this minimum, the difference becomes noticeable. As J increases the difference between the coupled and uncoupled surface results becomes negligible. Above J = 20, the coupled and uncoupled results merge each other.

The D + H_2 $(v = 0, j = 0) \rightarrow$ HD $(\sum v', \sum j')$ + H reaction probability values as a function of the total energy E (D, H_2 translational + H_2 rovibrational) are plotted in Fig. 3.6 for a few selected values of the total angular momentum, J = 0, 10, 20, 30, 40 and 50 (indicated in the panel) and for $\Omega = 0$. The coupled and uncoupled surface results are shown by the solid and dashed lines, respectively. The coupled surface results here refer to those obtained by simulating the nuclear dynamics using the Hamiltonian of Eq. 2.2 and the uncoupled surface results are those obtained by simulating the nuclear dynamics on the uncoupled lower adiabatic sheet of the DMBE PES [59]. The reaction probabilities are calculated upto the three-body dissociation limit of the DH_2 system ($\sim$ 4.7 eV). As J increases, the reaction threshold increases to higher energy values due to an increase in the centrifugal barrier height with J. The resonance structures and their energetic locations remain same in both coupled and uncoupled surface results for a given value of J. The difference between the coupled and uncoupled surface reaction probabilities for a fixed value of J are nearly zero at low energies. At higher energies near and above the minimum of CIs, this difference becomes noticeable. With increase in J, this difference becomes insignificant.

We now discuss the above dynamical quantities calculated for the isotopic H

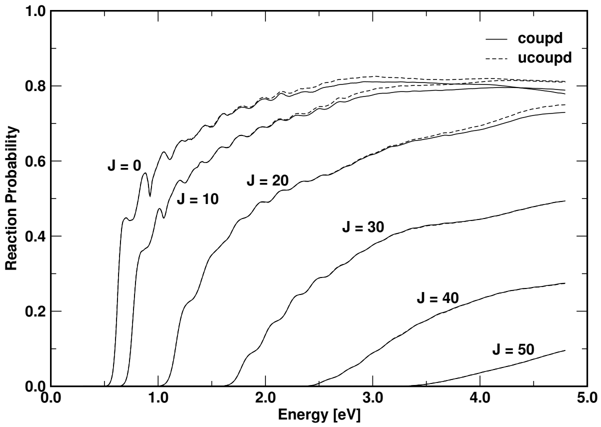

Figure 3.6: Same as in Fig. 3.1 for the D + H_2 ($v = 0, j = 0$) → HD ($\sum v', \sum j'$) + H exchange reaction on the DBME PES for the total angular momentum, J = 0, 10, 20, 30, 40 and 50 (indicated in the panel). The coupled and uncoupled surface results are shown by the solid and dashed lines, respectively. The zero of the energy scale corresponds to infinitely separated reagent.

+ HD reaction. This reaction yield either HD + H (channel R1) or H_2 + D (channel R2) products. Therefore, we in the following consider to show both the channel specific as well as total reaction probabilities. The reaction probability values for H + HD ($v = 0$, $j = 0$) reaction as a function of the total energy E are plotted in Figs. 3.5 (a-c) for five selected values of the total angular momentum, $J = 0$, 10, 20, 30 and 40 and for $\Omega = 0$. The reaction probabilities obtained in the uncoupled and coupled surface situations are shown by the dashed and solid lines, respectively. The reaction probabilities for channels R1 and R2 are given in panels (a) and (b), respectively, and the overall reaction probabilities (sum total of the two channel specific probabilities) are given in the panel (c). The effect of the nonadiabatic coupling on the channel specific reaction probabilities of panel (a) and (b) appears to be quite large for $J = 0$ and 10. These reveal a classic signature of nonadiabatic interactions including the geometric phase. Interestingly, the uncoupled and coupled surface results exhibit opposite behavior

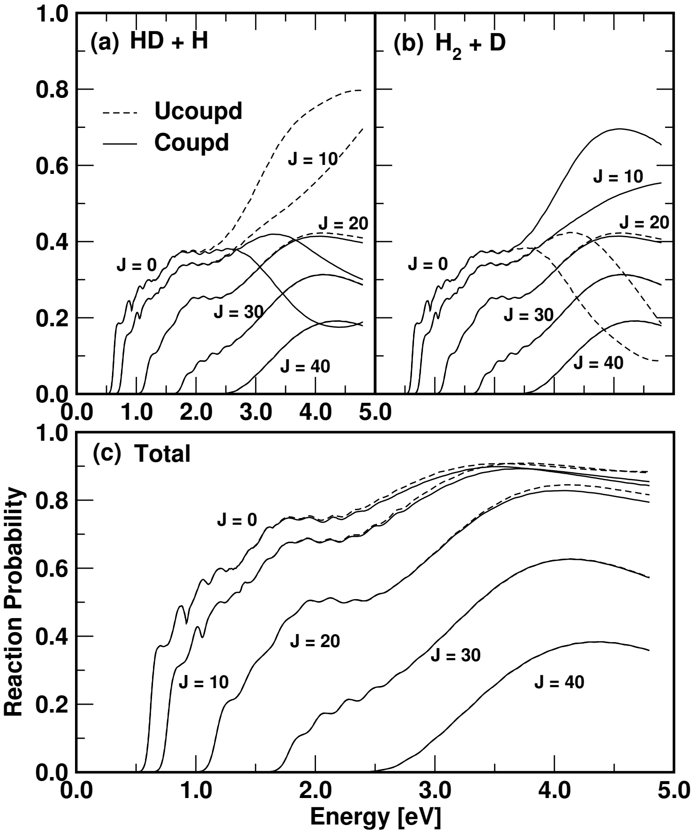

Figure 3.7: Reaction probabilities of the H + HD $(v = 0, j = 0)$ reaction for the (a)H + HD (R1) and (b)H_2 + D (R2) channels as a function of total energy, E. The sum total of these probabilities are plotted in panel (c). The probabilities are shown for various values of the total angular momentum, J indicated in each panel.

beyond the energetic minimum of the seam of CIs for $J = 0$ and 10 as shown in panels (a) and (b) for the R1 and R2 channels, respectively. And for $J = 20$ and beyond the differences between the uncoupled and coupled surface results are negligible. Due to this, the effect of the nonadiabatic interactions averages out in the total reaction probability results of panel (c) for small values of J. This may be because the inelastic probability (1 - total reaction probability) is not expected to show any geometric phase effects as it would require the nuclear wavefunction to traverse infeasible paths over three transition states. A verification of this will be worthwhile and will be addressed in a future publication [152]. For large J values, the channel specific reaction probabilities seem not to be affected by the nonadiabatic coupling and therefore, a similar trend is also observed in the total reaction probability results.

It emerges from the above discussion that the nonadiabatic coupling have almost similar effects in the dynamics of H + H_2 and its isotopic variants. At a more detailed level the channel specific reaction probabilities of the H + HD are seen to be severely affected by this coupling for low J values. A similar analysis to that depicted in Fig. 3.3 for the H + H_2 reaction revealed that the partial wave contributions upto $J = 60$ are necessary to obtain converged integral reaction cross sections for H + HD reaction upto the three-body dissociation limit.

3.2.3 Initial State-Selected Integral Reaction Cross Sections

The initial state-selected and energy resolved integral reaction cross sections, as a function of the total energy in the H + H_2 collisions are shown in Figs. 3.8 (a-d). These cross sections are calculated by Eq. (2.37). The coupled and uncoupled surface results are shown by the full and dashed lines, respectively, in each panel.

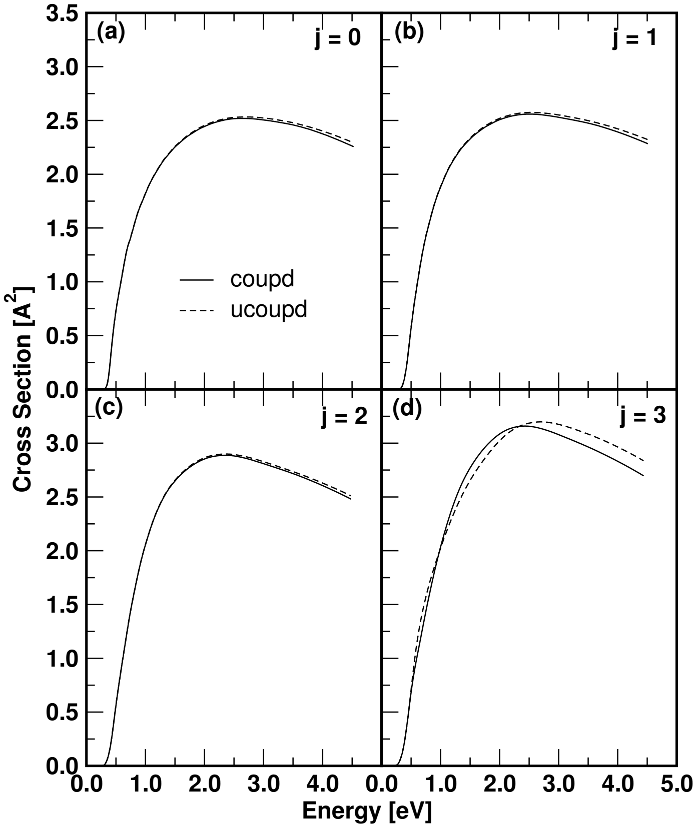

Figure 3.8: Initial state-selected integral reaction cross sections of the H + H_2 $(v = 0, j)$ as a function of the total energy. The cross sections for various j values are indicated in each panel.

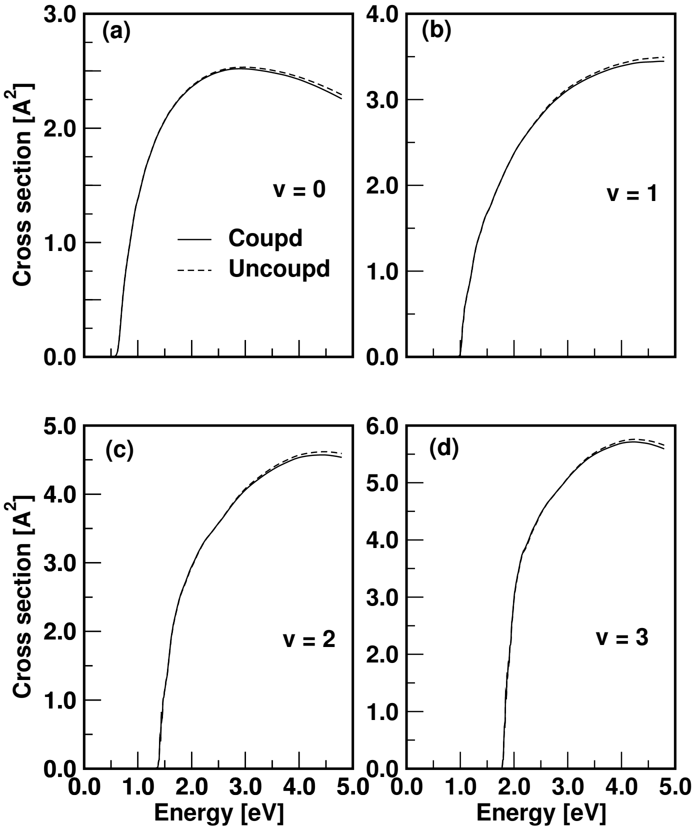

Figure 3.9: Same as in Fig. 3.8, for H + H_2 $(v, j = 0)$ reaction. The cross sections for various v values are indicated in each panel.

The reaction cross sections shown in Figs. 3.7 (a-d) for both the coupled and uncoupled surface situations are obtained with the rotationally excited reagent H_2 (j = 0 - 3, in panels (a) -(d), respectively) in the vibrational ground level (v = 0). The cross section results for $j > 0$ includes the contributions from $\Omega > 0$ and as stated above, Ω_{max} = min(j, J), within the CS approximation. For a given value of j the reaction cross section increases with energy reaching a maximum in the energy range of ~ 2.5 - 2.7 eV and then decreases as the energy increases in both the coupled and uncoupled surface results. The difference between the coupled and the uncoupled-surface results for a given value of j, is small at low

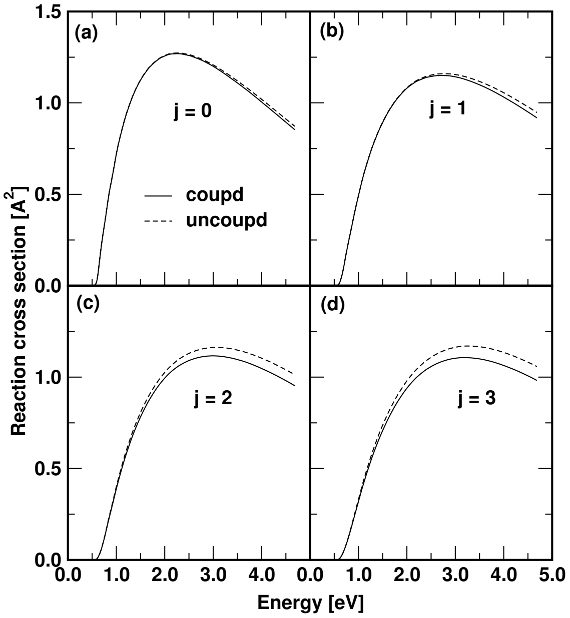

Figure 3.10: Same as in Fig. 3.8, for H + D_2 $(v = 0, j)$ reaction. The cross sections for various j values are indicated in each panel.

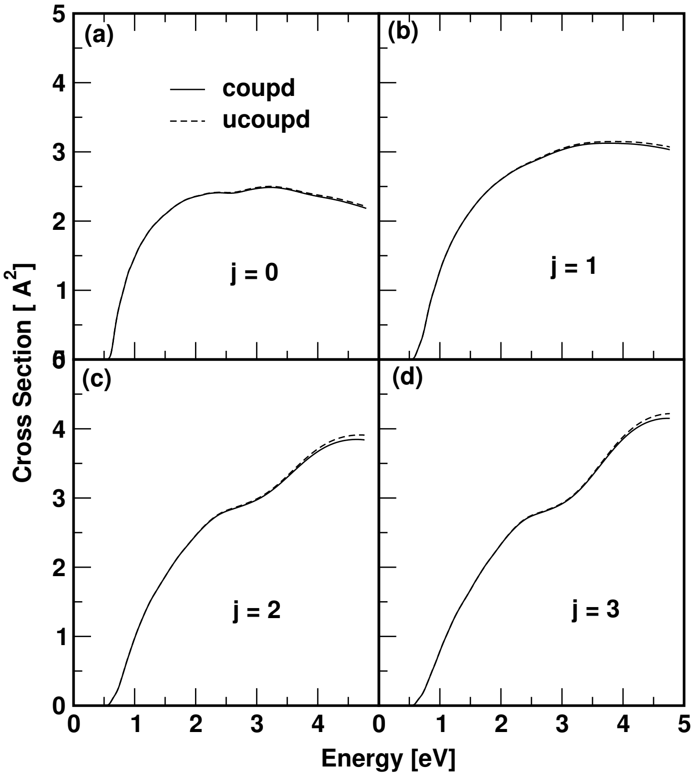

Figure 3.11: Same as in Fig. 3.8, for D + H_2 $(v = 0, j)$ reaction. The cross sections for various j values are indicated in each panel.

collision energies and increases very slightly for j = 0 - 2 beyond the energetic minimum of the seam of CIs. This difference appears to be somewhat larger for j = 3. The results of Fig. 3.8 do not reveal any dramatic effect of nonadiabatic coupling in the H + H_2 reaction dynamics on par with the recent GP results.

The integral reaction cross sections obtained with vibrationally excited H_2 are shown in Fig. 3.9 (a-d) for v = 0 - 3, respectively. In this case also no dramatic effect of the nonadiabatic coupling can be observed. The coupled surface results (solid lines) remain essentially identical to the uncoupled surface (dashed lines) results. The initial state-selected and energy resolved integral reaction cross sections of H + D_2 $(v = 0, j = 0 - 3)$ reaction are plotted as a function of the

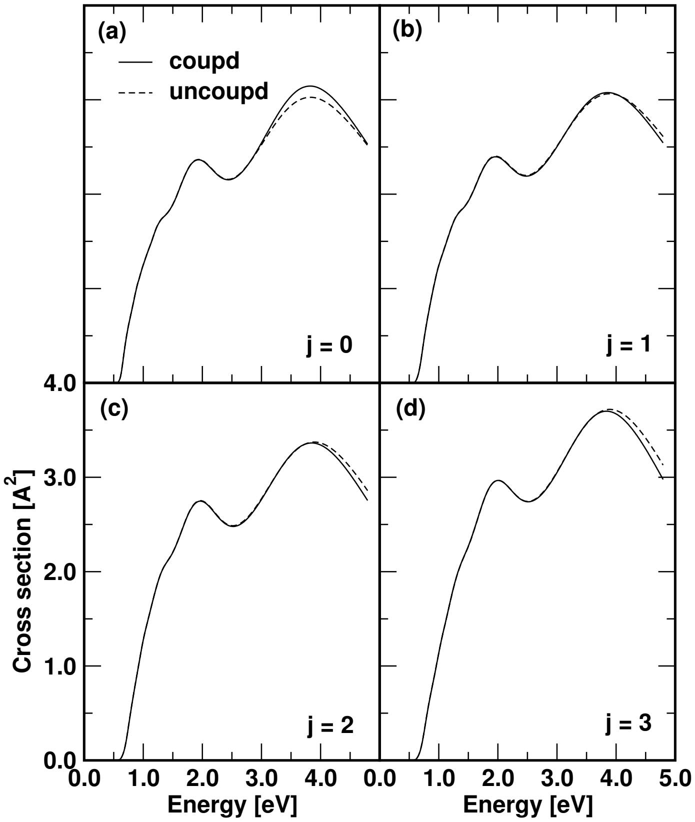

Figure 3.12: Same as in Fig. 3.8 for H + HD ($v = 0, j$) reaction. The cross sections here represent the sum total of those for the HD + H and H_2 + D channels shown for various j values indicated in each panel.

total energy and are shown in Figs. 3.10 (a - d). The coupled and uncoupled surface results are shown by the solid and dashed lines, respectively. It can be seen from the Figs. 3.10 (a - d) that for a particular value of j, the cross section values increases reaching a maximum in the energy range of 2.5 - 3.5 eV and then decreases, both in coupled and uncoupled surface situations. The difference between the coupled and uncoupled surface results is small at low energies and increases very slightly beyond the energetic minimum of the seam of CIs, occurring at $\sim$ 2.74 eV for a particular value of j. As j increases, the

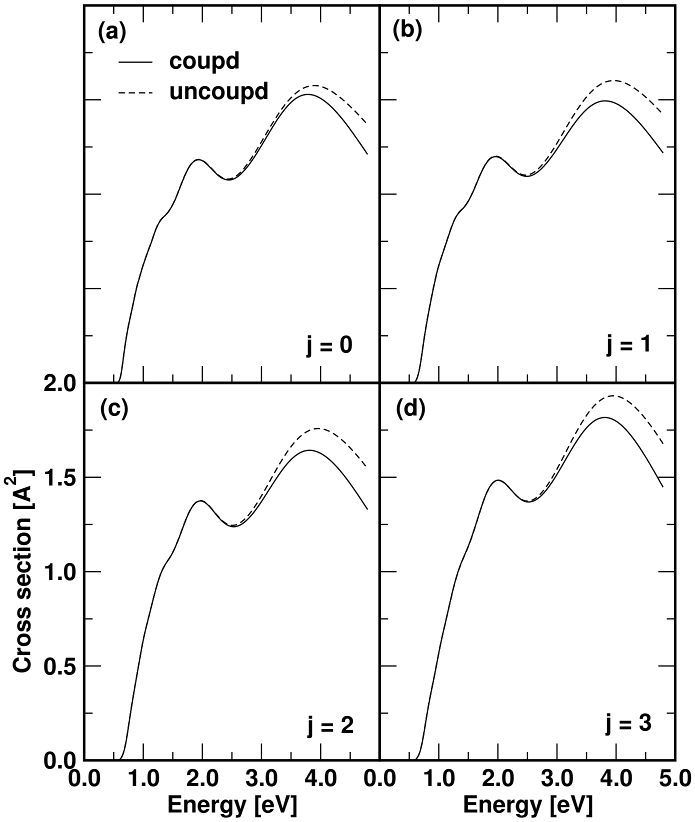

Figure 3.13: Same as in Fig. 3.8 for HD + H channel of H + HD $(v = 0, j)$ reaction.

difference between the coupled and uncoupled surface cross sections increases. The initial state-selected and energy resolved integral reaction cross sections of D + H_2 $(v = 0, j = 0-3)$ reaction are plotted as a function of the total energy and are shown in Figs. 3.11 (a - d). The coupled and uncoupled surface results are shown by the solid and dashed lines, respectively. It can be seen from the Figs. 3.11 (a - d) that the cross section increases with energy reaching a maximum value in the energy range 2.5 - 3.5 eV and then decreases for a particular value of j. The difference between the coupled and uncoupled surface results is small at low energies and increases very slightly beyond the energetic minimum of the

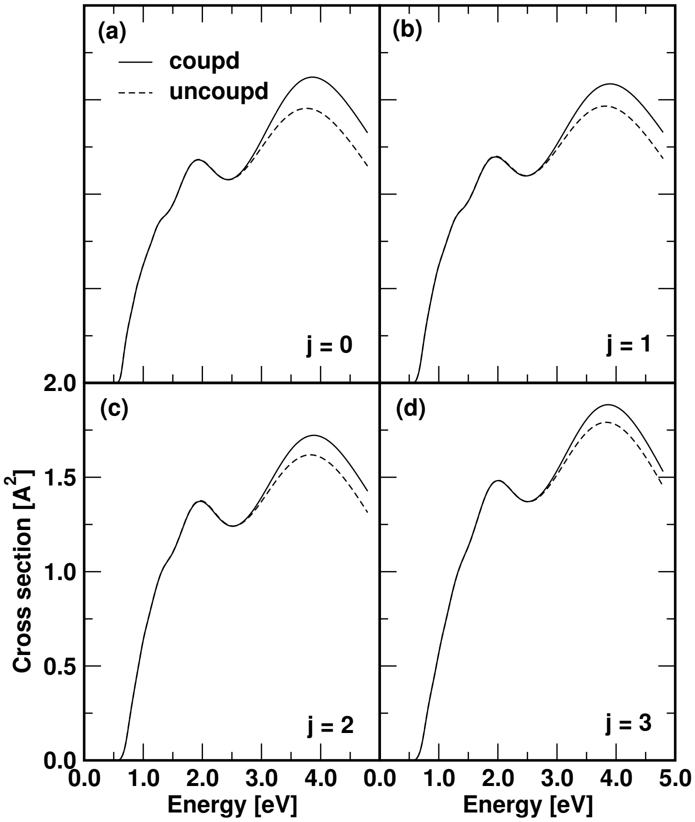

Figure 3.14: Same as in Fig. 3.8 for H_2 + D channel of H + HD ($v = 0, j$) reaction.

seam of CIs, occurring at $\sim$ 2.74 eV for a particular value of j. As j increases, the cross section values are seen to increase with energy in both coupled and uncoupled surface cross sections.

The initial state-selected total integral reaction cross sections for the H + HD (v = 0, j = 0 - 3) reaction are plotted in Figs. 3.12 (a-d) as a function of total energy. Unlike H + H_2 reaction cross sections (cf., Figs. 3.8 (a - d)) the H + HD reaction cross sections reveal resonance structures. The difference between the uncoupled (dashed lines) and coupled (solid lines) surface results in this case is somewhat larger when compared to the H + H_2 (cf., Figs. 3.8 (a - d)) results. The trend observed in the channel specific reaction probability results (cf., Figs. 4 (a-c)) also show up in the channel specific reaction cross sections. The channel specific reaction cross sections are shown for H + HD ($v = 0$, $j = 0$ - 3) reaction in Figs. 3.13 (a - d) and 3.14 (a - d) for the R1 and R2 channels, respectively, for illustration. However, in the total reaction cross section (sum total of R1 and R2 channels) the two opposite trends cancel out and therefore the coupled and uncoupled surface results essentially becomes identical. The reaction cross sections obtained with the vibrationally excited HD molecule in the ground rotational level also reveal similar characteristics and are not shown here.

3.2.4 Thermal Rate Constants

The thermal rate constants obtained by statistically averaging over the rotational states $j = 0$ - 3 are shown in Fig. 3.15 for the H + H_2 ($v = 0$) reaction. The coupled and uncoupled surface results are shown by the full and dashed lines, respectively.

The rate constants values available in the literature are shown by different points on the diagram. The meaning of various points are also indicated in the panel. The unfilled diamonds represents the experimental points extracted from Table IX of Pack *et al* [155]. With quite minor deviations all results of Fig. 3.15 are consistent with each other. The minor deviations represent estimates of the accuracy of the PES and the theoretical methods. The present rate constants reveal the expected Arrhenius behavior. Now most importantly Fig. 3.15 reveals that the difference between the coupled and uncoupled surface results is insignificant (within the drawing accuracy) in the reported temperature range of $\sim$ 0 - 1500 K.

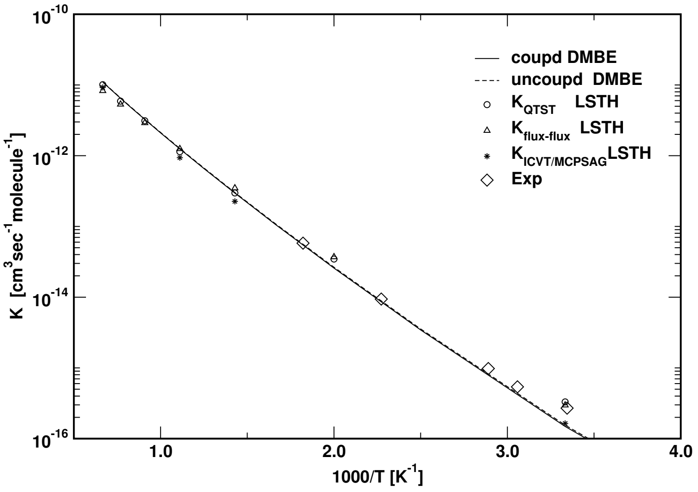

Figure 3.15: Arrhenius plot of the Boltzmann averaged (over j = 0 - 3) thermal rate constants for the H + H_2 (v = 0) reaction. The coupled and uncoupled surface results are shown by solid and dashed lines, respectively. Points on the diagram represents the results from the literature (K_{QTST} LSTH from Ref. [154]; $K_{flux-flux}$ LSTH from Ref. [155]; $K_{ICVT/MCPSAG}$ LSTH from Ref. [156]. The experimental values are taken from the Table IX of Ref. [154]).

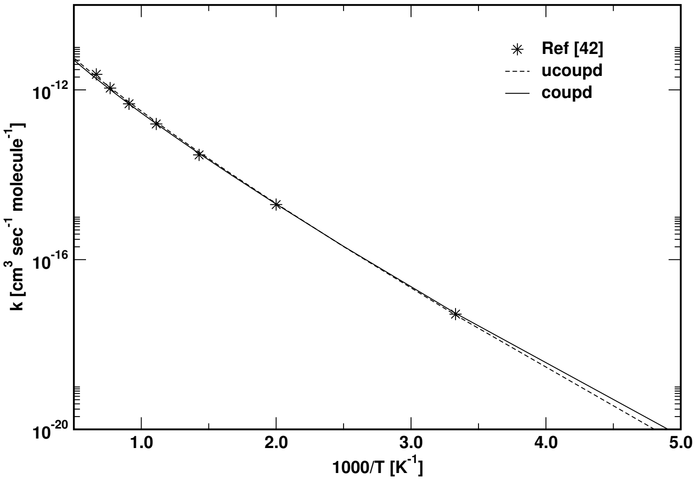

Figure 3.16: Same as in Fig. 3.15 for H + D_2 (v = 0) reaction. The points on the diagram refer to the results from the Ref. [157].

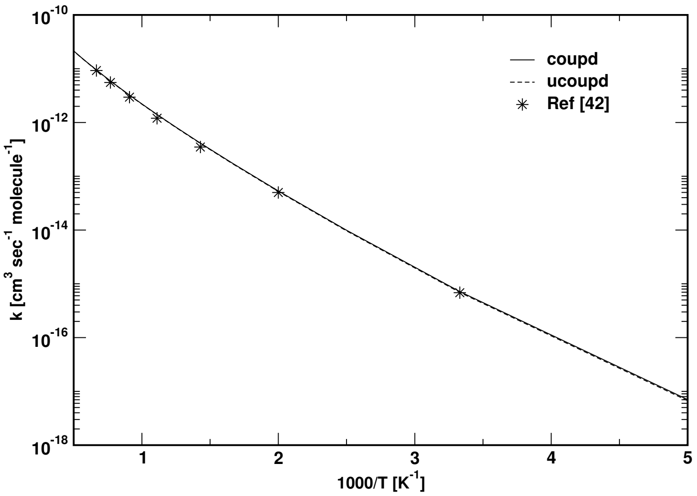

Figure 3.17: Same as in Fig. 3.15 for D + H_2 (v = 0) reaction. The points on the diagram refer to the results from the Ref. [158].

Similarly, we also show the thermal rate constants for the H + D_2 (v = 0) reaction by statistically averaging over the rotational states j = 0, in Fig. 3.16. The coupled and uncoupled surface results are shown by full and dashed lines, respectively. The rate constants values available in the literature are shown and indicated in the figure.

The thermal rate constants obtained for the D + H_2 (v = 0) by statistically averaging over the rotational states j = 0 - 3 are shown in Fig. 3.17. The coupled and uncoupled surface results are shown by the solid and dashed lines, respectively. The rate constant values available in the literature are shown and indicated in the diagram. The meaning of various points are also indicated in the figure. The rate constants reveal the expected Arrhenius behavior. It can also be seen from the Fig. 3.17 that the difference between the coupled and uncoupled results are insignificant in the reported range of ∼ 0 - 1500 K.

In Figs. 3.18 (a-b), we show the thermal rate constants obtained by statistically averaging over the rotational states j = 0 - 3 for the R1 and R2 channels

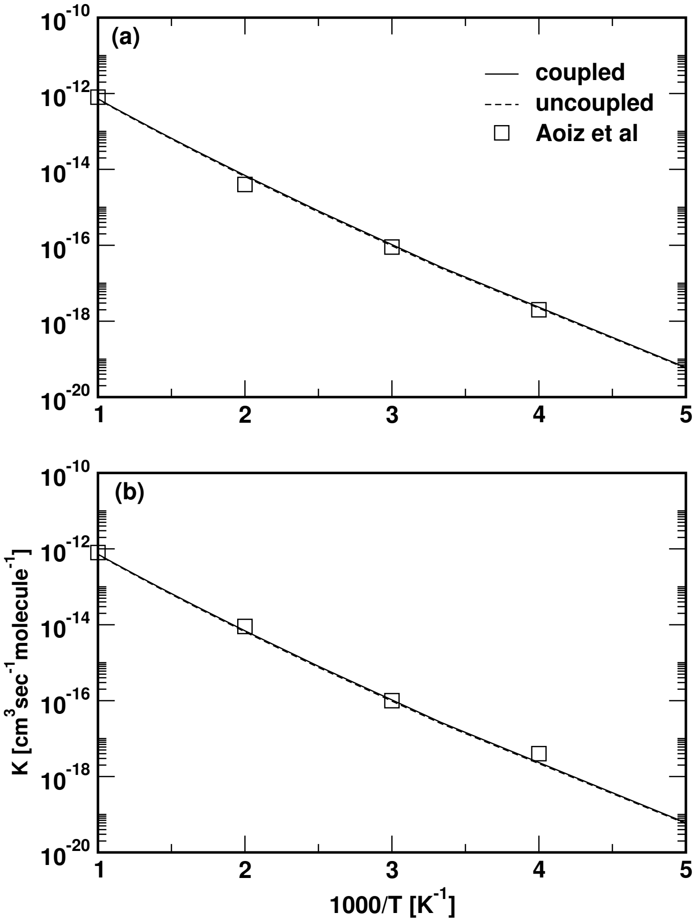

Figure 3.18: Same as in Fig. 3.15 for H + HD ($v = 0$) reaction. Thermal rate constants for the HD + H and H_2 + D channels are shown in panel (a) and (b), respectively. The points on the diagram refer to the results from the Ref. [159].

of the H + HD reaction, respectively. The coupled and uncoupled state results are shown by the full and dashed lines, respectively. The difference between the coupled and uncoupled surface results is also insignificant in these cases, although the channel specific reaction cross sections reveal some variations (cf., Figs. 3.13 (a - d) and 3.14 (a - d)). The difference apparently averages out on integrating the cross sections over the energy, to calculate the thermal rate constants. The theoretical results of Aoiz and coworkers extracted from [159] are superimposed on Figs. 3.18 (a-b) and are shown as squares. We see that our rate constant values are in good agreement with those of Aoiz and coworkers [159]. In Fig. 3.19 the total (sum of two channels) thermal rate constants obtained by statistically averaging over the reagent rotational states $j = 0$ - 3 are shown. Again, the coupled and uncoupled surface results shown by the full and dashed lines, respectively, reveal hardly any difference. We can see from the figure that the difference between the coupled and uncoupled surface results is small in the temperature range considered.

This drives us to the final point of concluding that the important dynamical observable like the thermal rate constant derived from the microscopic reaction probabilities is insensitive to the nonadiabatic coupling in the H + H_2 reaction dynamics. Even though, the latter show some effects of coupling in their detailed variations over the considered energy range.

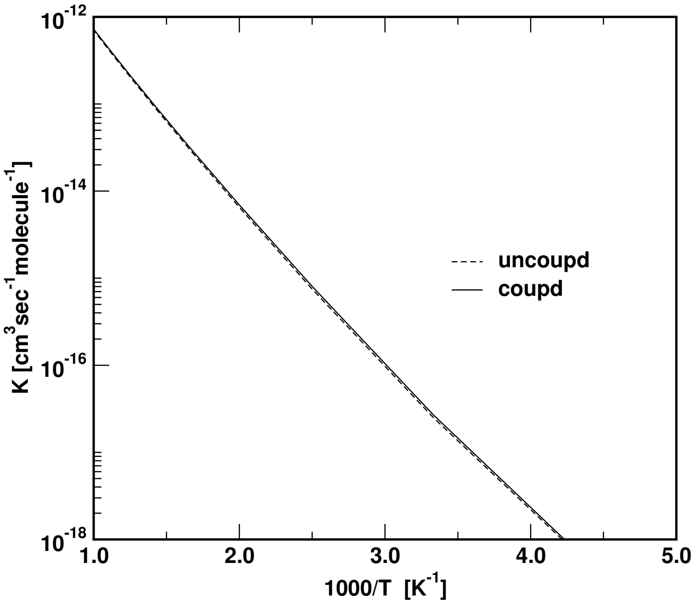

Figure 3.19: Same as in Fig. 3.15, for the total H + HD reaction.

3.3 Effect of reagent rotation and vibration on the H + H_2 reaction

3.3.1 Reaction probability

The H + H_2 ($v = 0, j = 4$) reaction probability values as a function of the total energy E (H, H_2 translational + H_2 rovibrational) are plotted in Fig. 3.20 for a few selected values of the total angular momentum $J = 0$, $\Omega = 0$ and $J = 4$, 10, 20, 30, 40 and 50 (indicated in the panel) and for $\Omega = 4$. The coupled and uncoupled surface results are shown by the solid and dashed lines, respectively. The zero of the energy scale corresponds to asymptotically separated reagents. It can be seen from Fig. 3.20, that coupled and uncoupled surface results dramatically differ from each other. The reaction threshold in both coupled and uncoupled surface situations shifts to higher energy as J increases.

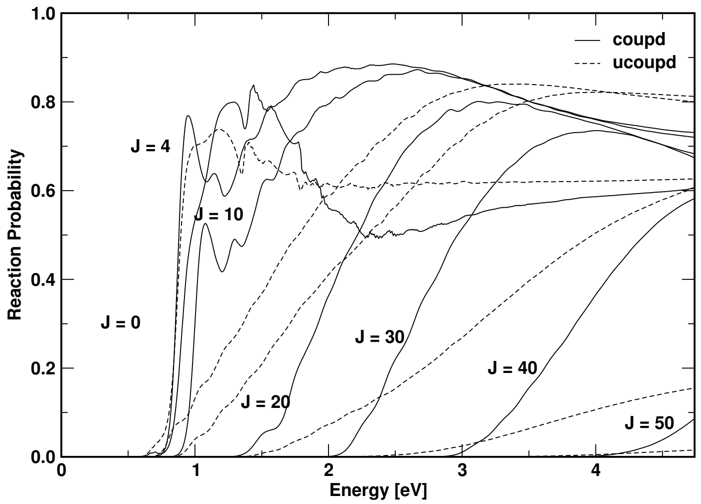

Figure 3.20: Total reaction probabilities as a function of the total energy E (H, H$_2$ rovibrational) for the H + H$_2$ ($v = 0$, $j = 4$) → H$_2$ ($\sum v', \sum j'$) + H exchange reaction on the DBME PES for the total angular momentum $J = 0$, $\Omega = 0$ and $J = 4$, 10, 20, 30, 40 and 50 (indicated in the panel) for $\Omega = 4$. The coupled and uncoupled surface results are shown by the solid and dashed lines, respectively. The zero of the energy scale corresponds to infinitely separated reagent.

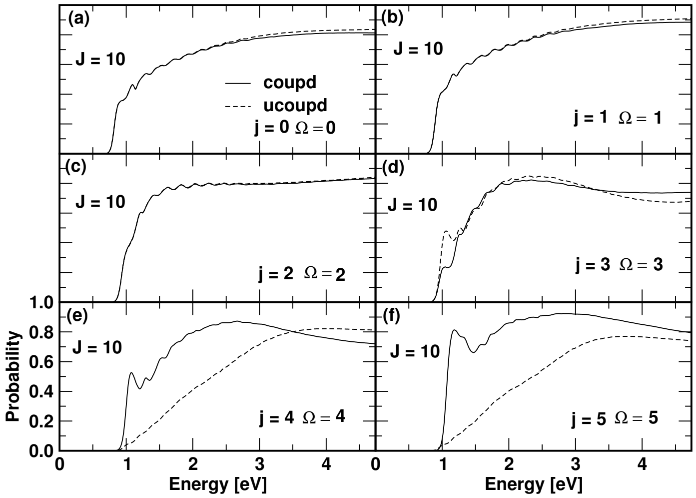

Figure 3.21: Same as in Fig. 3.20, for the H + H$_2$ (v = 0, j = 0 - 5, Ω = 0 - 5) reaction for the total angular momentum, J = 10. The coupled and uncoupled surface results are shown by the solid and dashed lines, respectively.

The difference between the coupled and uncoupled surface results increases with increase in J, and the reactivity increases in the coupled surface situation. It can also be seen from the figure that the uncoupled surface reaction probability for J = 50 is almost zero. The resonance structures are absent in the uncoupled surface results for small values of J.

In Figs. 3.21 (a - f) H + H$_2$ ($v = 0, j = 0-5, \Omega = 0-5$) reaction probabilities are shown for the total angular momentum, J = 10. The coupled and uncoupled surface results are again shown by solid and dashed lines, respectively. It can be seen from Figs. 3.21 (a - f) that the difference between the coupled and uncoupled surface reaction probabilities is insignificant for j = 0 - 2 and becomes substantial for $j \geq 3$. This shows that the nonadiabatic effects can become quite substantial with rotational excitation of reagent, H$_2$.

The H + H$_2$ ($v = 4, j = 0$) reaction probability values as a function of the total energy E are plotted in Fig. 3.22 for a few selected values of J = 0, 10,

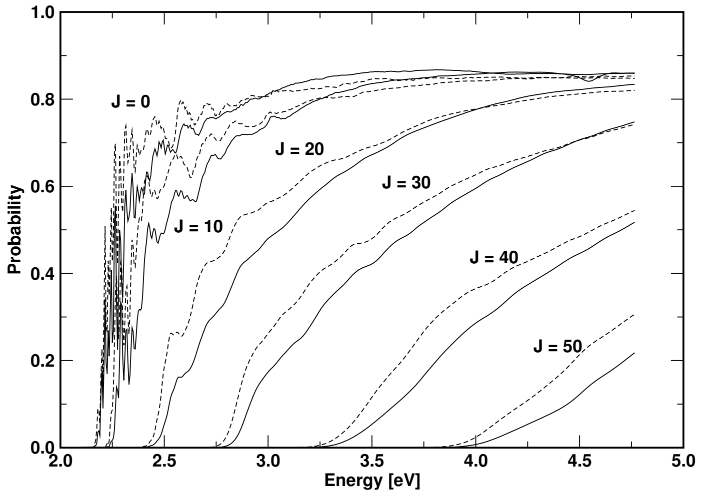

Figure 3.22: Same as in Fig. 3.20, for the H + H_2 ($v = 4, j = 0$) $\rightarrow$ H_2 ($\sum v', \sum j'$) + H reaction for the total angular momentum, J = 0, 10, 20, 30, 40 and 50 (indicated in the panel) and $\Omega = 0$.

20, 30, 40 and 50 (indicated in the panel) and for $\Omega = 0$. The coupled and uncoupled surface reaction probabilities are shown by solid and dashed lines, respectively. It can be seen from the Fig. 3.22 that the difference between the coupled and uncoupled surface reaction probabilities is low at small values of J and this difference increases with J.

When compared with Figs. 3.20 and 3.21 (a-f) it can be seen that electronic nonadiabatic interactions have more pronounced effect in the reaction dynamics with rotationally excited reagent. It can also be seen from the Fig. 3.22 that the resonance structures survive for smaller values of J and they are not seen beyond $J = 30$.

The effect of reagent, H_2 rotational excitation on the coupled and uncoupled surface reaction probabilities of the H + H_2 ($v = 0, j = 0 - 10$) reaction is shown in Figs. 3.23 (a - k) for $J = 0$ and $\Omega = 0$. The coupled and uncoupled surface results are shown by solid and dashed line types, respectively. It can be seen from the figure that the difference between the coupled and uncoupled surface reaction probabilities is small at smaller values of j and it increases with increasing j values. This difference is quite substantial already at energies below the minimum of the seam of CIs occurring at ~ 2.74 eV for $j \geq 3$. As j increases, the initial rotation of the reagent can correlate with the internal rotation of the system around the CI, and it becomes feasible for the nuclear wavefunction to encircle the CI on the lower adiabatic sheet even if the upper adiabatic sheet is not accessible at these energies. Therefore, the electronic nonadiabatic effects can become substantial with an increase in the reagent rotation.

The effect of reagent, H_2 vibrational excitation on the coupled and uncoupled surface reaction probabilities of the H + H_2 ($v = 0-10, j = 0$) reaction is shown in Figs. 3.24 (a - k) for $J = 0$ and $\Omega = 0$. The onset of the reaction shifts to the higher energies with the vibrational excitation in both the coupled and uncoupled surface situations. The resonance oscillations increase with the vibrational excitation for v = 0 - 10. The difference between the coupled and uncoupled surface reaction probabilities increases only slightly with the vibrational excitation. The effect is far lower in magnitude when compared with similar rotational excitation (cf., Figs. 3.23 (a-k)). The difference between the coupled and uncoupled surface results in Figs. 3.24 (a-k) is more visible only above the minimum of CIs. This shows that the effect of nonadiabatic coupling on the reaction dynamics with vibrationally excited reagent is not very significant.

3.3.2 Initial state-selected integral reaction cross sections

Initial state-selected and energy resolved integral reaction cross sections, as a function of the total energy in the H + H_2 collisions are shown in Figs. 3.25 (a - k). The coupled and uncoupled surface results are shown by solid and dashed line

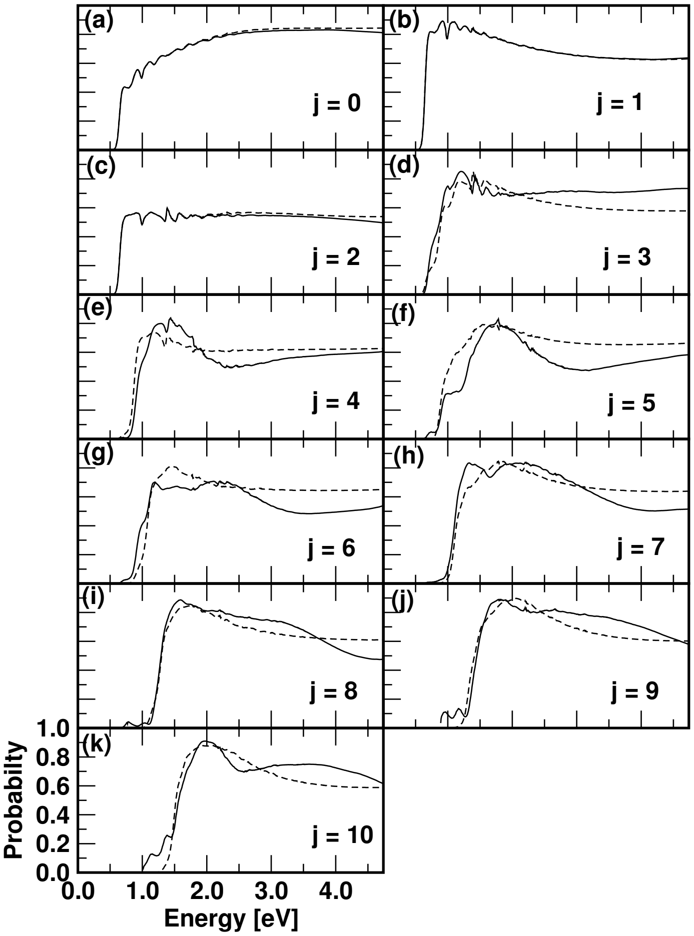

Figure 3.23: Same as in Fig. 3.20, for H + H_2 (v = 0, j = 0 - 10) → H_2 ($\sum v', \sum j'$) + H reaction on the DBME PES for the total angular momentum, $J = 0$ and $\Omega = 0$.

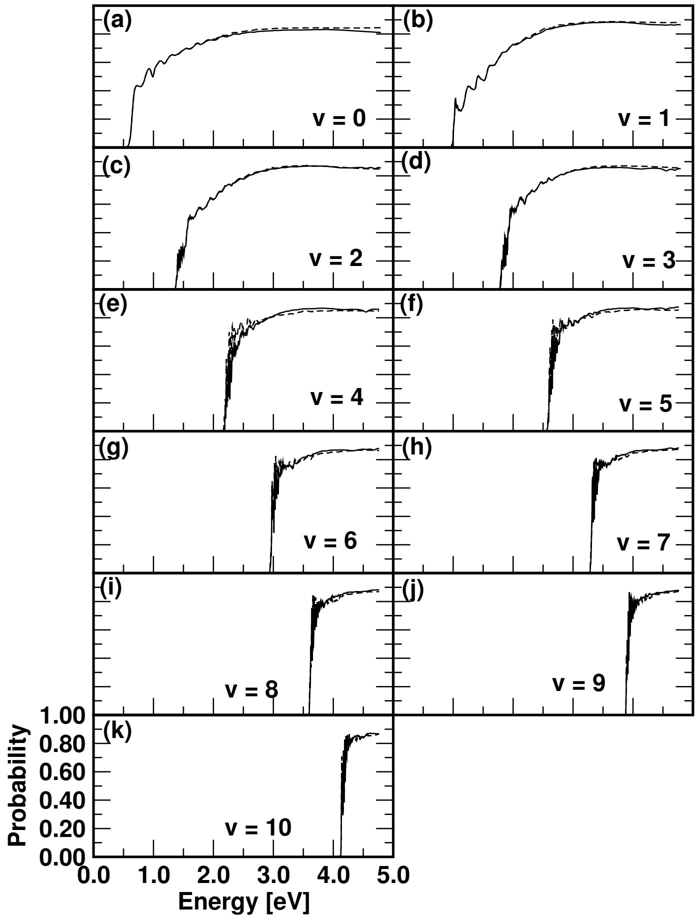

Figure 3.24: Same as in Fig. 3.20 for the H + H$_2$ (v = 0 - 10, j = 0) → H$_2$ ($\sum v', \sum j'$) + H reaction for the total angular momentum, $J = 0$ and $\Omega = 0$.

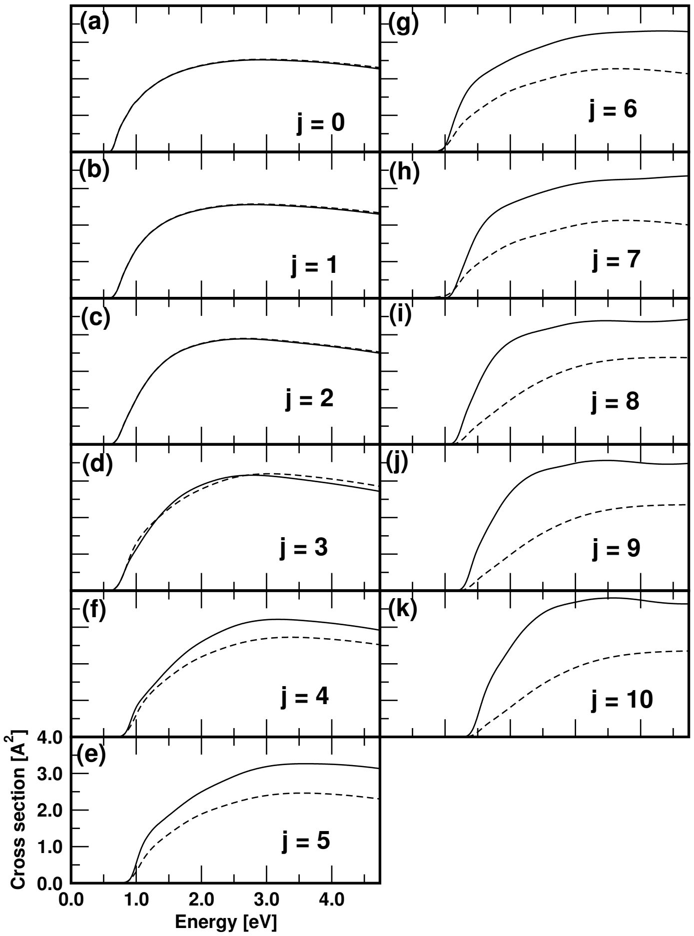

Figure 3.25: Initial state-selected integral reaction cross sections of the H + H$_2$ ($v = 0, j$) as a function of the total energy. The cross sections for various j values are indicated in each panel. The coupled and uncoupled surface results are shown by the solid and dashed lines, respectively.

types, respectively, in each panel. These reaction cross sections shown in Figs. 3.25 (a - k) for both coupled and uncoupled surface situations are obtained with the reagent, H_2 is in its ground vibrational level and $j = 0$ - 10 levels (indicated in the respective panel). The cross section for $j > 0$ includes the contributions from $\Omega > 0$ and $\Omega_{max} = \min(j, J)$, within the CS approximation. For a given value of j the reaction cross section increases with energy reaching a maximum in the energy range $\sim$ 2.5 - 2.7 eV and then decreases as the energy increases in both coupled and uncoupled surface situation. The difference between the coupled and uncoupled surface results for a given value of j, is small at low collision energies and increases very slightly for $j = 0$ - 3, at energies beyond the minimum of the seam of CIs ($\sim$ 2.74 eV). This difference becomes quite pronounced beyond $j \geq$ 3.

The integral reaction cross sections obtained with vibrationally excited H_2 are shown in Fig. 3.26 for $v = 0$ - 10, in panels (a - k), respectively and for j = 0. In contrast to the rotational excitation, reactivity upon reagent vibrational excitation is not dramatically affected by the nonadiabtatic coupling. It can be seen from Fig. 3.26 that the difference between the coupled and uncoupled surface results is negligibly small. The resonance structures of the probability results average out with many partial wave contribution in the cross section results of Figs. 3.25 and 3.26.

3.4 Coriolis coupling effects

In this section, we present and discuss the effect of CC on the initial state-selected reaction probabilities of H + H_2 reaction and compare them with the same using the CS approximation. The CC reaction probabilities are reported for

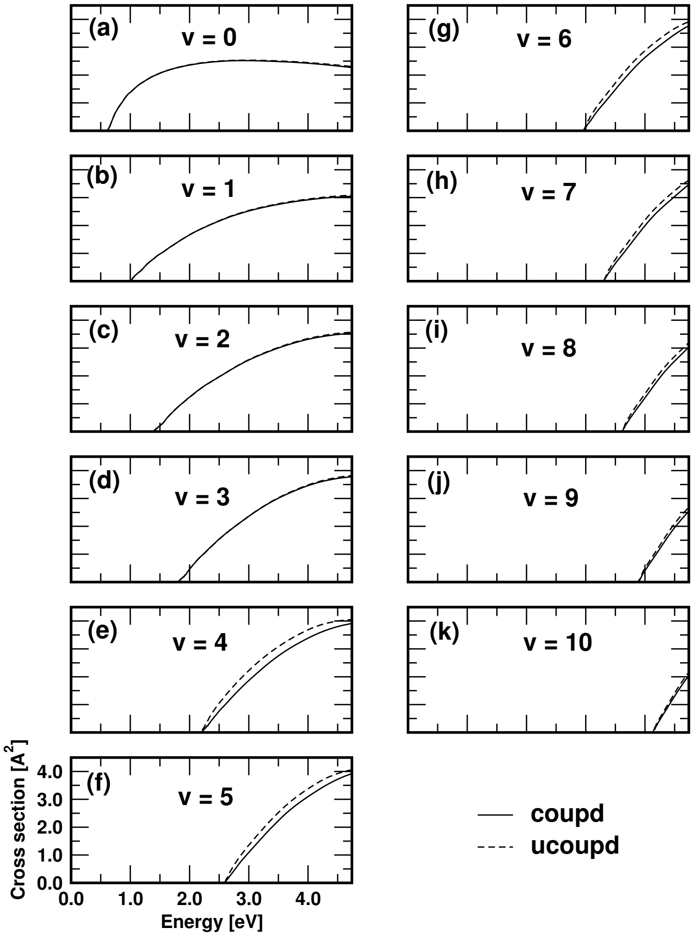

Figure 3.26: Same as in Fig. 3.25, for H + H_2 $(v, j = 0)$ reaction. The cross sections for various v values are indicated in each panel.

a total energy of $\sim$ 3.0 eV. Exact quantum scattering calculations were obtained by a WP propagation method based on the CP expansion scheme and DMBE PES of the reacting system. Partial wave contributions up to the total angular momentum J = 20 were found to be necessary for the scattering of H_2 in its ground rotational and vibrational states up to a total energy of 3.0 eV. For each J value, the projection quantum number K was varied from 0 to min (J,K_{max}), with $K_{max} = 4$. We present only the preliminary results here. The work including higher values of K is presently under progress .

3.4.1 Computational Details

The properties of the initial WP and the grid parameters used for the numerical calculations are listed in Table I. The WP is propagated for a total time of 413.76 fs using the CP scheme. It is well known that the stability of the CP scheme depends on the maximum allowed energy on the grid. For the potential energy, one generally sets a cut-off value to control the stability. The angular kinetic energy on the grid depending on the j_{max} $(= N_\gamma$ - 1) and J is usually large. Very large values of this kinetic energy are unphysical and the relevant wavefunction does not contain any components corresponding to them. In the present application the maximum permitted value of the angular kinetic energy is therefore truncated gradually above a reasonable value [160]. All calculations reported in this section are carried out with H_2 in its vibrational and rotational ground state. Each WP propagation upto 413.76 fs on a single processor takes nearly 60 hours of CPU time in an IBM P690 machine for the uncoupled situation. This CPU time increases considerably in case of coupled situation. The maximum allowed value of K (K_{max}) is considered upto 4, in the present case. The calculations considering higher values of K are still ongoing and we present only the preliminary results here. The parity is included in the dynamical calculations, which is decided by the (-1)$^{J+p}$ value. The convergence of the CC reaction probability results upto the total energy $E \sim 3.0$ eV and for each J and K values is explicitly checked with respect to the numerical parameters given in Table 3.1.

3.4.2 Reaction Probabilities

The initial state-selected and energy resolved reaction probability as a function of the total energy E for uncoupled situation are plotted in Figs. 3.27 (a - b) for the total angular momentum, $J = 1$ and $K = 0$, in panel (a) and $K = 1$, in panel (b), respectively. We also show the corresponding results with the CS approximation for comparison in each panel. The full lines represents the CC results and dashed lines represents CS results, respectively.

The CS calculations are carried out for a fixed value of the K quantum number, whereas in the CC calculations K is a variable quantity and is allowed to vary between 0 to min (J, K_{max}). We can see from the Figs. 3.27 (a - b) that both CC and CS reaction probabilities show the same number of resonances. The location of these resonances differ in both the cases which can be seen from Figs. 3.27 (a - b). The initial state-selected CC reaction probabilities calculated in both coupled and uncoupled surface situations are shown in Figs. 3.28 (a - b). The coupled surface results are shown by the full line type and the uncoupled surface results are shown by a dashed line type for clarity in the Figs. 3.28 (a - b). It can be seen from the Figs. 3.28 (a - b) that the coupled and uncoupled surface results differ above the minimum of the CIs, i.e., above 2.74 eV.

The initial state-selected CC reaction probabilities calculated in both coupled and uncoupled surface situations for $J = 5$ and $K = 0$ to 4 are shown in Figs. 3.29 (a - e) panels. The coupled and uncoupled surface results are shown by full

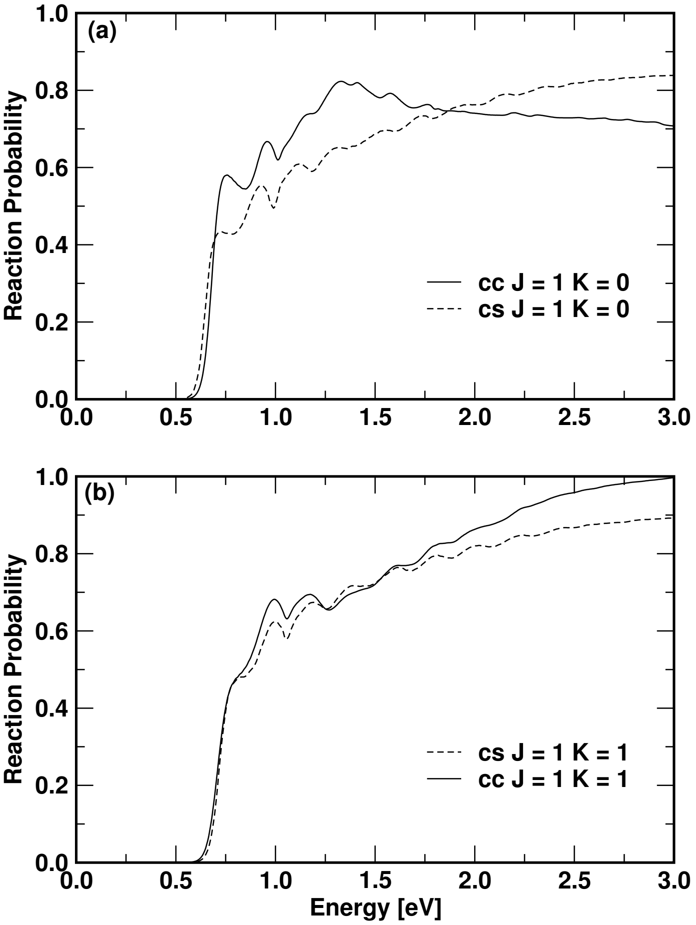

Figure 3.27: H + H_2 ($v = 0, j = 0$) reaction probabilities as a function of the total energy (H - H_2 translational energy + H_2 rovibrational energy) for the total angular momentum $J = 1$, $K = 0$, in panel (a) and $J = 1$, $K = 1$, in panel (b) calculated using the CC and CS models, respectively. The different line types are identified in the panels.

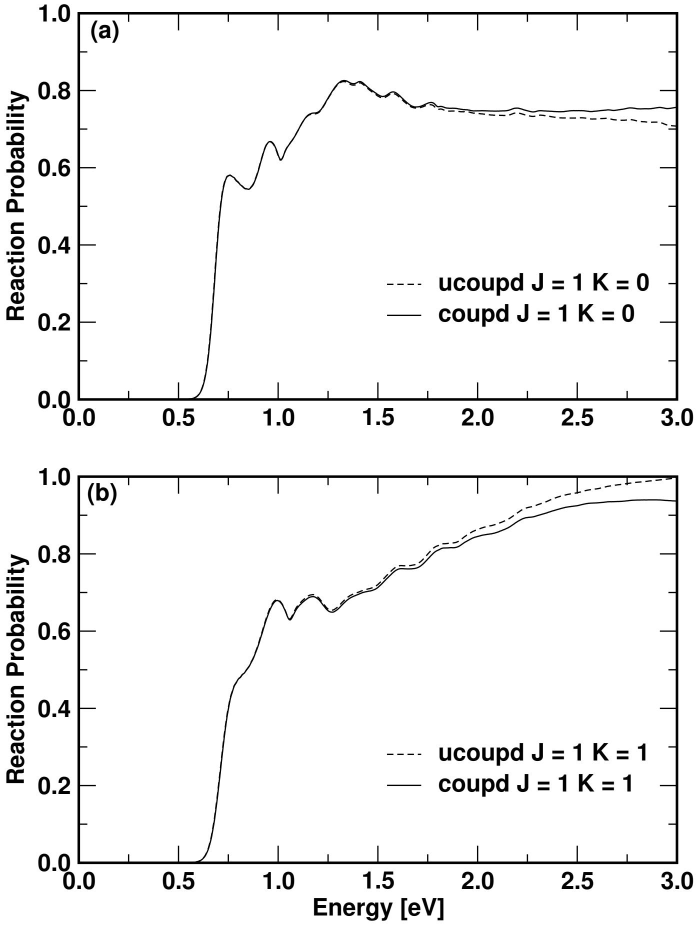

Figure 3.28: Total reaction probabilities as a function of total energy E for the H + H_2 $(v = 0, j = 0)$ exchange reaction for the total angular momentum $J = 1$, $K = 0$, in panel (a) and $J = 1$, $K = 1$, in panel (b). The coupled and uncoupled results are shown by solid and dashed lines types, respectively.

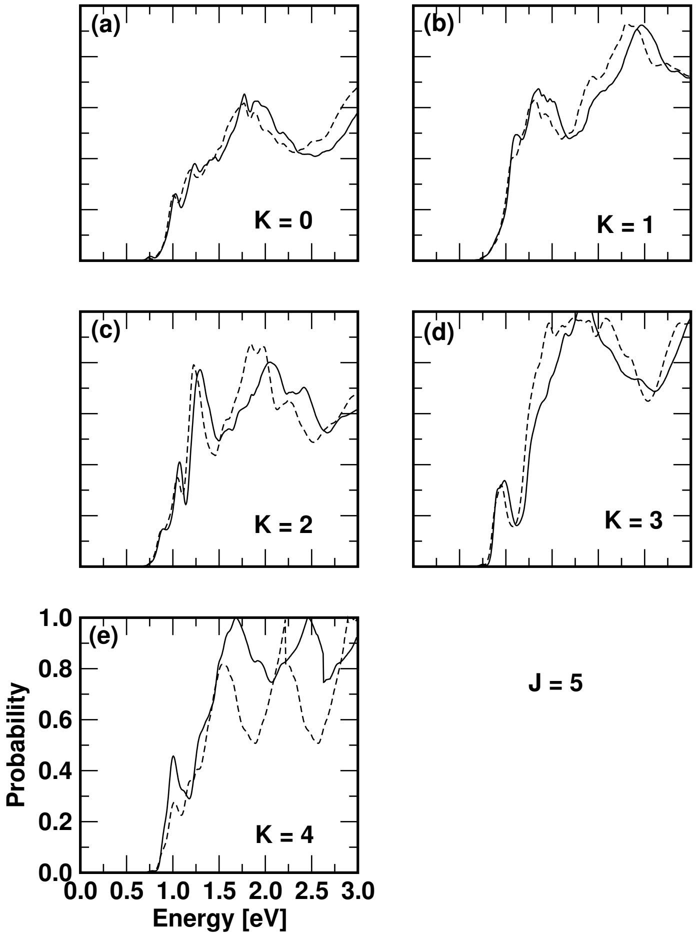

Figure 3.29: Same as in Fig. 3.28 for H + H_2 $(v = 0, j = 0)$ and for $J = 5$, $K =$ 0 - 4, in panels (a) - (e), respectively.

and dashed line types, respectively. It can be seen from Figs. 3.29 (a - e) that the difference between the coupled and uncoupled reaction probabilities increases with the increase in the K quantum number.

But as J increases, the difference between the coupled and uncoupled surface results reduces for any value of $K = 0$ to K_{max} which can be seen the in the Figs. 3.29 (a - e) where the CC reaction probabilities for $J = 15$ and $K = 0$ to 4 are plotted. The coupled and uncoupled surface results are shown by full and dashed

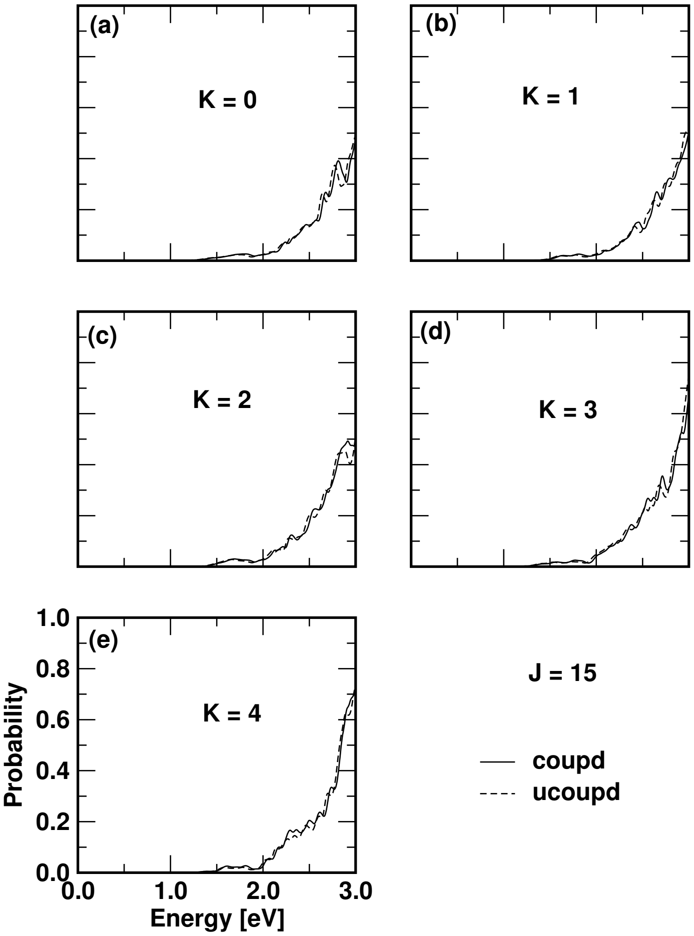

Figure 3.30: Same as in Fig. 3.28 for H + H_2 $(v = 0, j = 0)$ and for J = 15, K = 0 - 4, in panels (a) - (e), respectively.

line types, respectively.

3.5 Summary

We presented a theoretical account of the electronic nonadiabatic coupling effects on the dynamics of H + H_2 and its isotopic variants. The H + H_2 reaction occurs on the lower adiabtic sheet of its JT-split degenerate ground electronic manifold.

The quantum dynamical simulations are carried out by constructing suitable diabatic electronic states and by a time-dependent WP propagation approach within the CS approximation. Calculations of quantum dynamical quantities *e.g.,* initial state-selected energy resolved total reaction probabilities, integral reaction cross sections and thermal rate constants are carried out both in the uncoupled and coupled surface situations in order to explicitly examine the effect of surface coupling on the reaction dynamics.

The quantum dynamical results of these reactions reveal only minor impact of the nonadiabatic coupling on them. The effect of the surface coupling shows up only beyond the energetic minimum of the seam of conical intersections. Even though the reaction probability results show some sensitivity to this coupling (quite substantial in the channel specific reaction probabilities and reaction cross sections of H + HD reaction, cf., Figs. 3.7(a - b) and 3.18 (a - d)), the effect averages out in the total integral reaction cross sections with inclusion of the contributions from many partial waves. The Boltzmann averaged thermal rate constants are found to be essentially same in the uncoupled and coupled surface situations for both the reactions. The investigations reported in this paper are extended to a wide energy range starting from the onset of the reaction to the three-body dissociation limit. The findings of this paper are in general agreement with the recent literature data obtained by including the GP effect only. The reactivity of the hydrogen exchange reaction appears to vary with with isotopic substitution in the following order D + H2 < H + H2 < H + HD < H + D2 (cf., Figs. 3.1 (a), 3.5, 3.6, 3.7 (c), 3.8 (a-d), 3.10 (a-d), 3.11 (a-d) and 3.12 (a-d)).

We reiterate that the seam of CIs in H_3 occurs at the D_{3h} configuration whereas, the minimum energy path for the reactive scattering occurs at the collinear geometry, and this is perhaps the main reason that no dramatic surface coupling effect can be seen in the dynamics of this prototypical reaction. To this end we mention that the CS approximation is accurate enough for the title reaction. Inclusion of coriolis coupling does not dramatically change the integral reaction cross sections, it only alters very slightly the trend of variation of the reaction cross sections with reagent rotational excitation as noted in a recent publication [161]. Additionally, in a most recent work the GP effects on the coriolis coupling terms are predicted to be very small [76]. Therefore, the general findings of above are not expected to change dramatically on inclusion of the coriolis coupling terms in the dynamics. This work is currently underway.

Chapter 4

Quantum wave packet dynamics of N(^2D) + H_2 reaction

4.1 Introduction

In this chapter, the reaction probability, reaction cross section and thermal rate constant results obtained for the N(^2D) + H_2 insertion reaction employing the recently developed *ab initio* PES of Ho *et al.* [110] are presented and discussed. For this reaction partial wave contributions upto the total angular momentum J = 55 were necessary to obtain converged integral reaction cross sections up to a collision energy of 1.0 eV within the CS approximation [135, 136]. The thermal rate constants are calculated from the reaction cross sections and compared with the available experimental and other theoretical results. We also present and discuss the typical resonances formed during the course of the reaction and elucidate the insertion type mechanism for the product formation. The vibrational levels supported by the deep well ($\sim$ 5.5) eV of the 1 $^2A''$ PES of NH_2 are also calculated for the total angular momentum $J = 0$. A statistical analysis of the spacing between the adjacent levels of this energy spectrum is performed and the extent of irregularity in the spectral sequence is assessed.

4.2 Theoretical and computational details

4.2.1 Integral reaction cross sections and thermal rate constants

Integral reaction cross sections and the thermal rate constants of the N + H_2 reaction are calculated here by a time-dependent WP propagation approach [134, 150,162,163] as discussed in chapter 2. In this approach, the nuclear motion on the potential energy hypersurface is monitored by solving the TDSE (c.f., Eq. (2.1)) in the reactant channel (N + H_2) body-fixed Jacobi coordinates R, r and γ. A second-order split-operator scheme in conjunction with FFT and DVR methods is utilized to propagate the WPs and the reaction probabilities are calculated by the flux operator method discussed above.

4.2.2 Vibrational energy level spectrum of the NH_2 radical

The potential energy well of depth $\sim$ 5.5 eV in the $1\ ^2A''$ ground electronic state of the NH_2 occurring at the C_{2v} symmetry configuration is expected to support a large number of bound states corresponding to the vibrational energy levels of this radical. In addition, a large number of quasibound vibrational levels is also expected to be supported by the PES. In the following, the calculation of the vibrational energy level spectrum by a time-dependent WP method is discussed. In this method, the pseudospectrum pertinent to the Franck-Condon transition of a hypothetical initial state to the (final) Born-Oppenheimer PES of the N (^2D) + H_2 system is calculated. In the time-dependent picture, the golden rule expression for the spectral intensity is given by

$$P(E) \approx Re\int_0^\infty C(t)e^{iEt/\hbar}dt. \tag{4.1}$$

The quantity, $C(t) = \langle\Psi(t=0)|\Psi(t)\rangle$, in the above equation is the autocorrelation function of the system at time t. This is calculated by propagating a hypothetical initial state, $|\Psi(t=0)\rangle$ on the adiabatic (final) 1 $^2A''$ PES with the aid of the TDSE (Eq. (2.1)). As described in the previous section, the latter is numerically solved employing a mixed grid/basis set method. A 128×128 spatial grid is used in the $R \times r$ plane with $0.1\ a_0 \leq R \leq 12.8\ a_0$ and $0.1\ a_0 \leq r \leq 12.8\ a_0$. The nodes of a 47-point GLQ are used for the grid along Jacobi angle γ. The WP is propagated for a total time of $\sim$ 2.21 fs with a step length, Δt = 0.135 fs. The damping function [149] is activated at $R_{damp} = 10.2\ a_0$ and $r_{damp} = 9.6\ a_0$, to absorb the WP components reaching the grid edges at longer times.

The initial wavefunction, $|\Psi(t=0)\rangle$ pertinent to NH_2 is assumed to be a stationary GWP constructed in terms of the Jacobi coordinates

$$\begin{aligned}|\Psi(R,r,\gamma,t=0)\rangle &= N\sqrt{w(n)}\exp\left[-\frac{(R-R_0)^2}{2\delta_R^2} - \frac{(r-r_0)^2}{2\delta_r^2}\right] \\ &\times \left\{\exp\left[-\frac{(\gamma-\gamma_0)^2}{2\delta_\gamma^2}\right] + \exp\left[-\frac{(\gamma-\pi+\gamma_0)^2}{2\delta_\gamma^2}\right]\right\}. \end{aligned}\tag{4.2}$$

This GWP is initially located in the well region as well as in the barrier region along the minimum energy path of the $1^2A''$ PES of NH_2. The quantities R_0, r_0 and γ_0 specify the initial location and δ_R, δ_r and δ_γ refer to the width parameters of the GWP along the respective coordinates. The vibrational levels of NH_2 are

Table 4.1: Parameters for the different choices of the initial GWP used in the calculation of vibrational energy level spectrum of NH_2.

GWP	R_0 (a_0)	r_0 (a_0)	γ_0 (rad)	δ_R (a_0)	δ_r (a_0)	δ_γ (rad)	$\langle E \rangle$ (eV)
1	1.2275	3.0389	1.5708	0.35	0.25	0.10	-4.5983
2	1.4888	2.6398	1.5708	0.35	0.25	0.10	-4.3769
3	1.5656	2.5068	1.5708	0.35	0.25	0.10	-4.1961
4	1.6271	2.4147	1.5708	0.35	0.25	0.10	-4.0373
5	1.6655	2.2715	1.5708	0.35	0.25	0.10	-3.7841
6	1.7039	2.1793	1.5708	0.35	0.25	0.10	-3.5905
7	1.7654	2.1179	1.5708	0.35	0.25	0.10	-3.4290
8	1.8038	2.0463	1.5708	0.35	0.25	0.10	-3.2506
9	1.8422	1.9645	1.5708	0.35	0.25	0.10	-3.0383
10	1.8730	1.9030	1.5708	0.35	0.25	0.10	-2.8675
11	2.0881	1.6370	1.5708	0.35	0.25	0.10	-1.9077
12	2.3340	1.6677	1.5708	0.35	0.25	0.10	-1.4914
13	2.4493	1.5961	1.5708	0.35	0.25	0.10	-1.0897
14	2.9026	1.5654	1.5708	0.35	0.25	0.10	-0.1526
15	4.3241	1.4221	1.5708	0.35	0.25	0.10	0.7196
16	4.0	1.41	1.5708	0.35	0.25	0.10	0.7196

obtained with appreciable intensity by suitably varying the initial location and the width parameters of this GWP. The initial parameters and average energies of the GWPs used in the present calculations are given in Table 4.1. The convergence of each calculation is checked by varying the numerical grid parameters mentioned above.

The pseudospectral intensity (cf., Eq. (4.1)) when plotted as a function of energy yields peaks at the energy eigenvalues of the vibrational levels. The eigenfunctions of these levels are calculated by the spectral quantization algorithm [164]: by projecting a time-evolved WP onto the desired eigenstate (n) of energy E_n,

$$\Psi_n(E) = \int_0^T e^{iE_n t/\hbar}\Psi(t)dt. \qquad (4.3)$$

4.3 Results and Discussion

4.3.1 Reaction Probability, Integral Reaction Cross Section and Thermal Rate Constant

The reaction probabilities are calculated up to a total energy of 1.27 eV. In the CS model inclusion of partial-wave contributions up to $J = 55$ are found to be necessary to obtain converged integral reaction cross section results in this energy range. The convergence of each calculation is checked with respect to the choice of the numerical grid parameters given in Table 4.2. The reaction probabilities are found to be very sensitive to the location of the initial GWP at the asymptotic reactant channel. The reaction probabilities vary dramatically particularly for the higher values of J and exceeds its limiting value when this parameter is varied. Also the probabilities are sensitive to the choice of the spacing of the grid along R (this may be due to the possible artifacts of the PES arising from the grid representation). The slowly decaying centrifugal potential for higher J values will result a wrong value of the right hand side of Eq. (2.33), if it is not zero at the location of the initial WP. Therefore, we have located the latter far out in the asymptotic reactant channel (cf., Table 4.2) in the present study to obtain the correct reactant asymptote. An alternative to this problem is also advocated in a study by Schatz and coworkers [165].

The N (^2D) + H$_2$ $(v = 0, j = 0)$ reaction probability values as a function of the collision energy E are plotted in Fig. 4.1 for a few selected values of the total

Table 4.2: Numerical grid parameters and properties of the initial wavefunction used in the N + H_2 scattering study

Parameter	Value	Description
$N_R/N_r/N_\gamma$	512/64/48	Number of grid points
R_{min}/R_{max} (a_0)	0.1/86.97	Extension of the grid along R
r_{min}/r_{max} (a_0)	0.5/8.06	Extension of the grid along r
$\Delta R/\Delta r$ (a_0)	0.17/0.12	Grid spacings along R and r
r_d (a_0)	4.94	Location of the dividing surface in the product channel
R_{mask}/r_{mask} (a_0)	74.5 /5.06	Starting point of the masking function
R_0 (a_0)	73.5	Initial location of the center of the GWP in the coordinate space
E_{trans} (eV)	0.44	Initial translational kinetic energy
δ (a_0)	0.30	Initial width parameter of the GWP
Δt (fs)	0.135	Length of the time step used in the WP propagation
T (ps)	1.1	Total propagation time

angular momentum, J = 0, 10, 20, 30, 40, 50 and 55 (indicated in the panel) and for $\Omega = 0$. These represent the initial state-selected and energy resolved total (summed over all open v' and j' levels of the product NH at a given energy) reaction probabilities. It can be seen that the reaction has a threshold, because of the intrinsic barrier ($\sim$ 0.08 eV) in the PES, which shifts to the higher energy with increasing contribution from the centrifugal barrier for higher J values. The probabilities show a very sharp rise near the threshold and then oscillate at higher energies for all J values. The reaction probability for $J = 0$ shows a sharp peak at a collision energy of $\sim$ 0.08 eV near the threshold region. A similar peak has also been observed by Lin *et al.* [111] and Castillo *et al.* [116] in their WP calculations and is attributed to the formation of a shape resonance at the C_{2v} transition state [116]. The oscillations seen in the reaction probability curves of Fig. 4.1 can be attributed to a large number of quasibound vibrational levels supported by the 1 $^2A''$ PES.

In Fig. 4.2(a) we show the calculated reaction probabilities for $J = 0$, $\Omega = 0$ and for different values of the diatomic rotational angular momentum, j = 1 - 3. The general trend of a sharp increase of the probability near the threshold and a tendency to oscillate later can also be seen from the figure. A similar behavior can be seen in Fig. 4.2(b) where the probabilities for $J = 0$, $\Omega = 0$ and for v = 1 is plotted. Fig. 4.2(c) shows the calculated reaction probabilities for $J = 12$ and for Ω = 0 - 3. We can see from the Fig. 4.2(c) that the reaction threshold increases with an increase in the values of j and Ω. For a Fixed J, this causes an increase of the height of the effective barrier to the reaction, i.e., due to the term $j(j+1)/2\mu R^2$. The general tendency of sharp rise of the reaction probabilities near threshold and then to oscillate later can also be seen from this figure.

The integral reaction cross section results as a function of collision energy

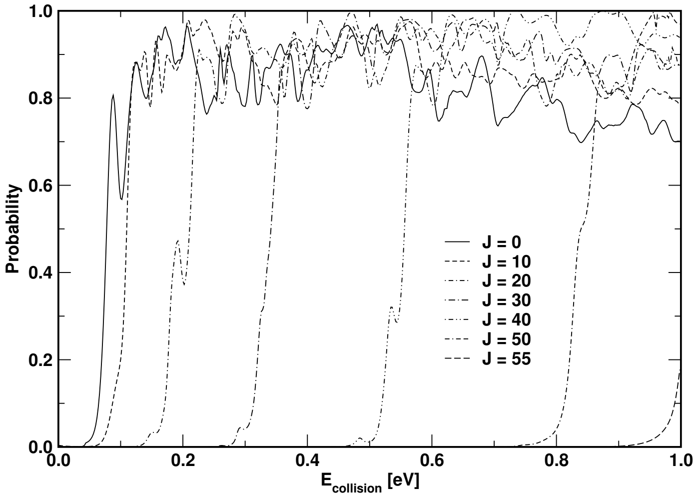

Figure 4.1: Total reaction probability as a function of the collision energy E for the N + H_2 ($v = 0, j = 0$) → NH ($\sum v', \sum j'$) reaction for the total angular momentum, J = 0, 10, 20, 30, 40 and 45 indicated by different line types in the figure.

calculated by Eq. (2.37) for the N + H_2 ($v = 0, j$) reaction for four different values of j (indicated in the panel) are shown in Fig. 4.3. The cross section values increase monotonically with increasing collision energy and reach to a plateau at high energies. It can be seen from Fig. 4.3 that the cross section values increase with the rotational excitations of the reagent diatom. The resonance oscillations also persist in the cross section results, though they are much weaker compared to those in the reaction probability results. This is because the oscillations in the probability results average out with different partial wave contribution of the total angular momentum J in the cross section results. It is also observed that the integral reaction cross sections (in the given energy range) decrease when H_2 is excited by one vibrational quantum (result not shown here for brevity).

The thermal rate constants obtained by statistically averaging over the rotational states $j = 0$ to 3, are compared with the experimental and other theoretical

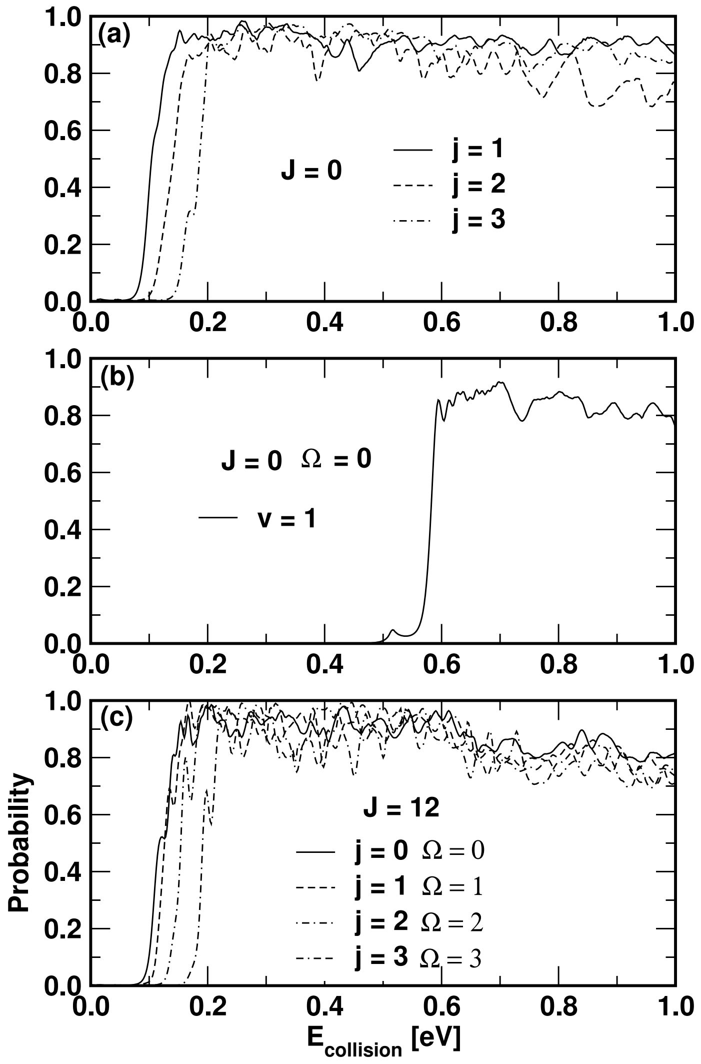

Figure 4.2: Same as in Fig. 4.1 for (a) N + H_2 $(v = 0, j = 1-3) \rightarrow$ NH $(\sum v', \sum j')$ + H (b) N + H_2 $(v = 1, j = 0) \rightarrow$ NH $(\sum v', \sum j')$ + H for $J = 0$, $\Omega = 0$ and (c) N + H_2 $(v = 0, j = 0-3) \rightarrow$ NH $(\sum v', \sum j')$ for $J = 12$, and Ω = 0 - 3.

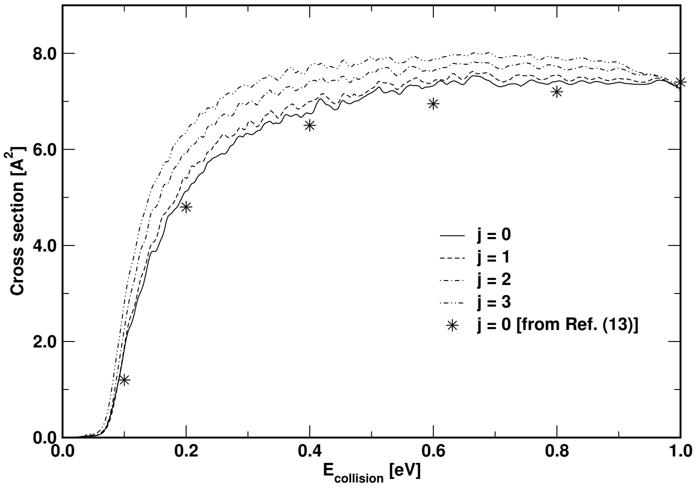

Figure 4.3: Initial state-selected integral cross sections of the N(^2D) + H$_2$ ($v = 0, j$) reaction as a function of the collision energy. The cross sections for various j values are shown by different line types indicated in the panel. The integral cross section results for j = 0 taken from Ref. [113] shown by the asterisks.

results (data extracted from the plots given in references mentioned) are shown in Fig. 4.4. It can be seen that the present results are in good accord with the available experimental results. The rate constant results exhibit the Arrhenius type of behavior as observed in the experimental results, revealing the feature of a barrier type of reaction. The rate constant values are fitted to the Arrhenius equation, K(T) = A$_0$ exp(-E_a/RT), where A$_0$ and E_a are the pre-exponential factor and activation energy for the reaction, respectively. The quantity R in the above equation denotes the universal gas constant. The fit yields the value A$_0$ = 6.37 × 10^{-11} cm^3 sec^{-1} molecule^{-1} and E$_a$ = 0.093 eV.

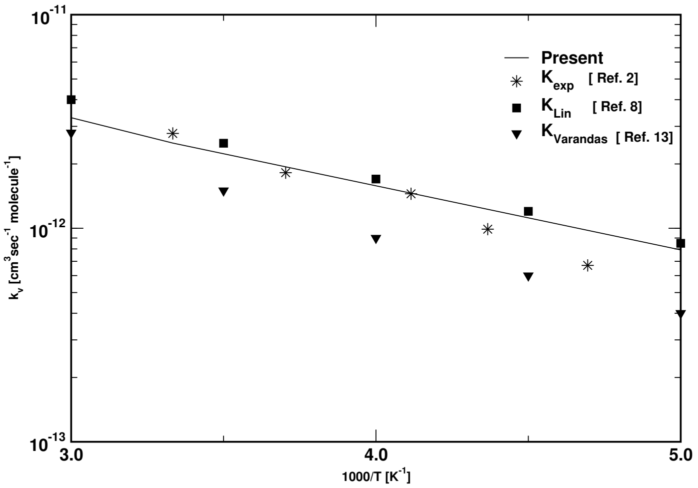

Figure 4.4: Arrhenius plot of Boltzmann averaged (over j = 0 - 3) thermal rate constants for the N + H_2 ($v = 0$) reaction. The points on the figure represents the results from the literature (K_{Exp} from Ref. [104]; K_{Lin} from Ref. [110]; $K_{Varandas}$ from Ref. [115]).

4.3.2 On the insertion type of mechanism of the N + H_2 reaction

The nature of the sharp peaks observed in the $J = 0$ probability curve in the vicinity of the threshold region of the N + H_2 reaction (cf., Fig. 4.1), were examined to understand the reaction mechanism. For this purpose, we calculate the transition state spectrum (using the pseudospectral approach described in section 4.22) by placing a suitably chosen GWP at the location of the barrier along the minimum energy path (GWP No. 16, in Table 4.1). This GWP is time evolved for a total time of $\sim$ 2.2 ps. The pseudospectrum of the quasibound states thus obtained is superimposed on the $J = 0$ reaction probability curve and is shown in Fig. 4.5 by different line types.

It can be seen from Fig. 4.5 that the peaks in the transition state spectrum can be associated with the oscillations in the reaction probability curve. It can

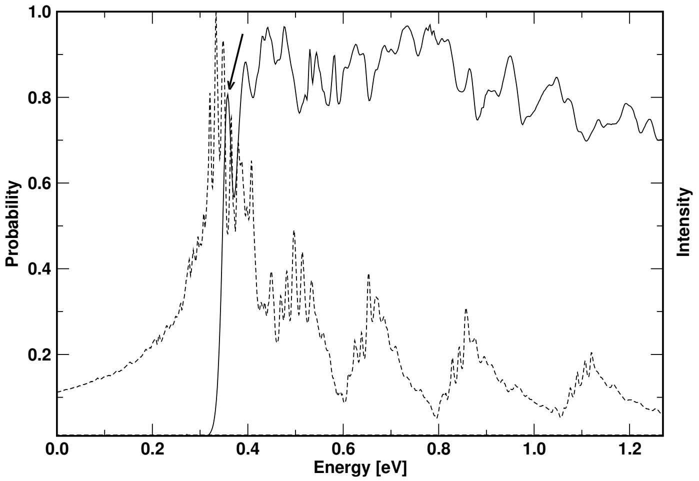

Figure 4.5: Quasibound spectrum (dashed lines) of NH_2 in the energy range 0 - 1.27 eV computed with the initial GWP no. 16 of Table 4.1. The initial state-selected total reaction probability for $J = 0$ is superimposed on the quasibound spectrum and by the solid line.

also be seen from the Fig. 4.5 that the sharp peak in the reaction probability at collision energy, $E \sim 0.08$ eV (0.35 eV total energy) corresponds to the peak marked by arrow in the transition state spectrum. To characterize this further, we computed the eigenfunctions of first few peaks around 0.08 eV. The eigenfunction of the resonance peak indicated by an arrow in Fig. 4.5 is shown in Fig. 4.6. The probability density contours of resonance eigenfunction (indicated by an arrow in Fig. 4.5) are plotted in the (R, r) and (γ, R) planes and are shown in Fig. 4.6.

The energy eigenvalue (total energy) of the peak is included in panel of Fig. 4.6. We can see from Fig. 4.6(b) that there is a heavy buildup of the probability density near the Jacobi angle, $\gamma = \frac{\pi}{2}$, revealing a C_{2v} configuration of the quasibound complex. Lifetimes of first few resonances have been estimated from the width of the spectral peaks fitted to a Lorentzian function and also from the decay of these states in time and the resulting data are collected in Table 4.3. In order to better understand the mechanistic aspects of the N (^2D) + H_2

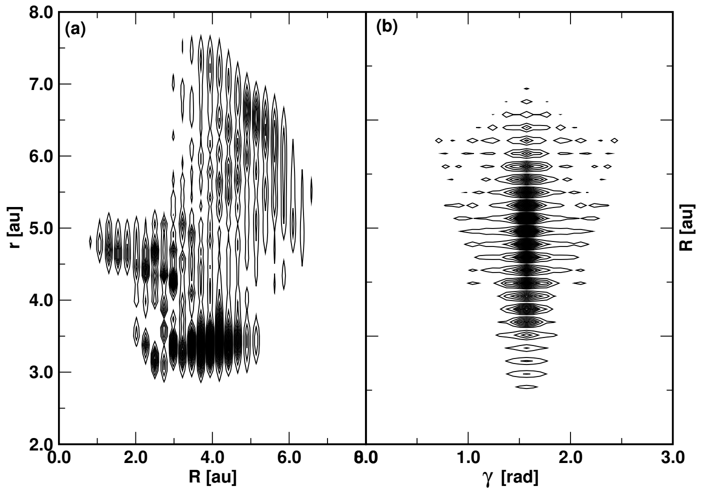

Figure 4.6: Probability density contours of the eigenfunction of resonance peak (indicated by an arrow in Fig. 5) of NH_2 (occurring near the barrier region of the PES) averaged over γ and r are plotted in the (R, r) and (γ, R) planes, respectively.

$(v = 0, j = 0)$ reaction dynamics, we examined the time evolution of the decaying resonance shown in Fig. 4.6.

The probability density of this decaying resonance averaged over γ and r at different times (indicated in the panel) are shown in the left and right columns of the Fig. 4.7, respectively. This wavefuncion is scattered symmetrically on either side of the T - shaped configuration at latter times (not shown here for brevity). Heavy buildup of probability density near $\gamma = \frac{\pi}{2}$ implies that N atom approaches perpendicularly to the H_2 molecule supporting an insertion type of mechanism of the reaction dynamics [107, 108].

This reveals that the scattering occurs through a C_{2v} geometry and the reaction proceeds through an insertion mechanism consistent with the experimental observations.

The reaction path for the C_{2v} approach of the N atom is sketched in Fig. 4.8. It reveals a barrier height of $\sim$ 0.08 eV. The topography of the barrier

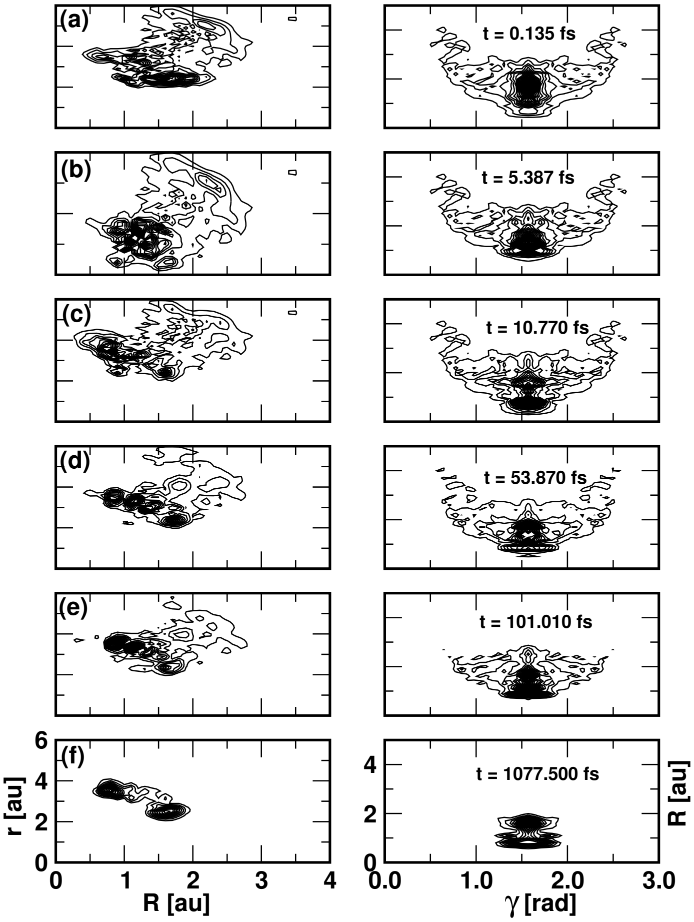

Figure 4.7: Time evolution of the quasibound eigen function of panel (b) of Fig. 7 displaying an insertion type of mechanism of the N + H_2 reaction dynamics.

Table 4.3: Energy (E), line-width lifetime ($\tau_{linewidth}$) and decay lifetime (τ_{decay}) of first three resonances near the barrier along the C_{2v} reaction path of NH_2.

GWP	E	$\tau_{linewidth}$	τ_{decay}
	(eV)	(fs)	(fs)
1	0.33384	77.53	77.64
2	0.34771	52.65	94.30
3	0.36511	122.43	125.72

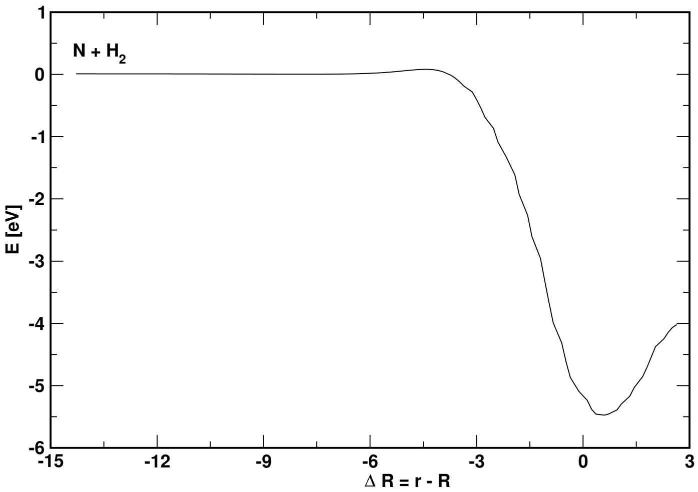

Figure 4.8: A schematic plot of the C_{2v} reaction path of N + H$_2$ reaction.

region exhibits no local minimum. Therefore, the observed sharp resonances in the vicinity of this region are of barrier type [166] rather than of shape type as noted in Ref. [116].

4.3.3 Vibrational energy level spectrum of the $1^2A''$ electronic state of NH$_2$

In this section we present the vibrational energy level spectrum of NH$_2$ supported by the deep well of its $1^2A''$ PES. These vibrational levels are calculated by the pseudospectral approach as discussed in section II. Eigenfunctions of first few energetically low-lying and well separated vibrational levels are calculated and assigned. A total of $\sim$ 400 vibrational levels are calculated. The NNSD of these vibrational level spectrum is examined in order to assess the short-range correlations and the extent of level repulsions in the spectral sequence.

In Fig. 4.9 we show a typical vibrational energy level spectrum of NH$_2$ calculated using the initial GWP No. 4 of Table 4.1. The intensity in arbitrary units is

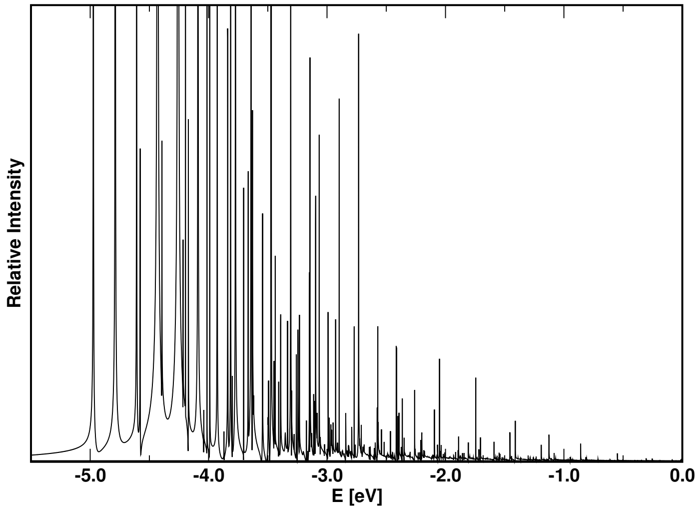

Figure 4.9: A typical vibrational energy level spectrum of NH_2, computed with the GWP No. 4 (cf., Table 4.1). The intensity is plotted in arbitrary units as a function of energy of the vibrational levels. The zero of energy corresponds to asymptotically separated N + H_2 reactants.

plotted as a function of the energy of the vibrational levels of the $1^2A''$ electronic state. Energy is measured from the bottom of the well of the $1^2A''$ PES and the zero of energy corresponds to asymptotically separated N + H_2 reactants. The peaks in the spectrum correspond to the vibrational energy levels of the NH_2 radical and energy corresponding to the peak maximum represents the vibrational energy eigenvalues. The nature of the peaks implies that the levels are of bound type. The WP is time evolved for 2.21 ps which leads to an energy resolution of $\sim$ 0.002 eV in the spectrum. This resolution is obtained by effectively doubling the propagation time obtained by calculating $C(2t)$ from $\Psi(t)$ [167]. It can be seen from Fig. 4.9 that at low energies near the bottom of the well, resolved peaks are obtained. The number of peaks in the spectrum increases significantly with an increase in energy. The energetic minimum of the well of the $1^2A''$ PES occurs at $\sim$ -5.5 eV for the C_{2v} geometry of NH_2. It can be seen that the 0 - 0 line in the spectrum of Fig. 4.9 occurs close to this energy. The zero point vibrational energy of NH_2 is estimated to be $\sim$ 0.527 eV. Approximately 400 vibrational levels are calculated by varying the location of the initial WP (a set of 15 WP calculations are carried out and the parameters are given in Table 4.1) in the well region of the $1^2A''$ PES.

Instead of giving an exhaustive list of 400 vibrational levels, it would rather be useful to analyze these levels in order to understand the nature of intramolecular motion in NH_2. The eigenfunctions of some these vibrational levels are calculated by Eq. (4.3) and their probability density ($|\Psi(E)|^2$) contours are plotted in Figs. 4.10 (a - f) and Figs. 4.11 (a - g) in the (R, r) and (γ, R) plane averaged over γ and r, respectively. The eigenfunctions in Figs. 4.10 (a - f) reveal local mode behavior and exhibit nodal progression along R, r and γ coordinates. The eigenfunctions in Figs. 4.11 (a - g), on the other hand, reveal hyperspherical mode type of behavior and exhibit nodal progression along the polar angle, Φ $(= tan^{-1}(\frac{r}{R}))$ [168, 169].

The eigenfunction of Fig. 4.10 (a) represents the vibrational ground level (the 0 - 0 line of Fig. 4.9) of NH_2. It does not contain any node along any of the three Jacobi coordinates. This level occurs at $\sim$ -4.973 eV and $\sim$ 0.53 eV above the minimum of the well of the $1^2A''$ PES. The latter therefore corresponds to the zero point vibrational energy of the $1^2A''$ electronic state of NH_2. The contour diagram in the (γ, R) plane reveal heavy build-up of probability density near $\gamma = \pi/2$, implying a T - shaped configuration of NH_2. The eigenfunction in Fig. 4.10 (b) represents one quantum excitation predominantly along R and corresponds to the fundamental level along this coordinate. The vibrational quantum of energy along this coordinate is about 0.184 eV. This vibrational level can be assigned as (1, 0, 0) according to the number of nodes along (R, r, γ) coordinates, respectively. The vibrational wavefunctions in panel (c) and (d) reveal excitations

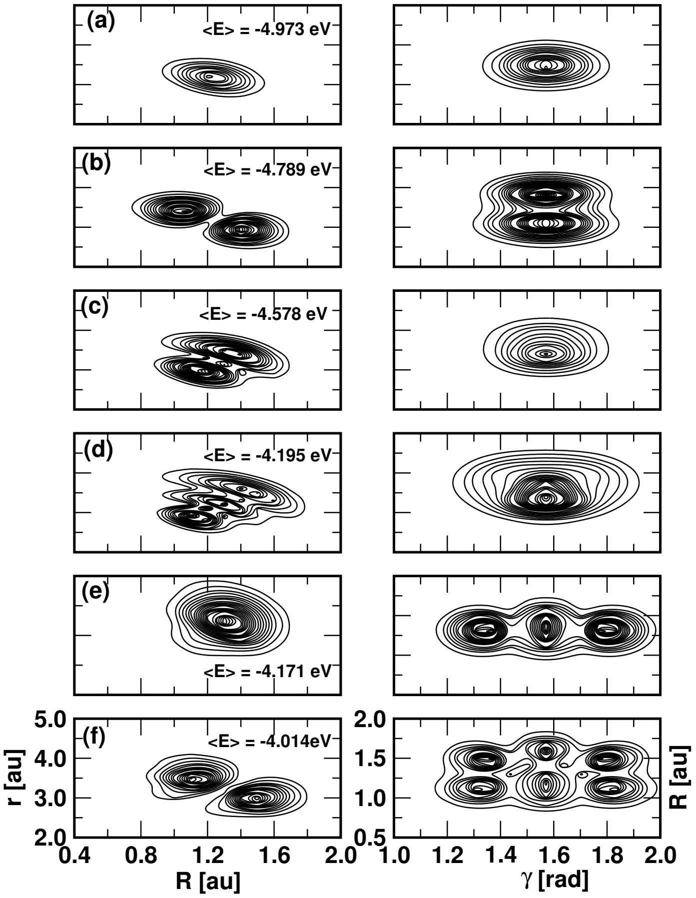

Figure 4.10: Probability density contours of the eigenfunctions of the low-lying vibrational levels of NH_2. The contours are plotted in the (R, r) plane averaged over γ (left column) and (γ, R) plane averaged over r (right column), to clearly reveal the nodal pattern in them.

along the r coordinate and can be assigned as (0, 1, 0) and (0, 2, 0), respectively. The vibrational quantum of energy along this coordinate is $\sim$ 0.395 eV. The vibrational wavefunctions in panel (e) and (f) reveal two quanta excitation along γ. In addition, the latter also reveals one quantum excitation along R. These wavefunctions can be assigned as (0, 0, 2) and(1, 0 , 2), respectively.

In contrast to Figs. 4.10 (a - f), the vibrational wavefunctions in Figs. 4.11 (a - g) do not reveal distinct excitations along the R, r and γ coordinates and a clear assignment of these wavefunctions according to the above prescription is impossible.

The progressions in the wavefunctions in Figs. 4.11 (a - g) can be assigned according to (ν_R, ν_P) specifications as discussed earlier in the literature [168,169]. The quantities ν_R and ν_P correspond to the number of nodes along the reactant ($N + H_2$) and product (NH + H) channels, respectively. Although the present system do not have high symmetry, for practical convenience the diagonal line in the (R, r) plane can be roughly assumed to separate the products from the reactants. According to this nomenclature the eigenfunctions of panel (a), (c), (e) and (f) correspond to a $\nu_R = \nu_P$ progression, and can be defined as (1, 1), (2, 2), (3, 3) and (1, 1), respectively. In addition, the one in panel (f) also reveals two quanta excitation along γ. The eigenfunctions in panel (b) and (d) of Fig. 4.11 correspond to a $\nu_R = \nu_P$ - 1 progression, with (1, 2) and (2, 3) for (ν_R, ν_P), respectively. This kind of analysis and assignment of wavefunctions was previously done by Sadeghi and Skodje for the $D + H_2$ resonances [168] and by Mahapatra and Sathyamurthy for the $He + H_2^+$ resonances [169]. While $\nu_P = \nu_R$ - 1 and $\nu_P = \nu_R$ - 2, progressions were found for the $D + H_2$ resonances, $\nu_R = \nu_P$, $\nu_R = \nu_P$ - 3 and $\nu_R = \nu_P$ - 4 were reported for the $He + H_2^+$ resonances. At further high energies the vibrational wavefunctions reveal complex and irregular nodal

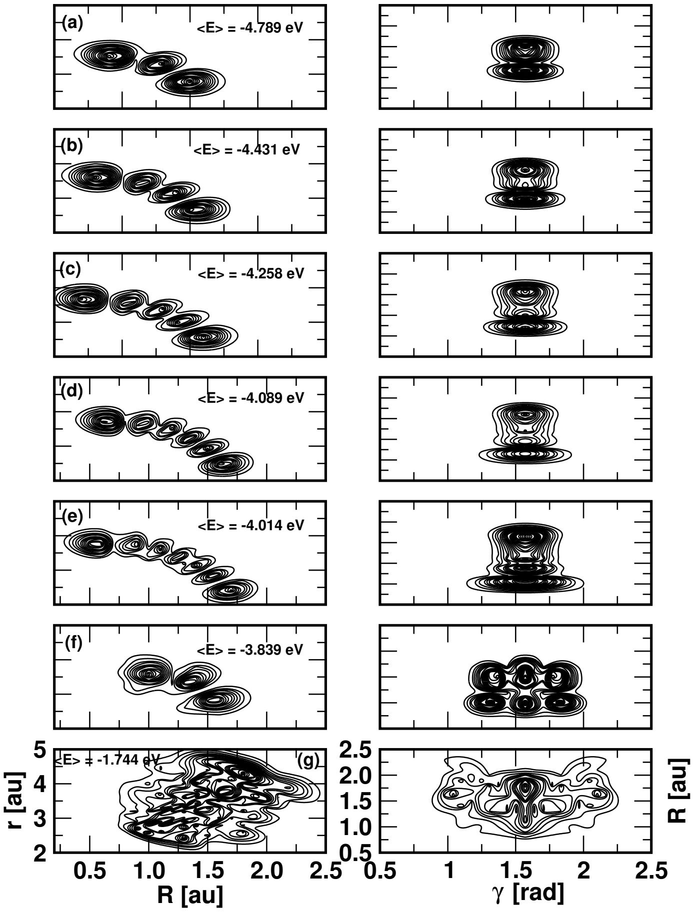

Figure 4.11: Same as in Fig. 4.10.

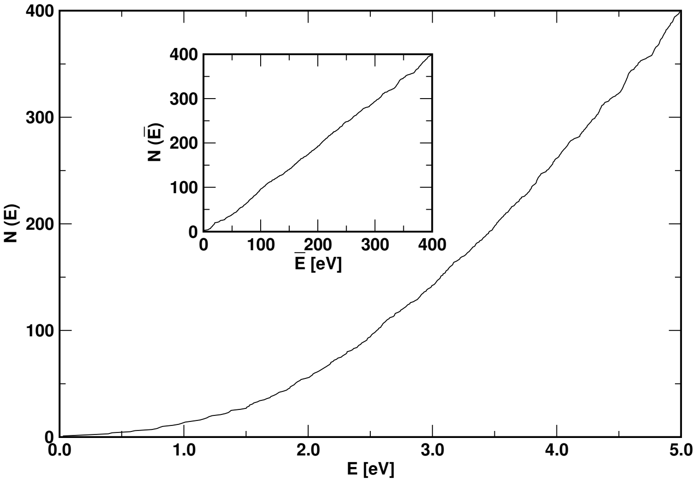

Figure 4.12: The quantum mechanical sum of states $N(E)$ as a function of energy E, derived from the folded vibrational level spectrum of the $1^2A''$ electronic state of NH_2. The corresponding unfolded spectrum is shown as an inset.

pattern which indicates quite a strong coupling between the three vibrational degrees of freedom of NH_2. For illustration, a typical wavefunction is shown in Fig. 4.11(g), for which no clear assignments can be made.

In order to have an insight of the extent of coupling between the three degrees of freedom and the observed complex pattern of the vibrational wavefunctions at higher energies we examine the calculated $\sim$ 400 vibrational levels for short-range correlations by analyzing the NNSD [170]. Prior to the application of this statistical analysis, the energy spectrum is unfolded, *i.e.,* the energy values are scaled with respect to a constant mean energy level spacing. This makes the average density of levels uniform over the entire energy range and removes the irrelevant secular variations of the spacing (decrease of spacing with energy), keeping the fluctuating variations unaffected. The quantum mechanical sum of states $N(E)$ (up to the energy E) as a function E is plotted in Fig. 4.12. It can be seen from Fig. 4.12 that $N(E)$ reveals the characteristics of a staircase

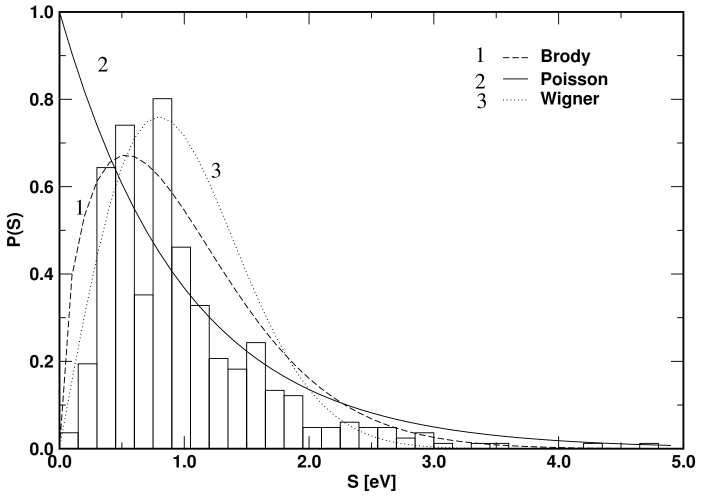

Figure 4.13: The nearest neighbor spacing distribution $P(s)$ as a function of the spacing s between energy levels derived from the unfolded bound state spectrum of NH_2 given in Fig. 8. Poisson (curve 1) and Wigner (curve 2) distributions correspond to the regular and irregular limits, respectively. The best fit of the histogram to the Brody distribution with $q = 0.7$ (see text) is included in the figure by curve 3.

function. This staircase function becomes almost a straight line (see the inset in Fig. 4.12) when the unfolded energy values $\overline{E_i}$ are used. These unfolded energy values are used to estimate the correlation between the adjacent energy levels by analyzing the NNSD, $P(s)$, where $s_i = \overline{E_{i+1}} - \overline{E_i}$, i = 1, 2, 3, ..., N-1.

In absence of any correlation between the adjacent energy levels, the NNSD becomes an exponential function, *i.e.,* $P(s)$ = exp(-s). This is the regular limit of the variation of the spacing, and is called the Poisson limit [171]. Therefore a classically integrable system shows "level clustering", $P(s) \rightarrow 1$ as $s \rightarrow 0$, indicating no correlation between the adjacent energy levels. On the other hand, for a classically chaotic system this distribution in the semiclassical limit is given by the Wigner surmise [170, 172], $P(s) = (\pi\ \mathrm{s}/2)\exp[-(\pi\ s^2)/4]$, which is the GOE limit of the Hermitian matrices. In this case one finds, $P(s) \rightarrow 0$ as $s \rightarrow$

0, indicating a "level repulsion", which means that the adjacent energy levels are strongly coupled. The NNSD obtained from the unfolded vibrational energy level spectrum of NH_2 is presented in Fig. 4.13, in the form of a histogram plot. Curves 2 and 3 are the regular (Poisson) and irregular (Wigner) limits of the distribution, respectively. It is evident from the histogram that the observed distribution does not correspond fully to either of the two limits. It exhibits an intermediate type of behavior. In order to estimate the extent of irregularity in the spectral sequence, we have fitted the histogram to the Brody distribution [173]: $P(s) = as^q e[(-bs^{1+q})]$, where, $a = (1 + q)\ b$, and $b = \Gamma[(2+q)/(1+q)]^{1+q}$; this distribution interpolates between the Poisson and Wigner limits by varying q in the range of 0 - 1. A value of $q = 0.7$ shown by the dashed lines (curve 1), in Fig. 4.13 can be seen to yield a good fit to the histogram. This reveals that at least ~ 70 % of the phase space contributes to the irregular spectral sequence. This is expected to initiate a large number of chaotic trajectories in the dynamics of N + H_2 reaction.

4.4 Summary

We have calculated the initial state-selected total reaction probabilities, integral reaction cross sections and thermal rate constants of the N + H_2 reaction in its $1^2A''$ electronic ground state for the total angular momentum, $J \neq 0$ within the CS approximation. The integral reaction cross sections are reported over an extended range of collision energies up to 1.0 eV. The calculated thermal rate constants are somewhat in better agreement with the experimental results compared to the available theoretical results. The transition state spectrum of NH_2 is calculated by locating suitable GWP at the location of the transition state. The eigenfunctions of first few transition state resonances are computed. The linewidth and decaylife times of these resonances are calculated. The insertion type of mechanism for the N + H_2 reaction dynamics is examined by time evolving a suitable resonance. The vibrational energy level spectrum of the $1^2A''$ electronic state of NH_2 radical is also calculated for the total angular momentum $J = 0$. We obtained $\sim$ 400 vibrational levels supported by the deep well ($\sim$ 5.5 eV) of the $1^2A''$ electronic state of NH_2 radical. Some of the low-lying vibrational levels are characterized by examining the nodal pattern in their eigenfunctions. The eigenfunctions reveal both local and hyperspherical types of nodal structures. Well defined nodal structures are found at low energies which become irregular with increase in the energy. The irregularity of the spectral sequence is further analyzed by analyzing the NNSD, which correlates to a Brody distribution revealing an irregularity index of 0.7.

Chapter 5

On the $(E \otimes e)$-Jahn-Teller CIs in the 3p (E') and 3d (E'') Rydberg electronic states of triatomic hydrogen

5.1 Introduction

A theoretical account of the static and dynamic aspects of the JT interactions in the 3p (E') and 3d (E'') Rydberg electronic states of H_3 are presented in this chapter. The static aspects are discussed based on *ab initio* quantum chemistry results, and the dynamic aspects are examined in terms of the vibronic spectra and nonradiative decay behavior of these states. The adiabatic PESs of these degenerate electronic states are derived from extensive *ab initio* calculations. The calculated adiabatic PESs are diabatized as illustrated in chapter 2 [174]. The nuclear dynamics on the coupled diabatic electronic states is simulated by propagating WPs with the aid of the TDSE. Calculations are performed both for the uncoupled and coupled state situations in order to understand the importance of nonadiabatic interactions due to the JT CIs in these excited Rydberg electronic states.

The *ab initio* adiabatic potential energies of the JT split components of the 3p (E') , 3d (E'') and several other excited Rydberg electronic states of H_3 were calculated over a large number of geometrical arrangements by Jungen and coworkers [175]. The vicinity of the D_{3h} equilibrium geometry of Rydberg excited H_3 is probed by the electron collision of H_3^+ in molecular beams [94, 95]. Therefore, it is valuable to understand the topography of the PESs of the 3p (E') and 3d (E'') electronic states in the neighborhood of the D_{3h} configuration and the motion of the WP on them (these two states have major contributions to the Rydberg emission process [94,95]). Like the 2p (E') ground electronic manifold, these two degenerate Rydberg excited states are also prone to the JT instability [8]. Investigations of the impact of the JT coupling on the spectroscopy and nonradiative decay of these states are the two main aspects of the present investigation.

The CIs of the JT split 3p (E') and 3d (E'') Rydberg electronic states are established. Our analysis shows that the JT interactions are not particularly strong in these electronic states, when compared to that in the electronic ground state of H_3 [96, 174, 176]. The nonradiative decay of these states is examined by calculating the time-dependent adiabatic and diabatic electronic populations. The results show much slower decay rates of these Rydberg states when compared with the same of the electronic ground state [96, 174].

5.2 Diabatic electronic states and conical intersections

The adiabatic potential energy surfaces used in this paper are a subset of solutions from a large number of geometrical arrangements where the lowest 15 electronic states have been documented between the geometry of H_3^+ and the dissociation limit to H + H_2 [175]. An orbital basis of 165 contracted Gaussian functions has been used which can describe Rydberg dissociation to H^* + H_2 as well as to H + H_2^*. At every grid point a CI (Configuration Interaction) calculation in the dimension of about 14000 CSF's (Configuration State Function) has been performed and calculations for 2366 grid points have been carried out.

The internal coordinates of H_3 have been chosen as mass scaled Jacobi coordinates R, r and γ with

$$R = S \cdot 0.75^{-1/4} \tag{5.1a}$$

$$r = s \cdot 0.75^{1/4}. \tag{5.1b}$$

Here s is the H-H distance in the diatom, S is the distance between the third H atom and the center of mass of the diatom, and γ is the angle between the vectors $\vec{r}$ and $\vec{R}$. For the equilibrium geometry of H_3^+ (an equilateral triangle with interatomic distances of 1.65 a_0) we have $R = r = 1.536\ a_0$ and $\gamma = 90°$. Our grid has been chosen such that one point exactly coincides with this equilibrium ; the step size is 0.2 a_0 for R and r in the vicinity of the H_3^+ minimum, 0.4 a_0 at longer separations, and 15° for γ. In the following these internal coordinates will also be used for the treatment of the nuclear dynamics.

In contrast to the 2p (E') surfaces the potentials of the 3p (E') state have an absolute minimum near the geometry of H_3^+. It is a double surface which in D_{3h} symmetry penetrates itself. Close to the minimum the surfaces are roughly parallel to that of the parent ion, but in C_{2v} symmetry ($\gamma = 90°$) the higher component of the 3p (E') surfaces has a saddlepoint near $R \sim 1.0\ a_0$, $r \sim 2.6\ a_0$, about 1.3 eV above the minimum; near $R \sim 0.9\ a_0$, $r \sim 2.9\ a_0$ it intersects the lower component such that in a linear arrangement (R =0) their sequence is inverted for $r > 3.0\ a_0$.

The surfaces of the 3d (E'') state are embedded in a dense sequence of electronic states, together with 3s (A_1'), 3p (A_2''), 3d (E') and 3d (A_1'). At the equilibrium these 7 states are compressed into an energy interval of about 0.1 eV, much less than the typical zero point vibrational energies in these potentials (0.54 eV for H_3^+). The potential surfaces are qualitatively parallel to that of the parent ion and the 3d (E'') surfaces are not intersected by another potential upto an energy of about 1 eV above the minimum.

We utilized the above adiabatic potential energy data for the 3p (E') and 3d (E'') electronic states and diabatized them as discussed before in chapter 2 [22–24]. In passing we note that for a symmetry-enforced ($E \otimes e$)-JT CIs, much simplification results in the construction of the diabatic electronic states [23]. In this case the adiabatic-to-diabatic mixing angle is solely determined in a geometrical fashion and does not depend at all on the strength of the JT coupling. This is already been exploited in our earlier works on this system [25,96,174,176] and encouraging results emerged thereof. If the two adiabatic components of the JT split potential energy surfaces are designated V_- (lower) and V_+ (upper) then the diabatization scheme reads as given in Eqs. (2.5), (2.6) and (2.7).

The computed adiabatic points on a (R, r, γ) grid by Jungen and coworkers are used here [175]. The raw adiabatic data are used to calculate the diabatic potential energies at each point of the grid and the resulting diabatic surfaces are then numerically interpolated using a three-dimensional spline on a denser grid. The numerical WP calculations are carried out on the latter consisting of a uniformly spaced 128 × 128 grid in the (R, r) plane with $0.33a_0 \leq R \leq 5.13a_0$ and $1.13a_0 \leq r \leq 5.13a_0$ (for the 3p (E') electronic manifold) and $0.33a_0 \leq R \leq 3.13\ a_0$, $1.13a_0 \leq r \leq 2.33a_0$ (for the 3d (E'') electronic manifold). A 63 point GLQ [153] is used for γ in both cases. Unlike the adiabatic potential energy functions, the diabatic potential energy functions do not exhibit a cusp like behavior at the seam of CIs [12]. Therefore, it is much simpler to numerically interpolate the diabatic potential energy functions rather than the adiabatic ones.

The two diabatic components of the 3p (E') Rydberg electronic manifold of H_3 are shown in Figs. 5.1 (a-b) and indicated by the thin and thick lines. The contour lines in panel a are plotted in the (R, r) plane for $\gamma = \pi/2$ corresponding to the C_{2v} arrangements of the three nuclei. The seam of the $(E \otimes e)$-JT CIs occurring for $R = r$ is shown by the line on the diagram. H_3 possesses an equilateral triangular geometry on this line. The energetic minimum on the seam is indicated by the cross. This minimum occurs at $R = 1.56\ a_0$, $r = 1.56\ a_0$ and $\gamma = \pi/2$. This minimum point on the seam is more clearly shown in panel b and indicated by an arrow. The energy at this minimum of the seam is $\sim$ 2.43 eV relative to the three-body dissociation (H+H+H) limit.

The above two diabatic potential energy surfaces obtained from the computed adiabatic potential energy data (panels in the left column) and the corresponding interpolated ones (panels in the right column) on the denser grid (defined above) using a three-dimensional spline are shown in the (R, r) plane in Figs. 5.2 (a-c) for γ= 0°, 30° and 60°, respectively. The two diabatic electronic states are

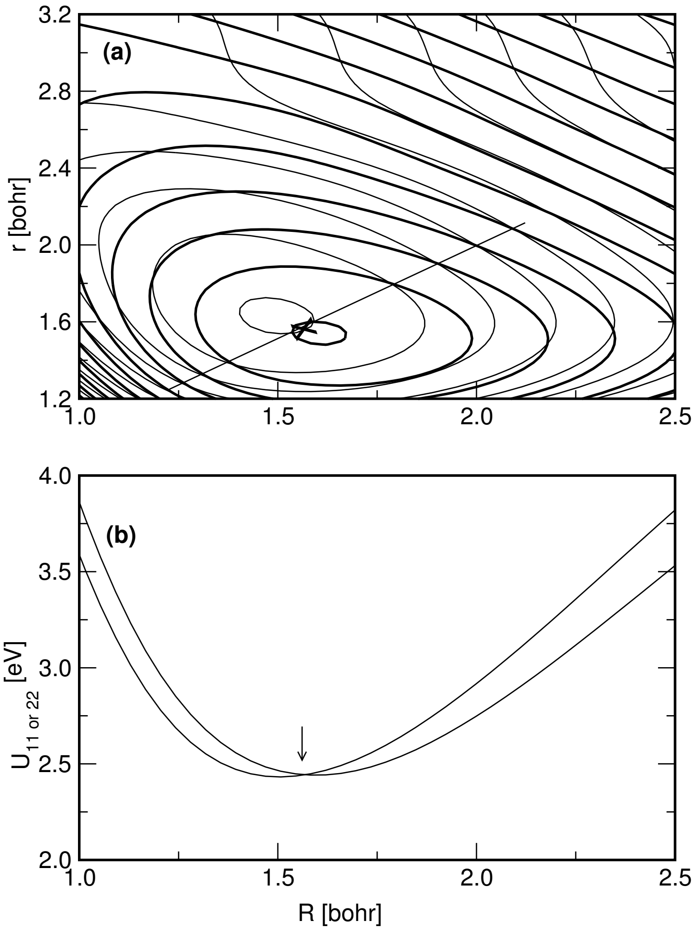

Figure 5.1: (a) Contours of the potential energies (eV) of the two diabatic components of the 3p (E') Rydberg electronic manifold of H_3 plotted in the (R, r) plane for $\gamma{=}\pi/2$. The lowest energy contour for both the states occurs at 2.45 eV and the spacing between the successive lines is 0.3 eV. The energy is measured relative to the three-body dissociation (H + H + H) limit. The straight line in the figure indicates the seam of CIs (occurring for $R = r$ between these two component states). The location of the energetic minimum on this seam is shown by the cross. (b) Potential energy cuts of the above two diabatic electronic states along R through the minimum of the seam of CIs. The minimum of the seam is indicated by an arrow and the minimum energy amounts to 2.43 eV.

indicated by two different line types in the figure.

It can be seen from the figures that the interpolated diabatic surfaces represent quite well the raw data, and are very smooth. The coupling surfaces of the above two diabatic surfaces are shown as contour line diagrams in the (R, r) plane in Figs. 5.3 (a-c) for $\gamma = 0^\circ$, 30° and 60°, respectively. The raw data and the corresponding interpolated ones are shown in the left and right column of the figure, respectively. A smooth behavior of the coupling surfaces is also apparent from the figure. It is to be noted that the coupling energy is exactly zero for the C_{2v} arrangements of the nuclei. The magnitude of the coupling potential becomes maximum at $\gamma = 0$ or π. Typically for the 3p (E') electronic state the maximum value is $\sim$ 0.78 eV, occurring for $R \sim 3.43\ a_0$, $r \sim 5.04\ a_0$ and $\gamma \sim 0$ or π.

The two component diabatic potential energy surfaces of the 3d (E'') Rydberg electronic manifold of H_3 are plotted in the (R, r) plane for $\gamma = \pi\ /2$ and are shown in Fig 5.4 (a). It can be seen that the topography of these two diabatic states is very similar and they remain energetically very close even for geometries far away from the D_{3h} configurations. This indicates that the JT interaction in the 3d (E'') electronic manifold is weaker than that in the 3p (E') electronic manifold.

The seam of CIs in the 3d (E'') electronic manifold is indicated by the straight line in Fig. 5.4 (a). The energetic minimum on this seam is marked by the cross on the diagram. This minimum occurs at $R = 1.52\ a_0$, $r = 1.52\ a_0$ and $\gamma = \pi/2$. The cuts of the above two diabatic surfaces through this minimum along R is shown in panel b. The minimum is more clearly shown by an arrow in the diagram and the energy at this minimum is $\sim$ 2.87 eV relative to the H + H + H dissociation limit. The maximum magnitude of the coupling potential in this case is 0.31 eV. We note that the coupling potential has a maximum value $\sim$

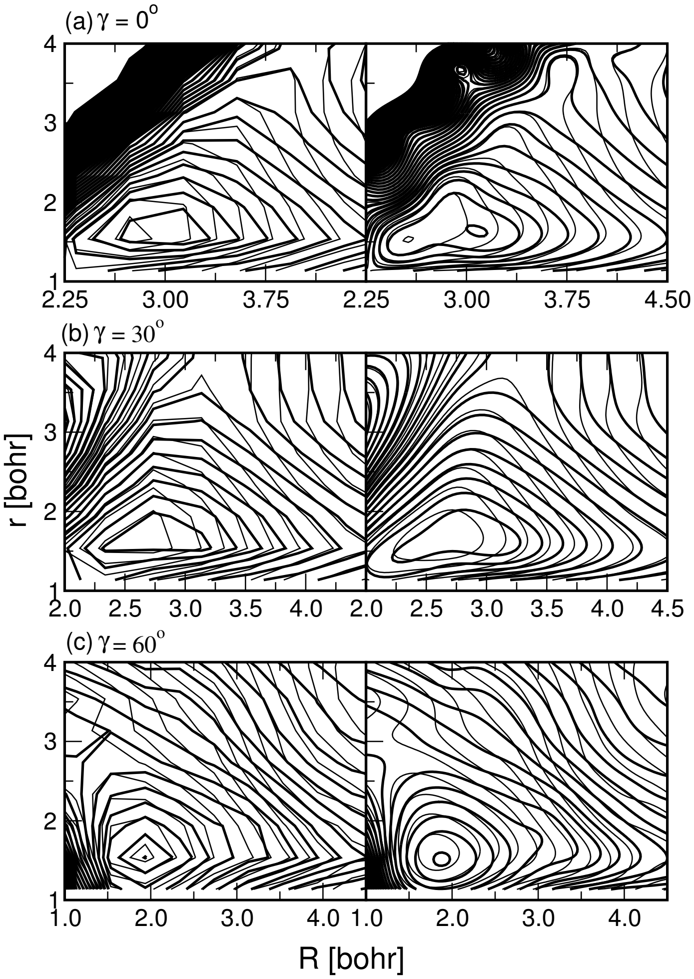

Figure 5.2: Contours of the diabatic potential energies of the 3p (E') Rydberg electronic manifold of H_3 plotted in the (R, r) plane for γ=0°, 30° and 60° in panel a,b and c, respectively. The diabatic surfaces are obtained from the computed *ab initio* adiabatic potential energy data (see text in Sec. II) and the corresponding interpolated ones are shown in the left and right columns of the figure, respectively.

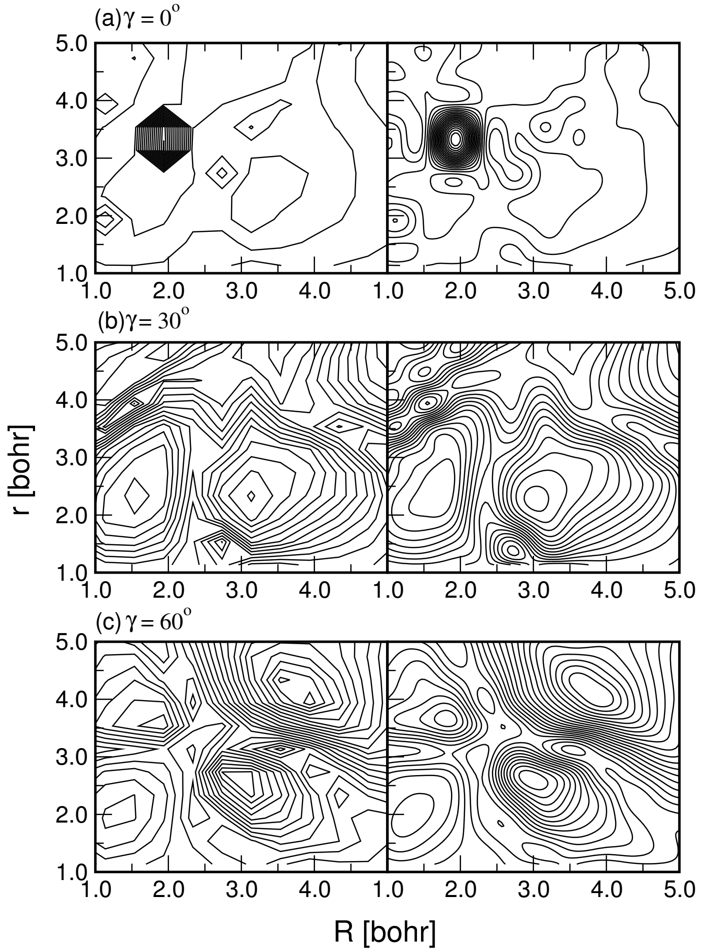

Figure 5.3: The coupling surfaces of the two diabatic PESs of Fig. 5.2 obtained from the computed *ab initio* data and interpolated using a three-dimensional spline. The contour line diagrams are plotted in the (R, r) plane for γ=0° (panel a), 30° (panel b) and 60° (panel c).

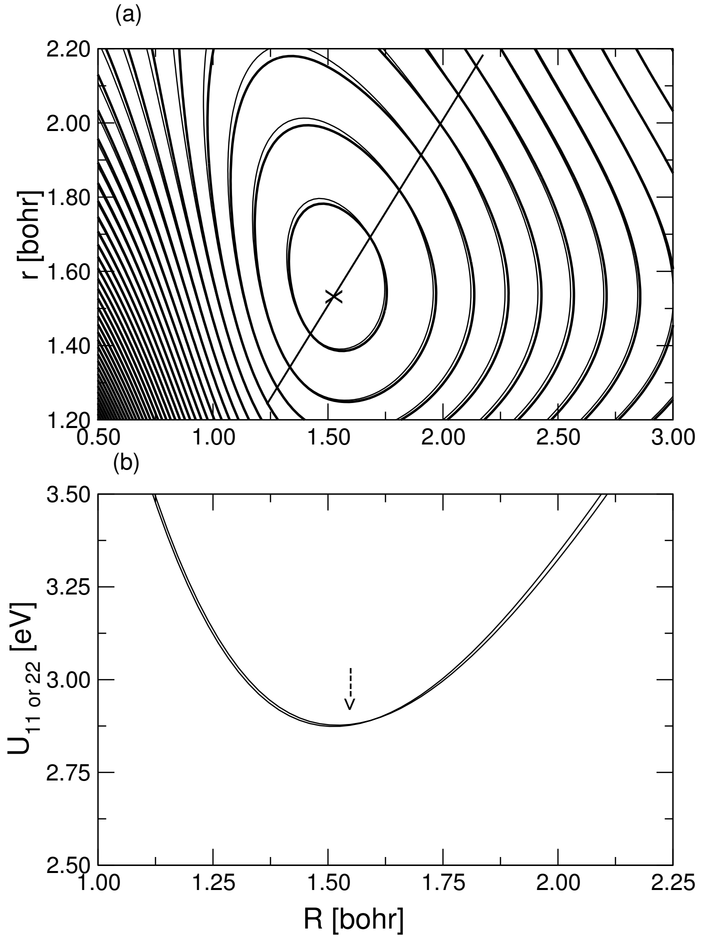

Figure 5.4: Same as in Fig. 5.1, for the 3d (E'') Rydberg electronic states of H_3. (a) The lowest energy contours in panel a in this case occurs at ∼ 2.88 eV and the spacing between the successive contour lines is 0.3 eV. The energy is measured relative to the three-body (H + H + H) dissociation limit. (b) The minimum of the seam of CIs is indicated by the arrow and the energy at this minimum amounts to ∼ 2.87 eV.

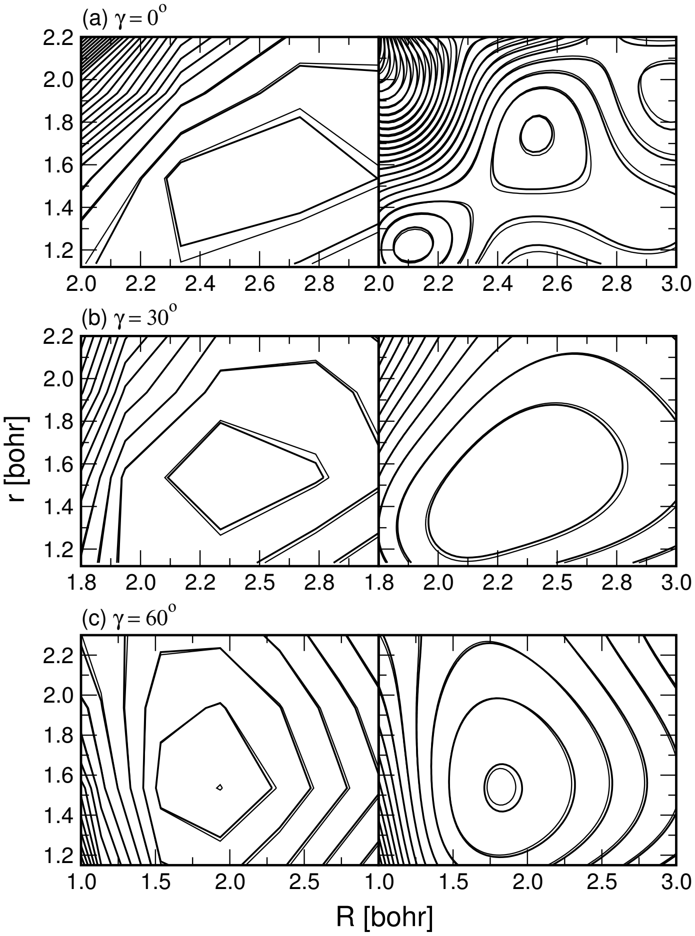

Figure 5.5: Same as in Fig. 5.2, for the 3d (E'') Rydberg electronic state of H_3.

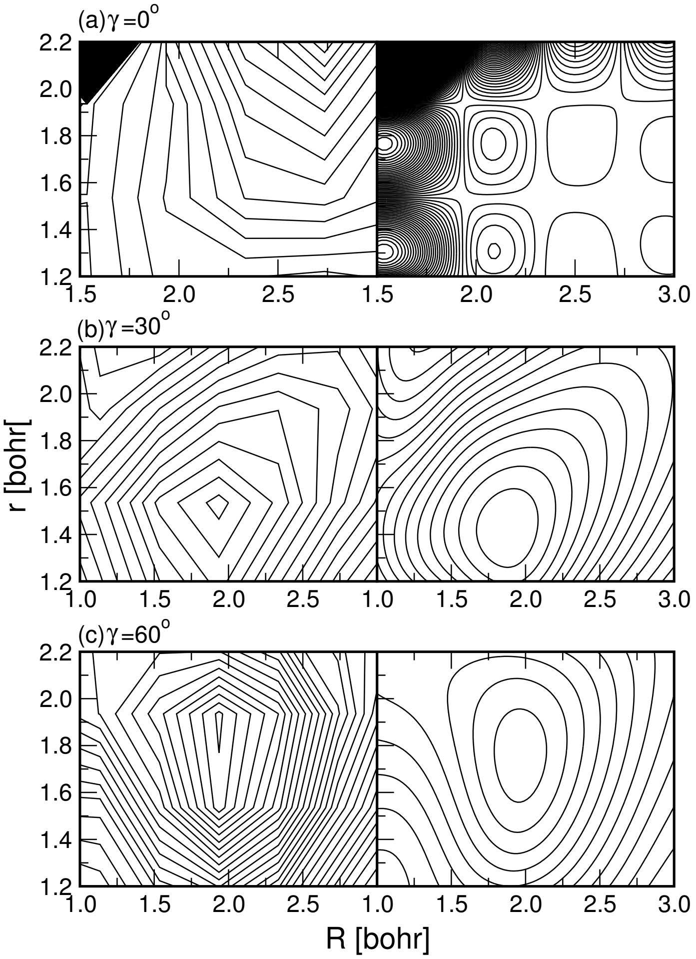

Figure 5.6: Same as in Fig. 5.3, for the 3d (E'') Rydberg electronic state of H_3.

3.25 eV for the 2p (E') ground electronic manifold of H_3. Therefore, it appears that the JT effects are much weaker in the Rydberg electronic states compared to those in the ground electronic manifold.

In order to show the quality of the numerical interpolations, we show in Figs. 5.5 (a-c) the cuts of the component diabatic states of the 3d (E'') electronic manifold in the (R, r) plane and for $\gamma = 0°$, $30°$ and $60°$, respectively. The coupling potentials of these two states are shown in Figs. 5.6 (a-c) for $\gamma = 0°$, $30°$ and $60°$, respectively. The diabatic energies and the coupling potentials derived from the computed *ab initio* adiabatic potential energies are shown in the left and the corresponding interpolated surfaces are shown in the right columns of Fig. 5.5 and Fig. 5.6. A smooth behavior of the diabatic surfaces and their coupling surfaces is also apparent in this case.

5.3 Theoretical framework to treat the nuclear dynamics

The nuclear dynamics in the degenerate 3p (E') and 3d (E'') Rydberg electronic states of H_3 is expected to be influenced by the low-lying CIs discussed above. For propagation of wave packets in these electronic states, we resort to the diabatic electronic basis as discussed in chapter 2. Spectral quantization algorithm with a GWP as discussed in chapter 4 has been employed to calculate the vibronic spectra. All the vibronic energy levels of the system can be obtained with appreciable intensities by suitably varying the initial location and the width parameters of this GWP. The initial parameters and the average energies of the GWPs used in the present calculations are given in Table 5.1 (for the 3p (E') electronic manifold) and Table 5.2 (for the 3d (E'') electronic manifold).

A second order split-operator scheme in conjunction with FFT and DVR methods is utilized to propagate the WPs. In each calculation the WP is evolved for a total time of 2.2 ps with a step length of Δt = 0.135 fs (3p (E') electronic manifold) and 550 fs with a step length of Δt = 0.135 fs (3d (E'') electronic manifold). The fast moving components of the WP reaching the grid edges are absorbed by activating a sin-type masking function [149] at $R_{mask} = 4.15$ a_0, $r_{mask} = 4.13$ a_0 in case of the 3p (E') electronic manifold and at $R_{mask} = 2.72$ a_0, $r_{mask} = 2.23$ a_0 in case of the 3d (E'') electronic manifold, respectively. The convergence of the calculations is explicitly checked by varying the numerical grid parameters stated above.

5.4 Results and discussion

The focus of the present work is to investigate the nonadiabatic coupling effects on the WP dynamics of H_3 near the CI of its 3p (E') and 3d (E'') Rydberg electronic states. This is motivated by our further plan to examine the DR process of Rydberg excited H_3. In the coupled state calculations the WP is initially prepared on the adiabatic electronic state and then transformed to the diabatic electronic basis for the propagation and final analysis. Companion calculations are carried out for the uncoupled adiabatic electronic states in order to clearly reveal the impact of the ($E\otimes e$)-JT CIs on the vibronic structure of these degenerate Rydberg electronic states. Different initial locations of the GWP on the potential energy surface yield same eigenvalue spectra. However, the intensity of the peaks differs in different spectra. Therefore, by varying the initial location of the GWP (cf., Tables 5.1 & 5.2) we are able to map out all the low-lying energy levels of the 3p (E') and 3d (E'') electronic states with appreciable intensities. In the following, we show and discuss the results obtained with only one location of the GWP in each case.

5.4.1 Vibronic energy levels of the 3p (E') Rydberg electronic manifold

The pseudospectrum of the uncoupled lower (V_-) adiabatic sheet of the 3p (E') electronic manifold of H_3 obtained with the initial GWP No. 3 (cf. Table 5.1) is shown in Fig. 5.7 (a). The peaks in the spectrum correspond to the bound vibrational energy levels of V_-. The energy is measured relative to the three-body dissociation (H + H + H) limit of 1.5 E_h. The energy eigenvalues and the assignments of the low-lying vibrational levels of V_- are given in Table 5.3 and are discussed below. The commonality of energy eigenvalues in various spectra obtained with different initial location of the GWP is explicitly checked. The pseudospectrum of V_- obtained with the GWP No. 3, in the coupled state situation is shown in Fig. 5.7 (b). The discrete level structure of the uncoupled V_- (cf., Fig. 5.7 (a)) becomes somewhat diffuse in the coupled state situations. The peak origin in the latter spectrum (cf., Fig. 5.7 (b)) shifts by $\sim$ 0.04 eV to higher energy which is due to the GP effects arising from the sign change of the adiabatic electronic wave function while encircling the CI in a closed loop [174, 182]. The minimum of the seam of CIs in the 3p (E') electronic manifold occurs at $\sim$ 2.43 eV. It can be seen that the 0-0 line in both the spectra in Fig. 5.7 appears above this energy. The energy eigenvalues of some of the distinct peaks in Fig. 5.7 (b) are also given in Table 5.3. It can be seen that the line density in the coupled state spectrum increases when compared to the uncoupled one. This increase is due to the nonadiabatic effects associated with the JT CIs in the 3p (E') electronic manifold [12]. The vibrational levels of the uncoupled V_- in Fig. 5.7 (a) are

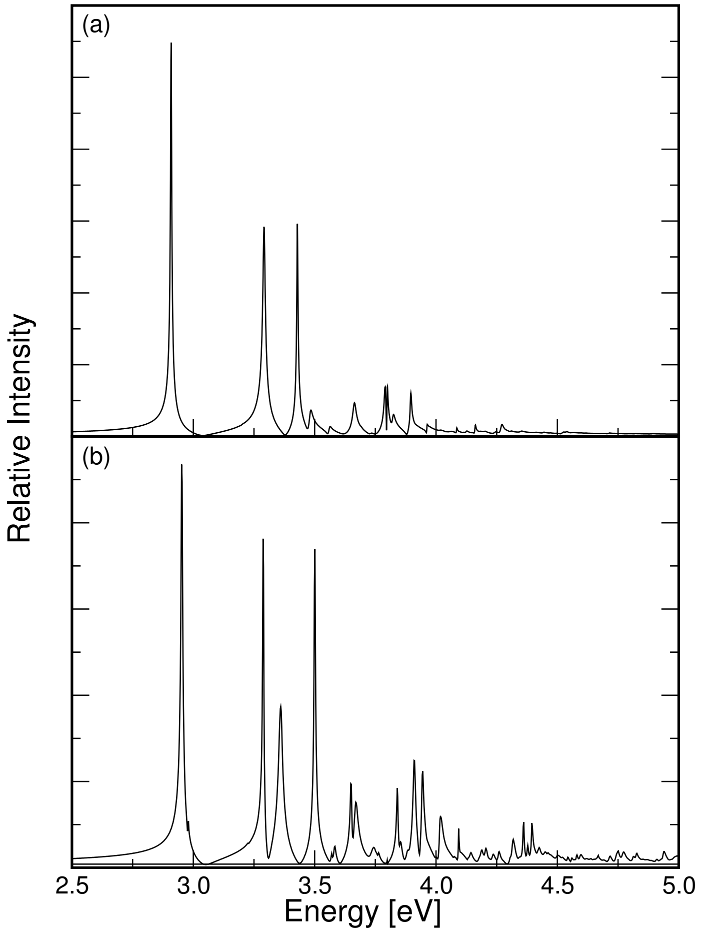

Figure 5.7: Pseudospectrum of the lower adiabatic sheet (V_{-}) of the 3p (E') Rydberg electronic manifold of H_3 in the uncoupled (panel a) and coupled state (panel b) situations. Intensity in arbitrary units is plotted as a function of the energy of the final vibronic states. The energy is measured relative to the three-body dissociation (H + H + H) limit.

assigned by computing their eigenfunctions, by projecting the time evolved WP onto the desired eigenstate (n) of energy E_n as given in Eq. (4.3).

The vibrational eigenfunctions of the uncoupled V_- surface are shown in Figs. 5.8 (a-h). Probability density ($|\psi_n(E)|^2$) contours of the eigenfunctions are plotted in the (R, r) plane (panels in the left column) and (γ, R) plane (panels in the right column). The probability density is averaged over γ in the former case and over r in the latter case. The eigenfunctions are assigned in terms of the number of nodes, n_R, n_r and n_γ along R, r and γ, respectively. According to this prescription the eigenfunction in Fig. 8 (a) would correspond to a (0,0,0) level. This is the ground vibrational level of the uncoupled V_- surface. The eigenfunction in Fig. 5.8 (b) represents the (0,1,0) level and that in Fig. 5.8 (c) the (0,0,2) level. The assignments of all the eigenfunctions in Figs. 5.8 (a-h) are given in Table 5.3. Even quantum excitation along the angle γ is seen in the eigenfunctions. In our previous work on the 2p (E') ground electronic state of H_3, we identified the eigenfunctions in terms of the progression along the breathing and bending vibrational modes [12]. These actually represent suitable linear combinations of the motions in Jacobi coordinates. Excitation along the breathing mode corresponds to a nodal progression along the D_{3h} symmetric stretch line ($R = r$). A nodal progression orthogonal to this line corresponds to the excitation along the bending mode. It is difficult to unambiguously assign the eigenfunctions in Fig. 8 according to this prescription due to their complex nodal pattern, however, the following qualitative estimates can be made. The eigenfunction in Fig. 5.8 (b) corresponds to one quantum excitation along the degenerate bending vibrational mode. Therefore, one vibrational quantum of this mode is ~ 0.38 eV in the lower adiabatic sheet of the 3p (E') electronic manifold. Similarly, the eigenfunction in Fig. 5.8 (f) has two quanta along this mode in addition to two quanta along γ.

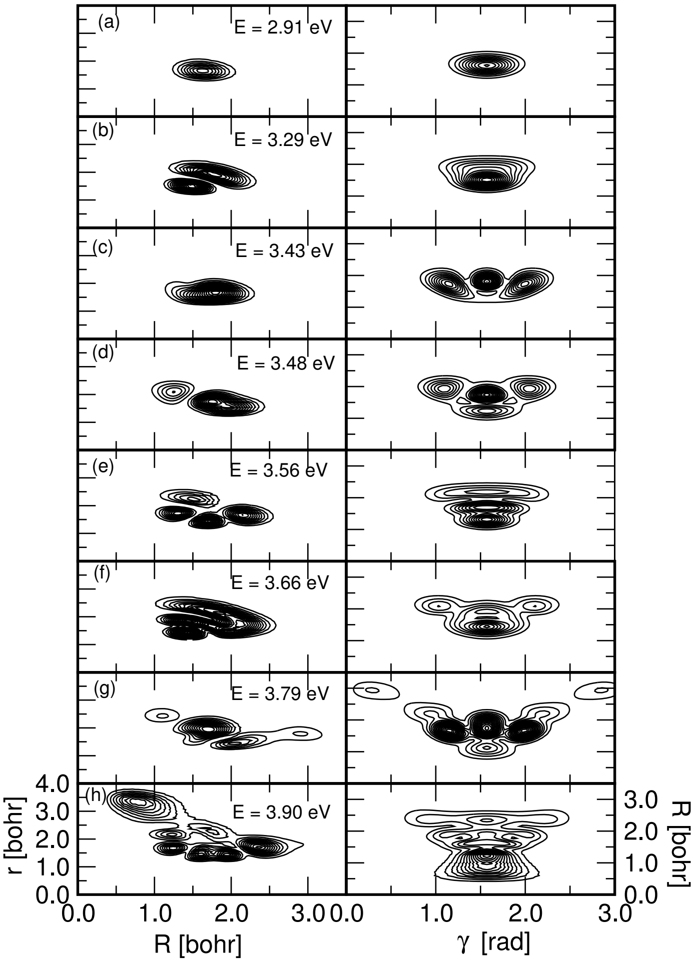

Figure 5.8: Probability density ($|\psi_n(E)|^2$) contours of the bound-state eigenfunctions of the lower adiabatic sheet (V_-) of the 3p (E') Rydberg electronic manifold of H_3, plotted in the (R, r) plane averaged over γ (left column) and (γ, R) plane averaged over r (right column). The energy eigenvalues are also indicated in the panels.

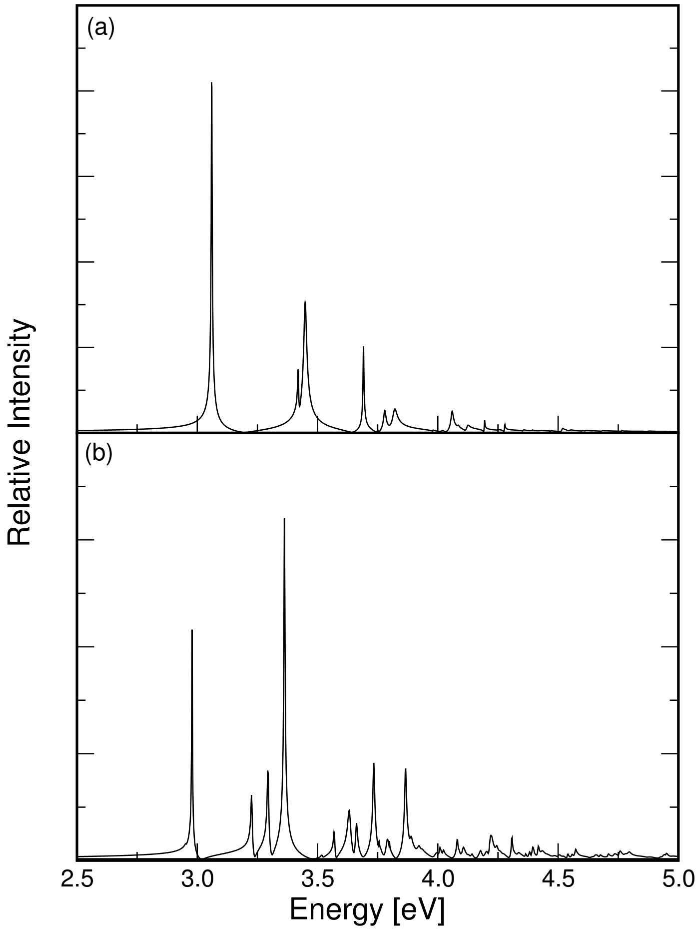

Figure 5.9: Same as in Fig. 5.7, for the uncoupled (panel a) and coupled (panel b) upper adiabatic sheet (V_+), of the 3p (E') electronic manifold of H_3.

The eigenfunction in Fig. 5.8 (e) corresponds to one quantum excitation along the breathing and one quantum along the degenerate bending vibrational mode. Therefore, the vibrational quantum along the breathing vibrational mode is $\sim$ 0.27 eV.

The pseudospectra of the upper adiabatic sheet, V_+, of the 3p (E') electronic manifold in the uncoupled and coupled state situations obtained with the initial GWP No. 3 (cf. Table 5.1) are shown in Figs. 5.9 (a-b), respectively. The band origin in the coupled state results shifts by ~ 0.08 eV to the lower energy. The width of the peaks in the two spectra essentially remains the same. The line density in the coupled state spectrum is higher than the uncoupled one. As mentioned above the additional peaks originate from the nonadiabatic interactions in the coupled state situation. The energy eigenvalues of some of the low-lying vibronic levels of V_+ are given in Table 5.3. The eigenfunctions of the vibrational levels of the uncoupled V_+ surface are shown in Figs. 5.10 (a-g). The probability density ($|\psi_n(E)|^2$) averaged over either γ or r are plotted as contour line diagrams in the (R, r) (panels in the left column) and (γ, r) plane (panels in the right column), respectively. The eigenfunctions are assigned in terms of (n_R, n_r, n_γ) specifications (as discussed above) and are included in Table 5.3. In this case also the eigenfunctions show even quanta excitation along the angle γ. The eigenfunction in Fig. 5.10 (c) exhibits one quantum excitation along the breathing mode and two quanta excitation along γ. The eigenfunction in Fig. 5.10 (e) on the other hand reveals one quantum excitation along the bending mode and two quanta excitation along γ. Therefore, roughly each quantum along this degenerate vibrational mode amounts to ~ 0.57 eV.

To this end we devote some space to further discuss the coupled state results shown in Figs. 5.7 (b) and 5.9(b). These two spectra are obtained with the same GWP No. 3 (cf. Table 5.1) evolving on the same final electronic manifold. However, the differences seen in the two spectra arise due to a difference in the initial location of the GWP. In the former case it is located on V_- and in the latter case it is on V_+. Therefore, the initial location of the WP represents different admixture of the two component diabatic electronic states U_{11} and U_{22}. The energy eigenvalues of the peak maximum of the coupled state spectra are also given in Table 5.3. It can be seen that the peaks in both the coupled state spectra

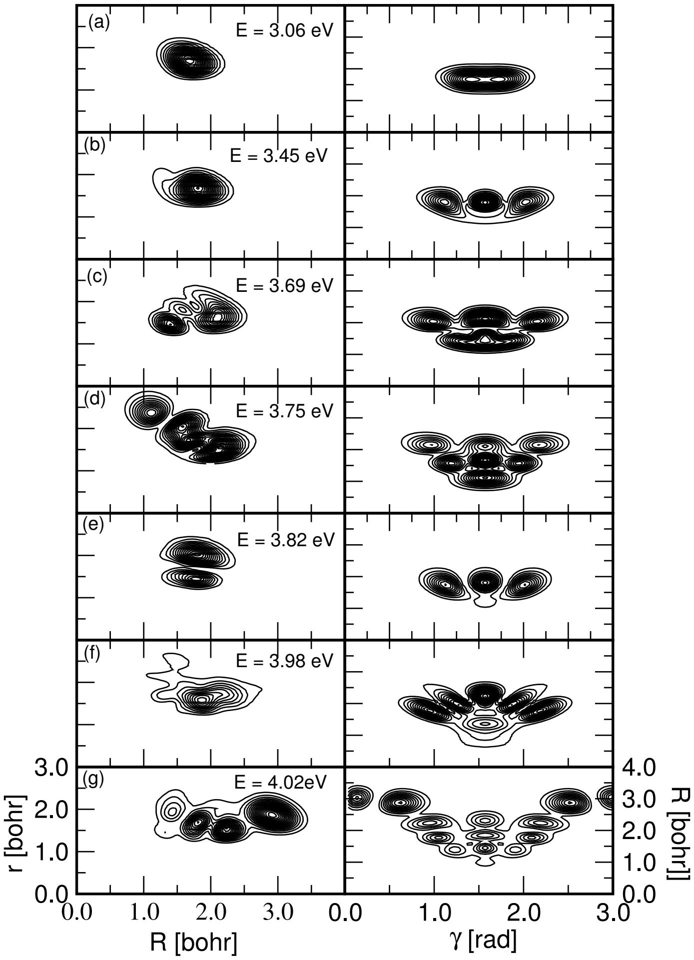

Figure 5.10: Same as in Fig. 5.8, for the vibrational levels of the upper adiabatic sheet (V_+) of the 3p (E') Rydberg electronic manifold of H_3.

appear at the same energy. However, due to two different locations of the initial WP the intensity of the peaks differs in two spectra. For example, the line at 2.95 eV gets more intensity and the line at 2.98 eV appears as a kink in Fig. 5.7 (b), whereas the opposite trend can be observed in Fig. 5.9 (b). As expected, the 0-0 line lies almost half-way between the 0-0 lines of the two uncoupled state spectra (cf. Table 5.3). The additional peaks in the coupled state spectrum result from the nonadiabatic interactions between the JT split potential energy surfaces. The shift in energy of the peaks between the uncoupled and coupled state spectra is quite small. This reflects that the JT coupling in this Rydberg electronic state is rather weak compared to the far stronger coupling effects observed in the 2p (E') ground electronic state of H_3 [96, 174, 174].

5.4.2 Vibronic energy levels of the 3d (E'') Rydberg electronic manifold

It can be seen from Figs. 5.4 and 5.5 that the two components of the 3d (E'') electronic manifold have almost identical topography. The adiabatic and the diabatic surfaces nearly coincide in this case. The vibronic structures of both the adiabatic surfaces are found to be very similar and we show only one of them below. In Figs. 5.11 (a-b) the vibronic structure of the upper adiabatic (V_+) state of the 3d (E'') electronic manifold in the uncoupled (panel a) and coupled (panel b) state situations is shown. These pseudospectra are calculated using the initial GWP No. 2 (cf. Table 5.2). A close look at the spectra in panels a and b reveals that nonadiabatic interactions cause somewhat broadening of the coupled state spectrum (panel b) at high energies. Analogous to the 3p (E') spectra, in this case also, the zero point vibrational level appears above the minimum of the seam of CIs at ~ 2.87 eV. The individual peak positions remain identical in both

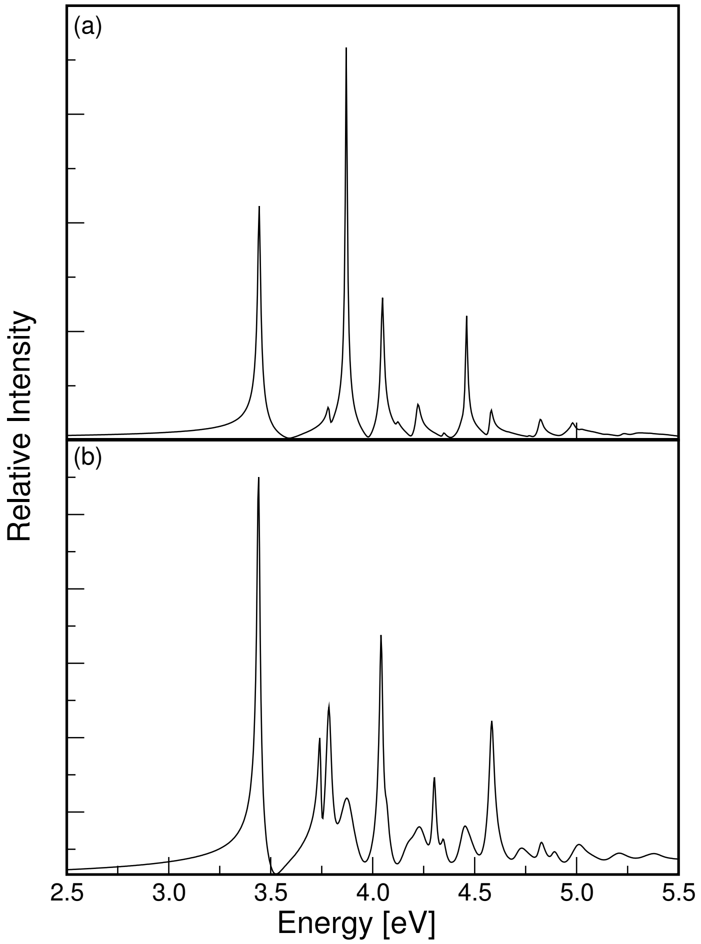

Figure 5.11: Same as in Fig. 5.7, for the uncoupled (panel a) and coupled (panel b) upper adiabatic sheet, V_+, of the 3d (E'') electronic manifold.

cases (cf. Table 5.3), however, additional peaks appear due to the nonadiabatic interactions in the coupled state situation [12]. The energy eigenvalues of both the adiabatic sheets of the 3d (E'') electronic manifold in the uncoupled and coupled state situations are given in Table 5.3.

The eigenfunctions of the low-lying vibrational levels of the uncoupled upper adiabatic sheet of the 3d (E'') electronic manifold are shown in Figs. 5.12 (a-g). They are also assigned in terms of the (n_R, n_r, n_γ) specifications as discussed above and the assignments are given in Table 5.3. The vibrational levels of the uncoupled lower adiabatic sheet reveal identical nodal progressions and we do not show them here. The eigenfunction in Fig. 5.12 (b) seems to reveal one quantum excitation along the degenerate bending vibrational mode. The quantum of this bending vibration therefore amounts to $\sim$ 0.43 eV, which can be compared with a value $\sim$ 0.31 eV derived from the available experimental results [177–179]. The eigenfunction in Fig. 5.12 (d) corresponds to one quantum excitation along both the breathing and bending vibrational modes. From the data given in Table 5.3 one can see that one quantum of the breathing vibrational mode amounts to $\sim$ 0.35 eV. This can be compared with a value of $\sim$ 0.39 eV estimated from the available experimental data [177–179].

More recent and improved electronic structure calculations [181] indicate a lowering of the absolute energies of the Rydberg electronic states. At the equilibrium geometry of H_3^+, the energy of the 3p (E') state is found to be $\sim$ 0.17 eV and that of 3d (E'') state found to be $\sim$ 0.12 eV lower than the results discussed above. In view of these corrections the energy of the minimum of the seam of intersections occurs at $\sim$ 2.26 eV and $\sim$ 2.76 eV for the 3p (E') and 3d (E'') electronic states, respectively. The energies of the first few vibronic levels of 3p (E') and the 3d (E'') electronic states along with the available experimental results [177–180] are given in table 5.4. The theoretical results in the latter are obtained by incorporating the above energy correction to the energies of table 5.3. It can be seen that the low-lying vibronic levels of both the electronic states are in fairly good agreement with the experimental results. A more rigorous comparison with the available experimental data [177–180] necessitates the energy levels to be calculated including the rotation, i.e., for the total angular momentum $\mathbf{J} \neq 0$. Such calculations are presently being taken up.

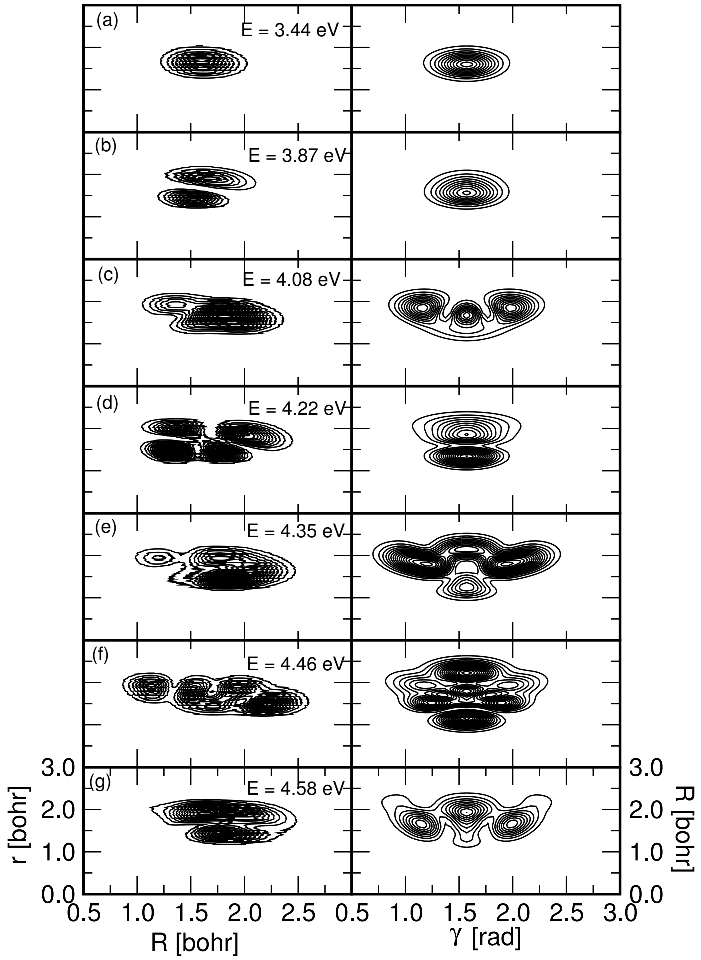

Figure 5.12: Same as in Fig. 5.8, for the vibrational levels of the uncoupled upper adiabatic sheet (V_+) of the 3d (E'') electronic manifold.

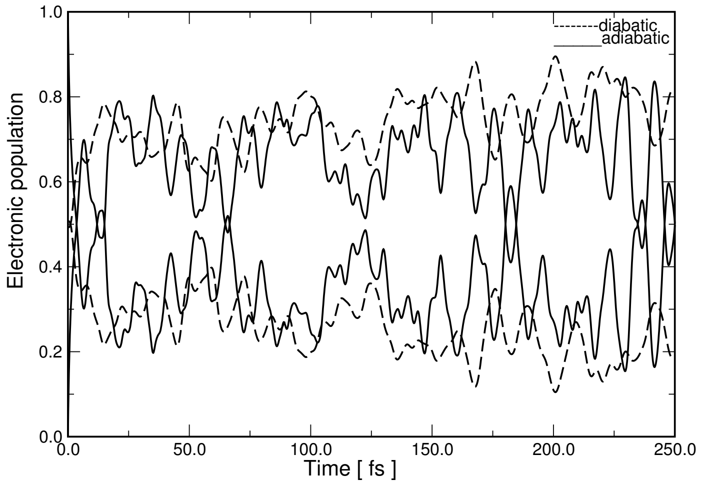

Figure 5.13: Time-dependence of the adiabatic (solid lines) and the diabatic (dashed lines) electronic populations in the coupled state dynamics of the 3p (E') Rydberg electronic manifold of H_3. The GWP No. 3 is initially located on V_+. The upper and the lower solid curves represent the population of V_+ and V_-, respectively.

5.4.3 Time-dependent wave packet dynamics

We now focus on the internal conversion dynamics of the 3p (E') and 3d (E'') Rydberg electronic manifold of H_3 driven by the JT CIs in the respective states. The relevant quantity reported here is the time-dependence of the diabatic and adiabatic electronic populations of these states.

In Fig. 5.13, we show the time-dependence of the adiabatic and diabatic electronic populations in the coupled state dynamics of the 3p (E') electronic manifold. These populations and all later ones shown below represent the fractional populations. The initial GWP No. 3 (cf. Table 5.1) is located on the upper adiabatic sheet V_+. The nuclear dynamics in this sheet is expected to be strongly affected by the nonadiabatic interactions. This is because the minimum of the seam of CIs coincides with the energetic minimum of this state. The adiabatic and diabatic electronic populations in Fig. 5.13 are indicated by the solid and dashed lines, respectively. The upper solid curve indicates the population of V_+ and the lower one that of V_-. Since the WP is initially located on V_+, the population of this state is 1.0 at t = 0. The population of this state sharply decreases to ~ 0.5 within 3.58 fs and to ~ 0.3 within ~ 6.5 fs and then fluctuates statistically around a value of ~ 0.3 at longer times. Therefore, within ~ 3.58 fs the WP reaches the CI, which is also marked by the growth of the population of V_- (upper solid line) within this period. The latter fluctuates around a value of $\sim$ of 0.7 at longer times. This indicates that on the average only 70 % of the WP reaches the lower adiabatic sheet. The maximum population exchange occurs at ~ 30 fs. Within this time ~ 80 % of the WP moves to V_-. The initial location of the WP on V_+ corresponds to an admixture of both the component diabatic states. Therefore, one finds a 49 % (51 %) population on U_{11} (U_{22}) at t = 0. The lower adiabatic surface exhibits a "Mexican hat" type of topography and has a cusp like behavior at the intersection seam. The resulting anharmonicity of this surface apparently causes most of the damping of the oscillations in the diabatic population [180] . Similar electronic population dynamics is observed by preparing the initial GWP on the lower adiabatic sheet (V_-). In this case on the average 30 % of the lower adiabatic population moves to the upper adiabatic sheet.

In order to better understand the above population dynamics we present snapshots of the WP evolving on the coupled 3p (E') electronic manifold at different times in Fig. 5.14. The probability density of the WP averaged over the angular coordinate is superimposed on the potential energy contours for $\gamma = \pi/2$ in the (R, r) plane. The seam of CIs between these two electronic states is also indicated in the first panel of the left column. It can be seen that the WP at t = 0 is generated very near to this seam. Because of this a considerable portion (~ 65

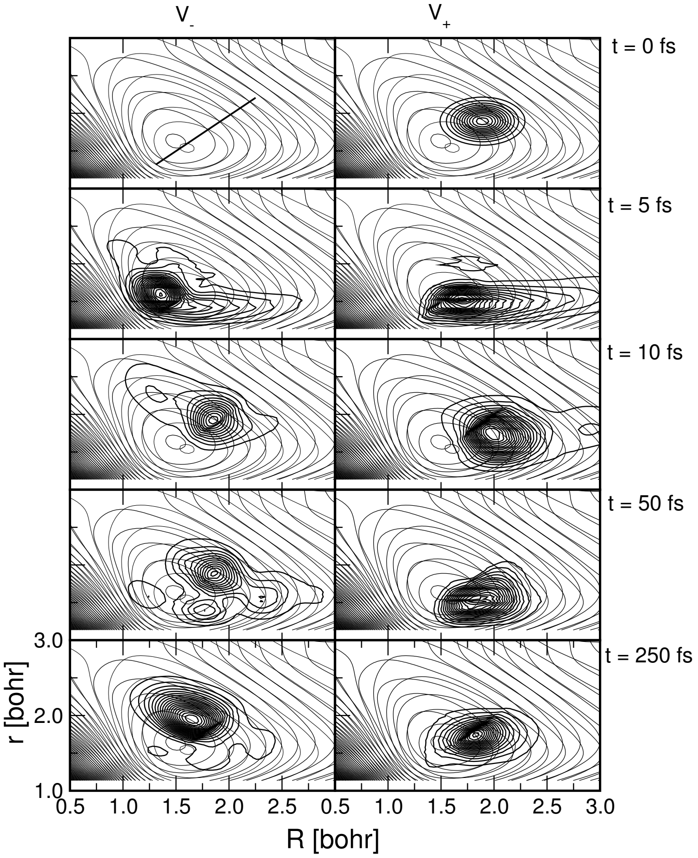

Figure 5.14: Probability density ($|\psi|^2$) of the adiabatic wave packet averaged over the Jacobi angle γ and superimposed on the potential energy contours in the (R, r) plane for $\gamma = \pi/2$. The WP components on the V_- and V_+ at a given time are shown in the left and right panels, respectively. The seam of CIs between these states is shown by a solid line in the first panel in the left column of the figure.

%) of the WP moves to the lower adiabatic state within $\sim$ 5 fs. (Since the WP is initially located on V_+, the population of this state is 1.0 and that of V_- is 0.0 at t = 0). Within $\sim$ 5 fs significant portion of the WP approaches the CIs and moves towards the minimum of the lower adiabatic sheet. The WP on V_- then moves towards the intersection seam and a portion of it moves back to V_+, which is marked by a rise in the population of the latter to $\sim$ 47 % (cf. Fig. 5.13) at $\sim$ 50 fs. The WP moves back and forth between the two states in time and the population exchange through the intersection seam continues. At longer times e.g., $\sim$ 250 fs, $\sim$ 76 % of the WP moves to V_-.

The electronic population dynamics in the coupled 3d (E'') electronic manifold exhibits very similar pattern as that in the 3p (E') electronic manifold. In this case the time-dependence of the populations reveal a more regular pattern. The time-dependence of the adiabatic and diabatic electronic populations obtained by locating the initial GWP No. 2 (cf. Table 5.2) on the upper adiabatic sheet (V_+) of the 3d (E'') coupled electronic manifold is shown in Fig. 5.15.

As before the solid and dashed lines represent the adiabatic and the diabatic electronic populations, respectively. The time-dependence of the adiabatic electronic population exhibit a very regular pattern and the recurrences therein are on the average $\sim$ 9 fs spaced in time. In this case on the average $\sim$ 50 % of the WP moves to the lower adiabatic sheet. The initial location of the WP in this case corresponds to 50 % (50 %) admixture of the two diabatic electronic states. Unlike in the 3p (E') electronic manifold (cf., Fig. 5.13) the diabatic electronic populations in this case reveal a very simple pattern. The oscillations seen in the adiabatic electronic populations are heavily suppressed in the corresponding diabatic ones.

The WP motion in the above coupled 3d (E'') electronic manifold is shown in

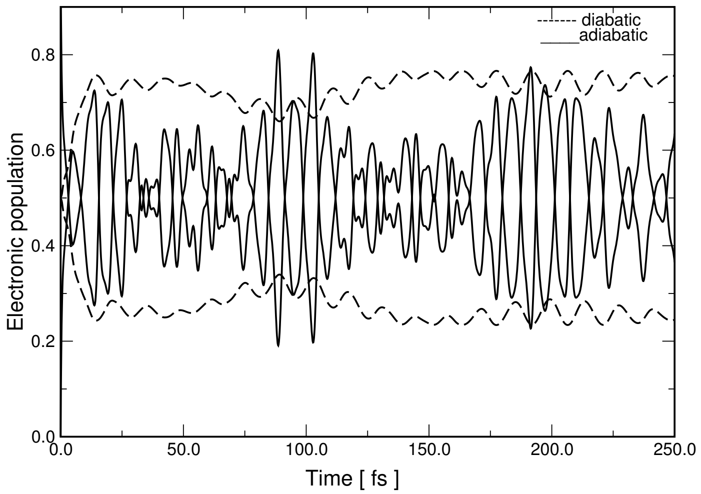

Figure 5.15: Same as in Fig. 5.13, for the time-dependence of adiabatic (solid lines) and the diabatic (dashed lines) electronic populations in the coupled state dynamics of the of 3d (E'') electronic manifold of H_3.

Fig. 5.16, at various times indicated in the diagram. The probability density of the two component adiabatic wave packets averaged over γ is plotted in the (R, r) plane and superimposed on the potential energy contours for $\gamma = \pi/2$. The seam of CIs is indicated by the solid line in the first panel in the left column. It can be seen that the WP is prepared close to this seam in this case also. Therefore, the WP is immediately perturbed by the strong nonadiabatic coupling and as a result $\sim$ 59 % of the WP moves to V_- at a very short time of $\sim$ 5 fs. Both the WP components move to the minimum of the respective surfaces and develop structures. The WPs move back and forth between the two states, which gives rise to quasiperiodic recurrences in the adiabatic electronic populations (cf., Fig. 5.15). On an average $\sim$ 50 % of the WP reaches the lower adiabatic state during the course of the entire dynamics.

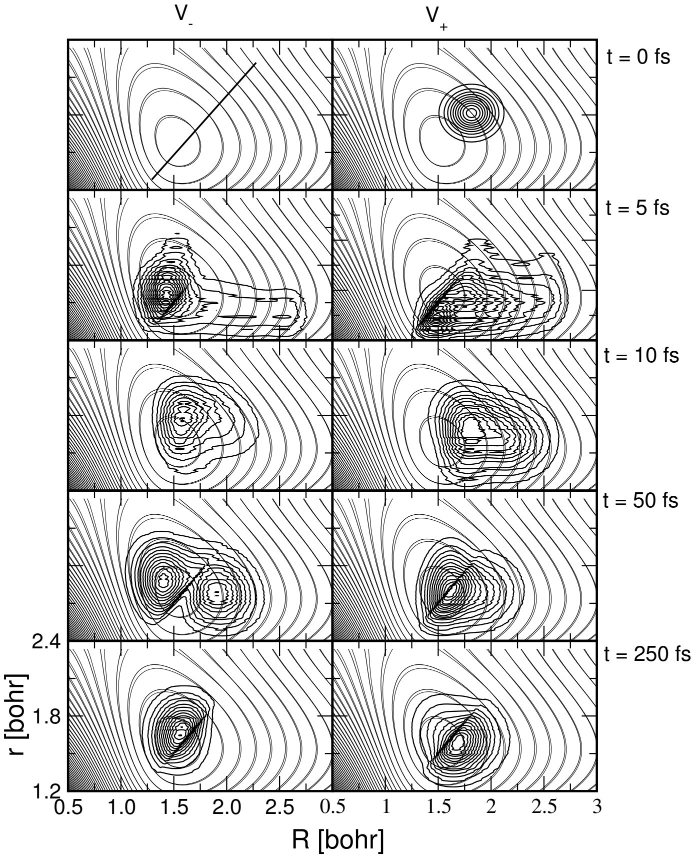

Figure 5.16: Same as in Fig. 5.14, for the 3d (E'') Rydberg electronic manifold of H_3.

5.5 Summary

We have presented a detailed account of the topography, spectroscopy and the time-dependent dynamics of the two important degenerate 3p (E') and 3d (E'') Rydberg electronic manifolds of H_3. The static aspects of these electronic states are discussed based on the *ab initio* adiabatic potential energy data. The adiabatic surfaces are diabatized and the JT CIs are established. The spectroscopy and the time-dependent dynamics are examined by propagating the WPs on the coupled manifolds of these electronic states.

Our findings reveal that the nonadiabatic coupling effects in these Rydberg electronic manifold of H_3 are much milder than those found in case of its 2p (E') ground electronic manifold. Comparing the two Rydberg electronic states, the nonadiabatic effects are slightly stronger in case of the 3p (E') electronic manifold. The strength of the coupling potential within each electronic manifold is proportional to the splitting of the adiabatic surfaces δ and a geometrical factor. In the case of a Rydberg series this splitting is proportional to n_{eff}^{-3}, where n_{eff} is the effective principal quantum number. With n_{eff} [2p (E')] $= 1.512$ and n_{eff} [3p (E')] $= 2.593$ [187], the coupling strength is expected to be about 5 times weaker for 3p (E'), assuming a constant JT splitting if expressed by effective quantum numbers. This however is only approximately true and the real ratio of the coupling strength is $\sim 1/8$. A similar explanation can be given for even weaker coupling strength for 3d (E'') electronic manifold.

The vibronic energy levels in both uncoupled and coupled state situations have been presented here and individual eigenstates of the uncoupled adiabatic electronic states were assigned. The results compare well with the available experimental data (cf. Table 5.4). The present work is motivated by recent experimental interest on the dissociative recombination process of H_3. Apparently

Table 5.1: Parameters for different choices of the initial Gaussian wave packet used for simulating nuclear dynamics in the 3p (E') Rydberg electronic manifold of H_3.

GWP	R_0 (a_0)	r_0 (a_0)	γ_0 (rad)	σ_R (a_0)	σ_r (a_0)	σ_γ (rad)	$\langle E\rangle$ (eV)
1	1.5823	1.5903	1.5708	0.25	0.20	0.15	3.0895
2	1.7882	1.7899	1.5708	0.25	0.20	0.15	3.1267
3	1.8912	1.8950	1.5708	0.25	0.20	0.15	3.4231
4	1.9868	2.0105	1.5708	0.25	0.20	0.15	3.6885
5	2.0823	2.0840	1.5708	0.25	0.20	0.15	3.9243
6	2.1779	2.1786	1.5708	0.25	0.20	0.15	4.2052

Table 5.2: Parameters for different choices of the initial Gaussian wave packet used for simulating nuclear dynamics in the 3d (E'') Rydberg electronic manifold of H_3.

GWP	R_0 (a_0)	r_0 (a_0)	γ_0 (rad)	σ_R (a_0)	σ_r (a_0)	σ_γ (rad)	$\langle E\rangle$ (eV)
1	1.6872	1.6876	1.5708	0.20	0.15	0.10	3.6068
2	1.8149	1.8145	1.5708	0.20	0.15	0.10	3.8071
3	1.9092	1.9095	1.5708	0.20	0.15	0.10	4.0789

the mechanism involved is much more complex and can not be satisfactorily explained by the currently available electronic structure data. An investigation of this complex mechanism and the analysis of the vibronic levels of the 3p (E') and 3d (E'') Rydberg electronic manifolds of H_3 including rotations are the two main tasks in the future and are presently in progress.

Table 5.3: Vibronic energy levels of the uncoupled and coupled lower (V_-) and upper (V_+) adiabatic electronic states of the 3p (E') and 3d (E'') Rydberg electronic manifolds of H_3. The assignments of the vibrational levels of the uncoupled states are also given (see text for details). A blank entry in the table implies that the corresponding quantity can not be given unambiguously.

3p (E′)						3d (E″)					
V_-			V_+			V_-			V_+		
Uncoupled		Coupled*	Uncoupled		Coupled*	Uncoupled		Coupled*	Uncoupled		Coupled*
	Energy	Assignment	Energy	Energy	Assignment	Energy	Energy	Assignment	Energy		
eV	(n_R, n_r, n_γ)	eV	eV	(n_R, n_r, n_γ)	eV	eV	(n_R, n_r, n_γ)	eV	eV	(n_R, n_r, n_γ)	eV
2.91	(0,0,0)	2.95	3.06	(0,0,0)	2.95	3.44	(0,0,0)	3.44	3.44	(0,0,0)	3.44
3.29	(0,1,0)	2.98	3.45	(0,0,2)	2.98	3.87	(0,1,0)	3.74	3.87	(0,1,0)	3.74
3.43	(0,0,2)	3.22	3.69	(1,-,2)	3.22	4.04	(0,0,2)	3.78	4.04	(0,0,2)	3.78
3.48	(1,0,2)	3.29	3.75	(2,0,2)	3.29	4.22	(1,1,0)	3.87	4.22	(1,1,0)	3.87
3.56	(1,1,0)	3.36	3.82	(0,1,2)	3.36	4.35	(1,0,2)	4.03	4.35	(1,0,2)	4.03
3.66	(0,2,2)	3.57	3.98	(0,0,4)	3.57	4.46	(3,0,2)	4.22	4.46	(3,0,2)	4.22
3.79	(1,1,2)	3.64	4.02	(3,0,2)	3.64	4.58	(0,1,2)	4.31	4.58	(0,1,2)	4.31
3.90	(2,2,0)	3.67	-	-	3.67	-	-	4.33	-	-	4.45
-	-	3.74	-	-	3.74	-	-	4.45	-	-	4.55
-	-	3.80	-	-	3.80	-	-	4.55	-	-	4.59
-	-	3.86	-	-	3.86	-	-	4.59	-	-	-
-	-	3.88	-	-	3.88	-	-	-	-	-	-
-	-	3.91	-	-	3.91	-	-	-	-	-	-
-	-	3.99	-	-	3.99	-	-	-	-	-	-
-	-	4.02	-	-	4.02	-	-	-	-	-	-
-	-	4.09	-	-	4.09	-	-	-	-	-	-
-	-	4.10	-	-	4.10	-	-	-	-	-	-

Table 5.4: The low-lying vibronic levels of the 3p (E') and 3d (E'') Rydberg electronic manifolds of H_3 along with the available experimental results [183–186]. The two numbers in the parentheses in the first column indicate the quantum numbers of the breathing and bending vibrational modes, respectively. The theoretical energy values are obtained from the coupled state energies of Table III with the corrections noted in the text at the end of the section IV B. A blank entry implies the corresponding value is not available.

Vibronic level	*Theory* (eV)	*Experiment.* (eV)
3p E$'$(0,0)	2.79	2.72
3p E$'$(1,0)	3.06	–
3p E$'$(0,1)	3.17	3.05
3d E$''$(0,0)	3.32	3.26
3d E$''$(1,0)	3.67	3.65
3d E$''$(0,1)	3.66	3.56

Finally a remark on the important role of the JT coupling in the dissociative recombination process seems to be useful here. Greene and coworkers [53] presented a model based on multichannel quantum defect theory which treats the capture of an electron into a whole Rydberg series, distinguishing direct (2p (E')) and indirect (higher Rydberg states) processes. The present study does not deal with the process of electron capture, but the predicted probability of population for the upper and lower sheet of 3p (E') (30 % : 70 %) may be relevant, under suitable circumstances, to the branching ratio of the H + H_2 and H + H + H channels.

Chapter 6

Future Directions

A theoretical account of the nonadiabatic reactive scattering dynamics of H + H_2 reaction and its isotopic variants with the aid of a TDWP approach is presented in this thesis. The nuclear dynamics is treated with a coupled electronic states of the system. The dynamical observables reported include the state-selected reaction probabilities, integral reaction cross sections and thermal rate constants. The reaction probabilities and integral reaction cross sections are calculated upto the three-body dissociation limit of H_3 ($\sim$ 4.75 eV). All the calculations are carried out with and without including the surface coupling in the dynamics to understand the importance of the nonadiabatic interactions on these observables. The difference between the reaction probability and integral reaction cross section data calculated with and without the surface coupling is small at low collision energies. At higher energies near and above the energetic minimum of the seam of CIs this difference becomes noticeable. However, as J increases this difference becomes negligible. The effect of reagent rotation and vibration on the dynamics of the H + H_2 reaction is studied when the reagent diatom, H_2 is in $(v = 0, j = 0 - 10)$ and $(v = 0 - 10, j = 0)$, respectively. Analysis of the reaction probability and integral reaction cross section data shows that the nonadiabatic effects are insignificant at small values of j and v, which become more pronounced with an increase of the latter quantities. Electronic nonadiabatic effects found to more important in the reaction dynamics of rotationally excited H_2. The thermal rate constants calculated and compare well with the available other theoretical and experimental results in the literature.

Quantum WP dynamical study of $N(^2D) + H_2$ reaction on a recently developed *ab initio* PES of NH_2 is studied in this thesis. Initial state-selected reaction probabilities, integral reaction cross sections and thermal rate constants are calculated and compare well with available other theoretical and experimental results. The reaction probabilities rise near threshold and then oscillate at higher energies for a particular value of J. These oscillations in the reaction probabilities are attributed to the large number of the quasibound vibrational levels supported by the ground PES of NH_2. The reaction cross section values increase with energy and then reach to a plateau at higher energies. The cross section values are found to increase with rotational excitation of the reagent, H_2. The results obtained support the expected insertion type of mechanism for this reaction. The vibrational levels supported by the deep well in the PES of this system are calculated and analyzed statistically.

The JT CIs in the 3p (E') and 3d (E'') Rydberg electronic states of H_3 is studied by calculating the vibronic energy spectrum of these electronic states with and without including surface coupling in the dynamics. The JT interactions in these electronic states are expected to be important in the dissociative recombination of H_3^+ ion. The JT conical interaction are found to be low in these electronic states as compared with degenerate ground electronic state, 2p (E') of H_3. The nonadiabatic interaction are more in 3p (E') electronic state as compared to 3d

(E'').

To this end we note that further studies on state-to-state dynamics of H + H_2 reaction by including the surface coupling explicitly in the dynamics is important. A detailed exploration of the GP effects on the H + H_2 reaction dynamics is necessary. Investigations of the coupling mechanism of Rydberg electronic states with its ground electronic state to shed light on the DR process of Rydberg excited H_3 is also important. Also study of the RT effects on the N (^2D) + H_2 reaction dynamics and an extension of the above techniques to other polyatomic reactions where surface coupling plays an important role in the dynamics will be valuable to arrive at a better understanding of the nonadiabatic chemical reaction dynamics.

Bibliography

[1] M. Born and R. Oppenheimer, Ann. Phys. **84**, 457 (1927).

[2] M. Born and K. Huang, in *The Dynamical Theory of Cryatal Lattices* (Oxford University Press, 1954).

[3] J. von Neumann and E. P. Wigner, Z. physik., **30**, 467 (1929).

[4] G. Herzberg, H. C. Longuet-Higgins, Disscuss. Faraday. Soc., **35**, 77 (1963).

[5] Chemical Physics **259**, 121-350, 2000 (special issue on conical intersections)

[6] W. Domcke, D. R. Yarkony, H. Köppel, Eds. *Conical Intersections: Electronic Structure, Dynamics and Spectroscopy*, (World Scientific, Singapore 2004).

[7] D. R. Yarkony, Rev. Mod. Phys. **68**, 985 (1996).

[8] H. Jahn and E. Teller, Proc. Roy. Soc. London, Ser. A. **161**, 220 (1937).

[9] I. B. Bersuker, *The Jahn - Teller Effect and Vibronic Interactions in Modern Chemistry* (Plenum Press, New York, 1984).

[10] R. Englman, *The Jahn - Teller Effect in Molecules and Crystals*, (Wiley, New York, 1972).

[11] I. B. Bersuker, Chem. Rev., **101**, 1067 (2001).

[12] H. Köppel, W. Domcke and L. S. Cederbaum, Adv. Chem. Phys., **57**, 59 (1984).

[13] M. Z. Zgierski and M. Pawlikowski, J. Chem. Phys., **70**, 3444 (1979).

[14] H. Köppel, L. S. Cederbaum and W. Domcke, J. Chem. Phys., **89**, 2023 (1988).

[15] H. Köppel, L. S. Cederbaum and W. Domcke, J. Chem. Phys., **111**, 10452 (1988).

[16] E. Renner, Z. Phys., **92**, 172 (1934).

[17] Ch. Jungen and A. Merer, Mol. Phys., **40**, 1 (1980).

[18] *Conical intersections in photochemistry, spectroscopy and chemical physics*, Chem. Phys., **259** (2000).

[19] T. F. O'Malley, Phys. Rev., **162**, 98 (1967).

[20] W. Lichten, Phys. Rev., **164**, 131 (1967).

[21] F. T. Smith, Phys. Rev., **179**, 111 (1969).

[22] T. Pacher, L. S. Cederbaum and H. Köppel, Adv. Chem. Phys., **84**, 293 (1993).

[23] A. Thiel and H. Köppel, J. Chem. Phys., **110**, 9371 (1999).

[24] H. Köppel, J. Gronki and S. Mahapatra, J. Chem. Phys., **115**, 23771 (2001).

[25] S. Mahapatra, H. Köppel and L. S. Cederbaum, J. Phys. Chem. A, **105**, 2321 (2001).

[26] F. Fernández-Alonso and R. N. Zare, Ann. Rev. Phys. Chem. **53**, 67 (2002).

[27] F. J. Aoiz, L. Bañares and V. J. Herrero, Int. Rev. Phys. Chem. **24**, 119 (2005).

[28] F. London, *Z. Elektrochem*, **35**, 552 (1929).

[29] D. G. Truhlar and R. E. Wyatt, Annu. Rev. Phys. Chem., **27**, 1 (1976).

[30] G. C. Schatz, Annu. Rev. Phys. Chem., **39**, 317 (1988).

[31] D. E. Manolopoulos and R. E. Wyatt, J. Chem. Phys. **92**, 810 (1990).

[32] J. Chang and N. J. Brown, J. Chem. Phys. **103**, 4097 (1995).

[33] D. M. Charutz, I. Last and M. Baer, J. Chem. Phys. 106, 7654 (1997).

[34] L. Bañares, F. J. Aoiz, V. J. Herrero, M. J. D'Mello, B. Niederjohann, K. Seekamp-Rahn, E. Wrede and L. Schnieder, J. Chem. Phys. **108**, 6160 (1998).

[35] S. Sukiasyan and H. D. Meyer, J. Chem. Phys. **116**, 10641 (2002).

[36] A. Jäckle and H. D. Meyer, J. Chem. Phys. **109**, 2614 (1998).

[37] B. K. Kendrick, J. Chem. Phys. **114**, 8796 (2001).

[38] B. D. Bean, J. D. Ayers, F. Fernández-Alonso, and R. N. Zare, J. Chem. Phys. **116**, 6634 (2002).

[39] S. C. Althorpe, J. Chem. Phys. **117**, 4623 (2002).

[40] S. C. Althorpe, F. Fernández-Alonso, B. D. Bean, J. D. Ayers, A. E. Pomerantz, R. N. Zare and E. Wrede, Nature (London) **416**, 67 (2002).

[41] S. A. Harich, D. Dai, C. C. Wang, X. Yang, S. D. Chao and R. T. Skodje, Nature (London) **419**, 281 (2002).

[42] S. L. Mielke, K. A. Peterson, D. Q. Schuenke, B. C. Garrett, D. G. Truhlar, J. V. Michael, M. C. Su, and J. W. Sutherland, Phys. Rev. Lett. **91**, 063201 (2003).

[43] T. J. Park and J. C. Light, J. Chem. Phys., **96**, 8853 (1992); *ibid*, **94**, 2946 (1991).

[44] D. X. Dai, C. C. Wang, S. A. Harich, X. Y. Wang, X. M. Yang, S. D. Chao and R. T. Skodje, Science **300**, 1730 (2003).

[45] F. Ausfelder, A. E. Pomerantz, R. N. Zare, S. C. Althorpe, F. J. Aoiz, L. Bañares, and J. F. Castillo, J. Chem. Phys. **120**, 3255 (2004).

[46] K. Koszinowski, N. T. Goldberg, J. Zhang, R. N. Zare, F. Bouakline, and S. C. Althorpe, J. Chem. Phys. (in press).

[47] K. Koszinowski, N. T. Goldberg, A. E. Pomerantz and R. N . Zare, J. Chem. Phys., **123**, 054306-1 (2005); A. E. Pomerantz, F. Ausfelder, R. N . Zare, S. C. Althorpe, F. J. Aoiz, L. Bañares and J. F. Castillo, J. Chem. Phys., **120**,3244 (2004); **120**, 3255 (2004).

[48] C. A. Mead, J. Chem. Phys., **72**, 3839 (1980).

[49] D. G. Truhlar and R. E. Wyatt, Ann. Rev. Phys. Chem. **27**, 1 (1976); G. Herzberg, *ibid.* **38**, 27 (1987); W. H. Miller, *ibid.* **41**, 245 (1990).

[50] I. F. Schneider and A. E. Orel, J. Chem. Phys. **96**, 4283 (1992).

[51] J. L. Krause, K. C. Kulander, J. C. Light and A. E. Orel, J. Chem. Phys. **96**, 4283 (1992); A. E. Orel, I. F. Schneider and A. Suzor-Weiner, Phil. Trans. R. Soc. Lon. **A 358**, 2445 (2000).

[52] B. J. McCall and T. Oka, Science, **287**, 1941, (2000).

[53] V. Kokoouline, Chris H. Greene and B. D. Esry, Nature, **412**, 891 (2001); V. Kokoouline and Chris H. Greene, Faraday Discuss. **127**, 413 (2004); Phy. Rev. Lett. **90**, 133201 (2003).

[54] Dissociative Recombination: theory, experiment and application, IV, Eds. M. Larsson, J. B. A. Mitchell and I. F. Schneider (World Scientific, Singapore, 2000).

[55] M. Larsson, Philos. Trans. R. Soc. London, Ser. A **358**, 2433 (2000); B. J. McCall et al., Nature (London) **422**, 500 (2003); V. Poterya, J. Glosik, R. Plasil, M. Tichy, P. Kudrna, and A. Pysanenko, Phys. Rev. Lett. **88**, 044802 (2002); V. Kokoouline and C. H. Greene, Phys. Rev. A **68**, 012703 (2003).

[56] B. J. McCall, T. R. Geballe, K. H. Hinkle and T. Oka, Science, **279**, 1910 (1998).

[57] D. G. Truhlar and C. J. Horowitz, J. Chem. Phys., **68**, 2466 (1978).

[58] D. G. Truhlar and C. J. Horowitz, J. Chem. Phys, **71**, 1514 (1979).

[59] A. J. C. Varandas, F. B. Brown, C. A. Mead, D. G. Truhlar and N. C. Blais, J. Chem. Phys, **86**, 6258 (1987).

[60] A. L. Boothroyd, W. J. Keogh, P. G. Martin and M. R. Peterson, J. Chem. Phys, **95**, 4343 (1996).

[61] A. L. Boothroyd, W. J. Keogh, P. G. Martin and M. R. Peterson, J. Chem. Phys, **104**, 7139 (1991).

[62] B. Liu, J. Chem. Phys., **58**, 1925 (1973).

[63] P. E. M. Siegbahn and B. Liu, J. Chem. Phys., **68**, 2457 (1978).

[64] M. R. A. Blomberg and B. Liu, J. Chem. Phys., **82**, 1050 (1985).

[65] B. O. Roos, P. R. Taylor and P. E. M. Siegbahn, Chem. Phys., **48**, 157 (1980).

[66] R. N. Porter, R. M. Stevens and M. Karplus, J. Chem. Phys., **49**, 5163 (1968).

[67] T. C. Thompson and C. A. Mead, J. Chem. Phys., **82**, 2408 (1985).

[68] T. C. Thompson, G. Izmirlian Jr., S. J. Lemon, D. G. Truhlar and C. A. Mead, J. Chem. Phys., **82**, 5597 (1985).

[69] K. D. Jordon, Chem. Phys., **9**, 199 (1975).

[70] Y. -S. M. Wu, A. Kuppermann and J. B. Anderson, Phys. Chem. Chem. Phys., **1**, 929 (1999).

[71] S. L. Mielke, B. C. Garrett and K. A. Peterson, J. Chem. Phys., **116**, 4142 (2002).

[72] B. Jayachander Rao, R. Padmanaban and S. Mahapatra, Chem. Phys., **333**, 135 (2007).

[73] S. Ghosal, B. Jayachander Rao and S. Mahapatra, J. Chem. Sci., **119**, 401 (2007).

[74] B. Jayachander Rao and S. Mahapatra, Indian. J. Phys., **81**, 1003 (2007).

[75] J. C. Juanes-Marcos and S. C. Althorpe, Chem. Phys. Lett., **381**, 743 (2003).

[76] J. C. Juanes-Marcos and S. C. Althorpe, J. Chem. Phys., **122**, 204324 (2005).

[77] J. C. Juanes-Marcos, S. C. Althorpe and E. Wrede, Science, **309**, 1227 (2004).

[78] S. C. Althorpe, J. Chem. Phys., **124**, 084105 (2006); ibid, **126**, 044317 (2007).

[79] B. Lepetit, A. Kuppermann, Chem. Phys. Lett., **166**, 581 (1979).

[80] Y. M. Wu, A. Kuppermann and B. Lepetit, Chem. Phys. Lett, 186, 319 (1991).

[81] A. Kuppermann and Y. M. Wu, Chem. Phys. Lett, **205**, 577 (1993).

[82] A. Kuppermann and Y. M. Wu, Chem. Phys. Lett, **241**, 229 (1995).

[83] A. Kuppermann and Y. M. Wu, Chem. Phys. Lett, **349**, 537 (2001).

[84] C. A. Mead and D. G. Truhlar, J. Chem. Phys., **70**, 2284 (1979).

[85] A. J. C. Varandas and H. G. Yu, Faraday Trans. **93** 819 (1997).

[86] C. A. Mead, J. Chem. Phys., **72**, 3839 (1980).

[87] D. A. Kliner, D. E. Adelman and R. N. Zare, J. Chem. Phys., **95**, 1648 (1991).

[88] E. Wrede, L. Schnieder, K. H. Welge, F. J. Aoiz, L. Bañares, V. J. Herrero, B. Martínez-Haya and V. Sáez Rábanos, J. Chem. Phys., **106**, 7862 (1997).

[89] B. K. Kendrick, J. Chem. Phys., **112**, 5679 (2000).

[90] B. K. Kendrick, J. Chem. Phys., **114**, 4335 (2001).

[91] B. K. Kendrick, J. Phys. Chem. A, **107**, 6739 (2003).

[92] B. K. Kendrick, J. Chem. Phys., **118**, 10502 (2003).

[93] B. K. Kendrick, J. Chem. Phys., **114**, 8796 (2001).

[94] R. Bruckmeier, Ch. Wunderlinch, H. Figger, Phys. Rev. Lett., **72**, 2250 (1994).

[95] D. Azinovic, R. Bruckmeier, Ch. Wunderlich, H. Figger, G. Theodorakopoulos and I. D. Petsalakis, Phys. Rev. A., **58**, 1115 (1998).

[96] S. Mahapatra and H. Köppel, Phys. Rev. Lett., **81**, 3116 (1998).

[97] E. J. Rackham, F. Huarte-Larranaga and D. E. Manolopoulos, Chem. Phys. Lett. **343**, 356 (2001).

[98] E. J. Rackham, T. Gonzalez-Lezana and D. E. Manolopoulos, J. Chem. Phys. **119**, 12895 (2003).

[99] D. C. Clary and J. P. Henshaw, Faraday Discuss. Chem. Soc. **84**, 333 (1987).

[100] P. Honvault and J.-M. Launay, J. Chem. Phys. **111**, 6665 (1999).

[101] P. Honvault and J.-M. Launay, J. Chem. Phys. **114**, 1057 (2001).

[102] N. Balucani, L. Cartechini, G. Capozza, E. Segoloni, P. Casavecchia, G. G. Volpi, F. J. Aoiz, L. Bañares, P. Honvault and J.-M. Launay, Phys. Rev. Lett. **89**, 013201 (2002).

[103] A. N. Wright and C. A. Winkler, *Active Nitrogen*; Academic Press: New York, 1968; W. R. Anderson and A. Fontijn, Gas-phase kinetics for propellant combustion modelling: Requirements and experiments, in: R. W. Shaw, T. B. Brill and D. L. Thompson (Eds.), *Overviews of recent research on energetic materials*, World Scientific, Singapore, 2005, p. 192.

[104] T. Suzuki, Y. Shihira, T. Sato and S. Tsunashima, J. Chem. Soc. Faraday Trans., **89**, 995 (1993).

[105] H. Kobayashi, T. Takayanagi, K. Yokoyama, T. Sato and S. Tsunashima, J. Chem. Soc. Faraday Trans., **91**, 3771 (1995).

[106] J. A. Dodd, S. J. Lipson, D. J. Flanagan, W. A. M. Blumberg, J. C. Pearson and B. D. Green, J. Chem. Phys., **94**, 4301 (1991).

[107] H. Umemoto and K. Matsumoto, J. Chem. Phys., **104**, 9640 (1996).

[108] H. Umemoto, T. Asai and Y. Kimura, J. Chem. Phys. **106**, 4985 (1997).

[109] M. Alagia, N. Balucani, L. Cartechini, P. Cachavecchia, G. G. Volpi, L. A. Pederson, G. C. Scatz, G. Lendavy, L. B. Harding, T. Hollenbeek, T. -S. Ho and H. Rabitz, J. Chem. Phys. **119**, 3063 (2003).

[110] T. -S. Ho, H. Rabitz, F. J. Aoiz, L. Bañares, S. A. Vázquez and L. B. Harding, J. Chem. Phys., **119**, 3063 (2003).

[111] S. Y. Lin and H. Guo, J. Chem. Phys., **124**, 031101 (2006).

[112] S. Y. Lin and H. Guo, Phys. Rev. A **74**, 022703 (2006).

[113] S. Y. Lin, L. Bañares and H. Guo, J. Phys. Chem. A, (2007), 10.1021/jp0682715.

[114] A. J. C. Varandas and L. A. Poveda, Theor. Chem. Acc., **116**, 404 (2006).

[115] T. S. Chu, K. L. Han and A. J. C. Varandas, J. Phys. Chem. A., **110**, 1666 (2006).

[116] J. F. Castillo, N. Bulut, L. Bañares and F. Gogtas, Chem. Phys., **332**, 119 (2007).

[117] S. K. Gray, G. G. Balint-Kurti, J. Chem. Phys. **108**, 950 (1998).

[118] J. M. Bowman, J. Phys. Chem. **95**, 4960 (1991).

[119] (a)S. L. Mielke, G. C. Lynch and D. G. Truhlar, J. Phys. Chem., **98**, 8000 (1994); (b)D. H. Zhang, J. Z. H. Zhang, J. Chem. Phys. **110**, 7622 (1999).

[120] L. A. Pederson, G. C. Schatz, T. Ho, T. Hollenbeek, H. Rabitz and L. B. Harding, J. Chem. Phys., **110**, 9091 (1999).

[121] N. Aronszajn, Trans. Am. Math. Soc., **68**, 337 (1950).

[122] C. de Boor and R. Lynch, J. Math. Mech., **15**, 953 (1966).

[123] P. J. Davis, *Interpolation and approximation*, Dover, New York (1975).

[124] S. Zhou, D. Xie, S. Y. Lin and H. Guo, J. Chem. Phys., **128**, 224316 (2008).

[125] K. Dressler and D. A. Ramsay, Philos. Trans. R. Soc. London, Ser. A **51**, 553 (1959).

[126] F. Santoro, C. Petrongolo and G. C. Schatz, J. Phys. Chem., A **106**, 8276 (2002).

[127] P. Defazio and C. Petrongolo, J. Chem. Phys., **125**, 064308 (2006).

[128] L. Adam, W. Hack, G. C. MacBane, H. Zhu, Z.-W. Qu and R. Schinke, J. Chem. Phys. **126**, 034304 (2007).

[129] R. F. Lu, T. S. Chu, Y. Zhang, K. L. Han, A. J. C. Varandas and J. Z. H. Zhang, J. Chem. Phys., **125**, 133108 (2006).

[130] F. Bouakline, S. C. Althorpe and D. P. Ruiz, J. Chem. Phys., **128**, 124322 (2008).

[131] T. S. Chu, K. L. Han, M. Hankel and G. G. Balint-Kurti, J. Chem. Phys., **126**, 214303 (2007).

[132] M. Hankel, S. C. Smith, R. J. Allan, S. K. Gray and G. G. Balint-Kurti, J. Chem. Phys., **125**, 164303 (2006).

[133] P. Defazio and C. Petrongolo, J. Chem. Phys., **127**, 204311-1 (2007).

[134] R. Kosloff, J. Phys. Chem., **92**, 2087 (1988); Ann. Rev. Phys. Chem., **45**, 145 (1994), and references therein.

[135] R. T. Pack, J. Chem. Phys., **60**, 633 (1974).

[136] P. McGuire and D. J. Kouri, J. Chem. Phys., **60**, 2488 (1974).

[137] D. T. Colbert and W. H. Miller, J. Chem. Phys. **96**, 1982 (1992).

[138] A. Askar and A. S. Cakmak, J. Chem. Phys. **68**, 2794 (1978); D. Kosloff and R. Kosloff, Comput. Phys. Commun. **30**, 333 (1983); J. Chem. Phys. **52**, 35 (1983).

[139] M. D. Feit, J. A. Fleck Jr. and A. Steiger, J. Comput. Phys. 47, 412 (1982).

[140] H. Tal-Ezer and R. Kosloff, J. Chem. Phys., **81**, 3967 (1984).

[141] T. J. Park and J. C. Light, J. Chem. Phys. **85**, 5870 (1986).

[142] G. Arfken, *Mathematical Methods for Physicists*, Academic Press Inc., Prism Books Pvt. Ltd., Bangalore, (1994).

[143] R. Kosloff, J. Phys. Chem., **92**, 2087 (1988).

[144] V. Mohan and N. Sathyamurthy, Comput. Phys. Rep., **7**, 213 (1988).

[145] R. Kosloff, Ann. Rev. Phys. Chem., **45**, 145 (1994).

[146] D. Kosloff and R. Kosloff, J. Comput. Phys., **52**, 35 (1983).

[147] J. C. Light, I. P. Hamilton, J. V. Lill, J. Chem. Phys. **82**,1400 (1985). Z. Bačić, J. C. Light, Ann. Rev. Phys. Chem. **40**, 469 (1989).

[148] D. Neuhauser and M. Baer, J. Phys. Chem. **93**, 2872 (1989); J. Chem. Phys. **91**, 4651 (1989); D. Neuhauser, M. Baer, R. S. Judson and D. J. Kouri, Comput. Phys. Commun. **63**, 460 (1991).

[149] S. Mahapatra and N. Sathyamurthy, J. Chem. Soc., Faraday Trans. **93**, 773 (1997).

[150] J. Z. H. Zhang, Theory and Application of Quantum Molecular Dynamics; World Scientifc, Singapore, 1999.

[151] F. J. Aoiz, L. Bañares, and J. F. Castillo, J. Chem. Phys. **111**, 4013 (1999).

[152] B. Jayachander Rao, T. Rajagopal Rao and S. Mahapatra, [Manuscript under preparation].

[153] W. H. Press, B. P. Flannery,S. A. Teukolsky, W. T. Vetterling, Numerical Recipes in Fortran: The Art of Scientifc Computing, 2nd ed.; Cambridge University Press: New York.

[154] Y. Zheng, J. Chem. Phys., **122**, 094316 (2005).

[155] T. J. Park and J. C. Light, J. Chem. Phys. **91**, 974 (1992).

[156] D. K. Bondi, D. C. Clary, J. N. L. Conner, B. G. Garrett and D. G. Rtuhlar, J. Chem. Phys., **76**, 4986 (1982).

[157] T. J. Park and J. C. Light, J. Chem. Phys., **96**, 8853 (1992).

[158] T. J. Park and J. C. Light, J. Chem. Phys., **94**, 2946 (1991).

[159] F. J. Aoiz, M. Brouard, C. J. Eyles, J. F. Castillo and V. S. Rãbanos, J. Chem. Phys. **125**, 144105 (2006).

[160] F. Göğtas, G. G. Balint-Kurti and A. R. Offer, J. Chem. Phys., **104**, 7927 (1996).

[161] S. Sukiasyan and H. -D. Meyer, J. Chem. Phys., **116**, 10641 (2002).

[162] *Dynamics of Molecules and Chemical Reactions*, edited by R. E. Wyatt and J. Z. H. Zhang (Marcel Dekker, New York, 1996).

[163] (a) N. Balakrishnan, C. Kalyanaraman, N. Sathyamurthy, Phys. Rep. **280**, 79, (1997); (b) M. Beck, A. Jäckle, G. A. Worth, and H. -D. Mayer, Phys. Rep. **324**, 1, (2000); (c) G. Nyman and H. -G. Yu, Rep. Prog. Phys. **63**, 1001 (2000).

[164] R. Skodje, R. Sadeghi, H. Kppel and J. Krause, J. Chem. Phys., **101**, 1725 (1994).

[165] S. K. Gray, E. M. Goldfield, G. C. Schatz and G. G. Balint-Kurti, Phys. Chem. Chem. Phys., **1**, 1141 (1999).

[166] F. Fernández-Alonso and R. N. Zare, Annu. Rev. Phys. Chem., **53**, 67 (2002).

[167] U. Manthe, H.-D. Mayer, and L. S. Cederbaum, J. Chem. Phys. **97**, 9062 (1992); V. Engel, Chem. Phys. Lett. **189**, 76 (1992).

[168] R. Sadeghi and R. T. Skodje, J. Chem. Phys. **102**, 193 (1995).

[169] S. Mahapatra and N. Sathyamurthy, J. Chem. Phys. **105**, 10934 (1996).

[170] M. L. Mehta, *Random Matrices*, 2^{nd} ed. (Academic. New York).

[171] M. V. Berry and M. Tabor, Proc. R. Soc. London, Ser. **A 356**, 375 (1977).

[172] T. A. Brody, J. Flores, J. B. French, P. A. Mello, A. Pandey, and S. S. M.Wong, Rev. Mod. Phys. **53**, 385 (1981).

[173] M. V. Berry and M. Robnik, J. Phys. **A 17**, 2413 (1984).

[174] S. Mahapatra and H. Köppel, J. Chem. Phys. **109**, 1721 (1998).

[175] M. Jungen, M. Lehner and R. Guérout, Khimicheskaya Fizika **23(2)**, 71 (2004);(an electronic copy of the same can be obtained from the author on request).

[176] S. Mahapatra and H. Köppel, Chem. Phys. Lett. **306**, 387 (1999).

[177] G. Herzberg, J. T. Hougen and J. K. G. Watson, Can. J. Phys. **60**, 1261 (1982).

[178] U. Müller and P. C. Cosby, J. Chem. Phys. **105**, 3531 (1996).

[179] W. Ketterle, H. P. Messmer and H. Walther, Europhys. Lett. **8**, 333 (1989).

[180] U. Manthe and H. Köppel, J. Chem. Phys., **93**, 345, 1685 (1990).

[181] M. Jungen, (Unpublished results).

[182] B. Lepetit, Z. Peng and A. Kuppermann, Chem. Phys. Lett. **166**, 572 (1990)

[183] G. Herzberg, J. T. Hougen and J. K. G. Watson, Can. J. Phys. **60**, 1261 (1982).

[184] U. Müller and P. C. Cosby, J. Chem. Phys. **105**, 3531 (1996).

[185] W. Ketterle, H. P. Messmer and H. Walther, Europhys. Lett. **8**, 333 (1989).

[186] U. Galster, Private communication.

[187] I. Mistrik, R. Reichle, U. Müller, H. Helm, M. Jungen and J.A. Stephens, Phy. Rev. A **61**, 033410 (1999).

List of Publications:

1. **B. Jayachander Rao**, S. Mahapatra, H. Köppel and M. Jungen, *J. Chem. Phys*, **123**, 134325 (2005); "On the ($E \otimes e$)-Jahn-Teller conical intersections in the 3p (E') and 3d (E'') Rydberg electronic states of triatomic hydrogen"
2. **B. Jayachander Rao**, R. Padmanaban and S. Mahapatra, *Chem. Phys.* **333**, 135 (2007); "Nonadiabatic quantum wave packet dynamics of H + H_2 (HD) reactions".
3. R. Padmanaban, S. Ghosal, **B. Jayachander Rao** and S. Mahapatra, "Time-dependent quantum wave packet dynamics of atom-diatom reactive scattering", in: Proceedings of 2nd international conference on current developments in Atomic molecular and chemical physics with applications, Ed. Man Mohan, Narosa Publications, New Delhi.
4. **B. Jayachander Rao** and S. Mahapatra, *J. Chem. Phys.* **127**, 244307 (2007); "Quantum wave packet dynamics of the N(^2D) + H_2 reaction".
5. **B. Jayachander Rao** and S. Mahapatra, *Ind. J. Phys.* **81**, 1 (2007); "On the electronic nonadiabatic effects in the H + H_2 reaction dynamics".
6. S. Ghosal, **B. Jayachander Rao** and S. Mahapatra, *J. Chem. Sci.* **119**, 401 (2007); "Reactive chemical dynamics through conical intersections".
7. **B. Jayachander Rao**, R. Padmanaban and S. Mahapatra, [manuscript under preparation]; "Coriolis coupled nonadiabatic quantum wave packet dynamics of the H + H_2 exchange reaction".
8. **B. Jayachander Rao**, T. Rajagopal Rao and S. Mahapatra, [manuscript under preparation]; "Nonadiabatic quantum wave packet dynamics of the D + H_2, D + HD and H + D_2 exchange reactions".

Presentations in Conferences:

1. Poster presented in "Symposium in Theoretical Chemistry (TCS - 2004)", BARC, Mumbai, December 9 - 12, 2004.
2. Poster presented in "Chemfest 2005" in School of Chemistry, University of Hyderabad, February 19, 2005.
3. Poster presented in "Current Developments in Atomic, Molecular and Optical Physics with Applications (CDAMOP 2006)", Delhi University, New Delhi, March 21-23, 2006.
4. Poster presented in "Theoretical Chemistry Symposium (TCS - 2006)", Bharathidasan University, Thiruchirappalli, December 11-13, 2006.
5. Poster presented in "Asian Spectroscopy Conference (ASC 2007)", Indian Institute of Science, Bangalore, January 29-02 February, 2007.
6. Poster presented in "Chemfest 2006, 2007, 2008", School of Chemistry, University of Hyderabad.
7. Oral presentation in "Chemsfest 2008", School of Chemistry, University of Hyderabad.